A Numerical Study of Midlatitude Squall Lines with the Canadian Regional Finite-Element Model

Stéphane Bélair

Department of Atmospheric and Oceanic Sciences

McGill University, Montreal

A Thesis submitted to the Faculty of Graduate Studies and Research in partial fulfillment of the requirements for the degree of Doctor of Philosophy

 January 1995

National Library of Canada

Bibliothèque nationale du Canada

Acquisitions and Bibliographic Services Branch

Direction des acquisitions et des services bibliographiques

395 Wellington Street
Ottawa, Ontario
K1A 0N4

395, rue Wellington
Ottawa (Ontario)
K1A 0N4

Your file Votre référence

Our file Notre référence

ISBN 0-612-05670-8

Canada

ABSTRACT

A research version of the Canadian regional finite-element (RFE) model is used to evaluate the capability of the operational model in reproducing the meso-β-scale structure and evolution of three different types of midlatitude squall-line systems, and to advance our understanding on the development of these features.

In this thesis, we use the well-documented 10-11 June 1985 squall line as a test bed to examine the appropriate incorporation of various physical representations and their coupling with RFE's model components. It is demonstrated through a series of sensitivity studies that the operational prediction of squall lines can be improved if more realistic model physics, reasonable initial conditions, and high resolution are used. It is shown that subgrid-scale moist convection and grid-scale moist physics must be adequately treated in order to reproduce the internal structures of the squall line.

Then, the improved version of the RFE model is used to study the role of gravity waves in the development of a prefrontal squall line associated with the 14 July 1987 Montreal flood. It is found that the gravity waves and convection propagate in a "phase-locked" manner and that the wave-CISK mechanism accounts for the maintenance and intensification of the system. It is also found that frontogenetical processes and release of conditional symmetric instability are responsible for the development of a trailing stratiform rainband associated with the July 1987 Montreal flood. Numerous sensitivity experiments are conducted, and they show that the meso-β-scale structures and the wave-convection system are very sensitive to the interaction of the parameterized convection with grid-scale physical processes.

In the last part of the thesis, the along-line variability of the 26-27 June 1985 squall line during PRE-STORM is examined. It is found that the three-dimensional structures of the squall's circulations are determined by both a large-scale trough and convectively generated disturbances. In particular, it is shown that rear inflows in the stratiform region tend to be more intense to the south of the mesolow and near the base of the large-scale trough.

RESUME

Une version de recherche du modèle canadien régional aux éléments finis (EFR) est utilisée pour évaluer la capacité du modèle opérationnel de reproduire les structures méso-β-échelles et l'évolution de trois lignes de grain aux latitudes moyennes, et pour approfondir la compréhension du développement de ces systèmes.

Nous utilisons le cas bien documenté de la ligne de grain du 10-11 juin 1985 pour vérifier si l'incorporation de diverses représentations physiques et leur couplage avec les composantes du modèle EFR sont convenables. Il est démontré par des études de sensibilité que la prédiction opérationnelle de lignes de grain peut être améliorée si une physique de modèle plus réaliste, des conditions initiales raisonnables, et une haute résolution sont utilisés. Il est montré que la convection sous-échelle et les processus humides à l'échelle du modèle doivent être traités adéquatement pour reproduire les structures internes de la ligne de grain.

Ensuite, la version améliorée du modèle EFR est utilisée pour étudier le rôle des ondes de gravité dans le développement d'une ligne de grain pré-frontale associée à l'inondation du 14 juillet 1987 à Montréal. Il est montré que les ondes de gravité et la convection se propagent en phase et que le mécanisme ondes-CISK est responsable pour le support et l'intensification du système. Il est aussi montré que des processus frontogénétiques et le relâchement d'instabilité symétrique conditionnelle sont responsables du développement d'une bande de précipitation stratiforme à l'arrière de la ligne de grain. Des études de sensibilité ont été conduites, et montrent que les structures méso-β-échelle et le système onde-convection sont très sensibles à l'interaction entre la convection paramétrisée et les processus à l'échelle du modèle.

Finalement, la variabilité le long de la ligne de grain du 26-27 juin 1985 est examinée. On trouve que les circulations tridimensionnelles de la ligne de grain sont déterminées par un creux à grande échelle et des perturbations générées par la convection. En particulier, il est montré que des courants entrant à l'arrière de la région stratiforme ont tendance à être plus intenses au sud du mésocreux et près de la base du creux à grande échelle.

ACKNOWLEDGMENTS

I wish to thank Prof. Da-Lin Zhang, my thesis supervisor, and Dr. Jocelyn Mailhot of RPN, for their considerable support and assistance during the course of the thesis research. I also wish to thank Prof. Jacques Derome, Drs. Michel Béland and Andrew Staniforth for making this research possible. I acknowledge the technical assistance provided by the supporting staff at RPN, and especially Mr. Bernard Bilodeau, to deal with the complicated RFE modeling system. Thanks also go to Mr. Ning Bao, who provided the necessary initial conditions from the PSU/NCAR modeling system. The research staff at RPN and faculty at the Department of Atmospheric and Oceanic Sciences of McGill University have helped improve the content of this thesis, through their comments and recommendations.

I am also grateful to the American Meteorological Society for permitting the reproduction of article 1 as part of the thesis.

Finally, I must thank my mother, sister, and Pierre Loiselle who supported me throughout the course of this project and who never had any doubts about my capacities. Most importantly, I am indebted to my wife for letting me spend so much time on this project.

TABLE OF CONTENTS

List of Figures

Figure		Page

Figure		Page

Figure		Page

Figure Page

Figure		Page

Figure Page

List of Tables

STATEMENT OF ORIGINALITY

The original aspects of the thesis are described as follows:

1) It is demonstrated that the operational prediction of the meso-β-scale structures of midlatitude squall lines, such as mesolows, mesohighs, cold outflows, mesovortices, rear inflows, gravity waves and quantitative aspects of precipitation, can be obtained if realistic convective parameterization and explicit moist physics, reasonable initial conditions, and high resolution are included.

2) It is found that the two-dimensional structures of some midlatitude squall lines may depart substantially from the classical squall-line models depending upon the interaction of the convective systems with their large-scale environment. These structures include the rapid propagation and separation of a leading convective line from a trailing rainband, the development of a surface-based instead of an elevated rear-to-front descending flow, the generation of low-to-mid-level stratiform clouds, and the development of an intense anticyclonic vorticity band in the stratiform region.

3) The internal circulations of squall lines are found to depend on the location of the convective system with respect to large-scale and convectively generated mesoscale circulations. These processes determine the along-line variability of the internal flow of squall lines, as well as the weather conditions at different segments of the convective systems.

4) It is found that rear inflows are more intense to the south of convectively-induced mesolows and near the base of large-scale troughs. This region also favors the development of trailing stratiform precipitation.

MANUSCRIPTS AND AUTHORSHIP

Candidates have the option, **subject to the approval of their Department**, of including, as part of their thesis, copies of the text of a paper(s) submitted for publication, or the clearly-duplicated text of a published paper(s), provided that these copies are bound as an integral part of the thesis.

If this option is chosen, **connecting texts, providing logical bridges between the different papers, are mandatory.**

The thesis must still conform to all other requirements of the "Guidelines Concerning Thesis Preparation" and should be in a literary form that is more than a mere collection of manuscripts published or to be published. **The thesis must include, as separate chapters or sections:** (1) a Table of Contents, (2) a general abstract in English and French, (3) an introduction which clearly states the rationale and objectives of the study, (4) a comprehensive general review of the background literature to the subject of the thesis, when this review is appropriate, and (5) a final overall conclusion and/or summary.

Additional material (procedural and design data, as well as descriptions of equipment used) must be provided where appropriate and in sufficient detail (e.g., in appendices) to allow a clear and precise judgement to be made of the importance and originality of the research reported in the thesis.

In the case of manuscripts co-authored by the candidate and others, **the candidate is required to make an explicit statement in the thesis of who contributed to such work and to what extent**; supervisors must attest to the accuracy of such claims at the Ph.D. Oral Defense. Since the task of the Examiners is made more difficult in these cases, it is in the candidate's interest to make perfectly clear the responsibilities of the different authors of co-authored papers.

The complete text of the above must be cited in full in the introductory sections of any theses to which it applies.

CO-AUTHORED MANUSCRIPTS

Chapters 3 to 6 of this thesis are in the form of articles published or submitted for publication in scientific journals. The results and analyses presented in these manuscripts originate from the research work I performed within the context of the Ph.D. project. The co-authors of the manuscripts, namely, Prof. D.-L. Zhang and Dr. J. Mailhot, provided normal supervision of the project. They also helped arrange and edit the text.

Chapter 1

Introduction

1.1 Mesoscale convective systems

It has been recently realized that mesoscale processes often generate precipitation systems that differ considerably from what would be expected from the synoptic conditions (e.g., Charba and Klein 1980; Ramage 1982; Gyakum 1986). Accurate prediction of these mesoscale convective systems (MCSs) has been a serious challenge to atmospheric scientists for many years, partly because of the lack of understanding on how these MCSs develop, and partly because of the fact that MCSs often occur on a scale too small to be resolved by the standard rawinsonde network or handled by operational numerical weather prediction (NWP) models. Thus, data from high-resolution networks, such as the Oklahoma-Kansas Preliminary Regional Experiment for STORM central (PRE-STORM) field program in the United States (Cunning 1986), together with radar and satellite imagery, are useful to study the internal structure and evolution of these weather systems.

MCSs are deep convective systems which are considerably larger than individual thunderstorms and sometimes characterized by an extensive region of stratiform clouds to the rear (see Cotton and Anthes 1989). The convective region of the cloud systems has typical lifetimes of 6 to 12 h, whereas the stratiform region may last for as long as several days. The MCSs are responsible for a large percentage of the summertime precipitation in some regions (see Fritsch et al. 1986; Fritsch and Heideman 1989) and may produce violent weather events such as flash flood, gust winds, hail and tornadoes. They are categorized in two types of systems, namely squall lines and mesoscale convective complexes (MCCs), which are discriminated according to their shapes in satellite images. MCCs show circular shapes (e.g., Maddox 1980a; McAnelly and Cotton 1986, 1989;

Leary and Rappaport 1987; Augustine and Howard 1991) whereas squall lines display linear and smaller-scale structures (e.g., Bluestein and Jain 1985; Smull and Houze 1985; Johnson and Hamilton 1988). Furthermore, MCCs are driven by the diurnal cycle and are typically nocturnal events, in contrast with squall lines which are more driven by strong dynamics than thermodynamics. Squall lines are also modulated by the diurnal cycle but they can occur at any time of the day. However, a firm categorization of MCSs is not possible, since recent studies have shown that lines of deep convection could occur within large mesoscale systems exhibiting a circular cloud shield at upper levels (e.g., Stumpf et al. 1991; Stensrud and Fritsch 1993; Trier and Parsons 1993; Nachamkin et al. 1994). Thus, the set of MCSs rather constitutes a continuous spectrum of events in which prefrontal squall lines are at one extreme of the spectrum, and the MCCs are at the other end.

a. Mesoscale convective complexes

MCCs were first defined from satellite imagery by Maddox (1980a), based on the areal extent, eccentricity and duration of the generated upper-level cloud shields. He noted that MCCs are particularly well organized midlatitude convective systems that are often responsible for heavy nocturnal rainfalls during the growing season (see also McAnelly and Cotton 1989; Augustine and Howard 1991). Maddox (1983) conducted a composite study of 10 MCCs and showed that they are convective systems with a warm core for most of the troposphere (Menard and Fritsch 1989) and a cold core near the tropopause. The warm core structure tends to force a strong mass and moisture convergence in the low to midlevels and strong outflow near the tropopause. The MCCs typically develop in the afternoon in the region of a weak surface front coupled with a low-level southerly jet of moist warm air. The primary forcing is associated with low-level warm advection and weak midlevel propagating short wave. While some portion of the warm advection is associated with travelling waves, some of it seems to be the result of diurnally modulated, terrain related boundary-layer processes. Cotton et al. (1989) performed a composite study similar to Maddox (1983) but with a sampling of 134 cases and better temporal resolution. They divided the lifecycle of MCCs into seven periods and found that the upper-tropospheric divergence and vorticity in MCCs are maximized at the mature stage and maintain nearly as constants until their dissipation stage. This is quite different from what happens for tropical clusters in which the maximum values are reached at maturity but rapidly decrease shortly after. This difference comes from the fact that MCCs are inertially stable, i.e., their horizontal scale is greater than the Rossby radius.

b. Squall lines

In this thesis, we focus on the second type of MCSs, i.e., squall lines, which are easily recognizable from radar and satellite images, due to their linear nature. Squall lines form in a conditionally unstable atmosphere characterized by strong low-level vertical wind shear. They have been categorized in four different types of development (i.e., broken line, back building, broken areal, and embedded areal), depending on the relative magnitudes of vertical wind shear, convective available potential energy (CAPE), Richardson number, and large-scale forcing (e.g., frontal zones, dry lines, orography) (see Bluestein and Jain 1985). Weisman and Klemp (1982) further showed that the amount of CAPE and wind shear determine the severity and duration of squall lines, which are constituted by long-lived rotating supercell storms with a low Richardson number or by multicellular type thunderstorms with a high Richardson number.

Thorpe et al. (1982) argued that the propagation of squall lines is related to the convectively-induced cold pool, which act as an obstacle to the flow, by producing convergence at the interface between the cold pool and the storm relative inflow. They proposed that the long life of the strictly two-dimensional solution is a consequence of low-level shear in the ambient wind profile. Rotunno et al. (1988) added to this argument by viewing the non-supercellular squall as a line of short-lived ordinary convective cells and recognizing the primary importance of the low-level wind shear in the regeneration of the cells by balancing the cold pool outflow. Squall line propagation has also been associated with gravity waves, which can initiate convective activity when moving in an environment having low convective inhibition and positive CAPE (see Uccellini 1975). A number of studies have reported that convection and gravity waves could move together in a "phase-locked" manner (e.g., Miller and Sanders 1980; Stobie et al. 1983; Einaudi et al. 1987; Zhang and Fritsch 1988a; Ramamurthy et al. 1993), suggesting that the wave-CISK mechanism, by which gravity waves provide the necessary low-level convergence to initiate new convection and latent heating/cooling amplifies the waves, could be responsible for the propagation and intensification of squall lines (see Cram et al. 1992a; Tremblay 1994).

There are many studies on the internal structures of squall lines in midlatitudes. The associated precipitation is typically characterized by a leading line of intense and deep convection, followed by an extensive area of lighter stratiform precipitation (see Fig. 1.1) (e.g., Smull and Houze 1985; Johnson and Hamilton 1988; Houze et al. 1989; Zhang et al. 1989; Biggerstaff and Houze 1991a). Intense surface pressure perturbations are often produced within these systems (see Fig. 1.1), such as a pre-squall mesolow caused by the adiabatic warming due to the compensating subsidence (see Hoxit et al. 1976), a mesohigh below the convective line, which is induced by strong evaporational cooling (see Fujita 1959), and a wake low at the rear of the stratiform region (Johnson and Hamilton 1988). A surface gust front also can be generated, which tends to enhance the low-level convergence ahead of the convective line, thus assisting the initiation of new convective cells.

According to the conceptual model of squall lines developed by Houze et al. (1989), the convectively generated anvil clouds could extend rearward a few hundreds of kilometers behind the leading line (Fig. 1.2). The relative across-line flow exhibits an overturning updraft, a front-to-rear (FTR) ascending current that transports high

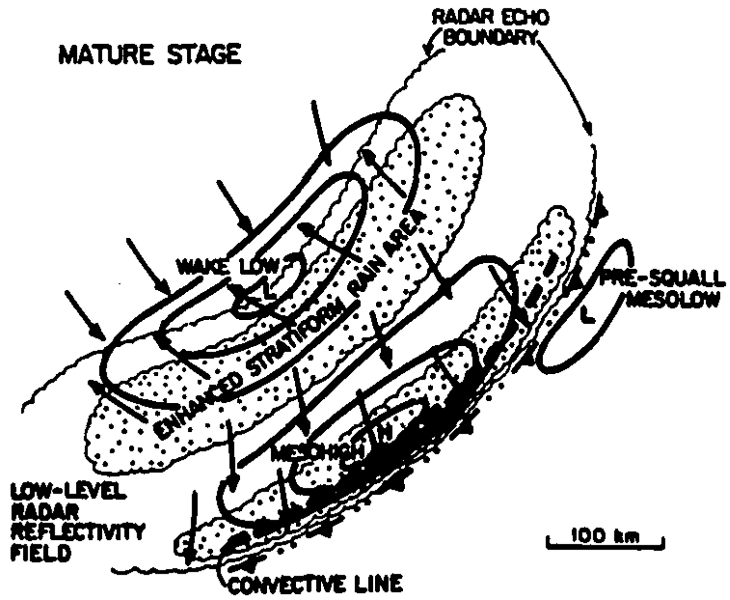

Fig. 1.1 Conceptual model of a squall line with a trailing stratiform region viewed in a horizontal cross section (from Johnson and Hamilton 1988).

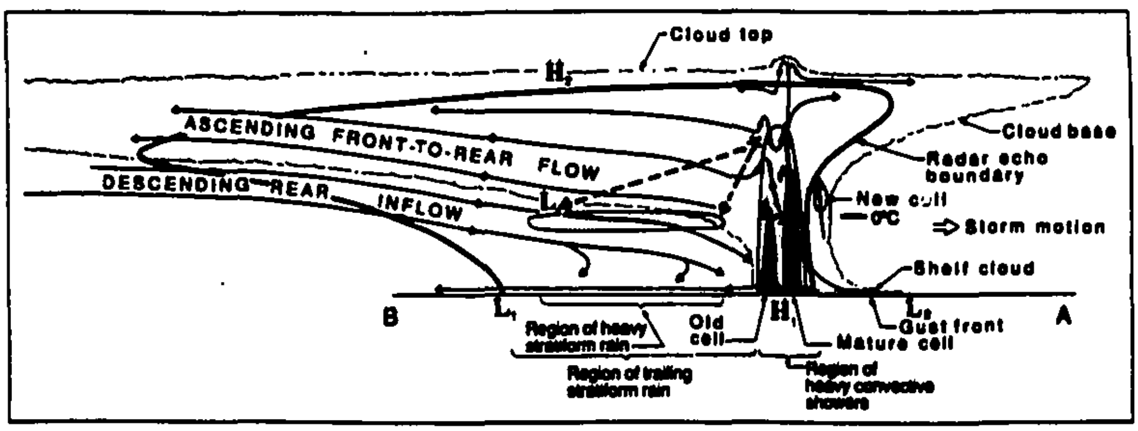

Fig. 1.2 Conceptual model of a squall line with a trailing stratiform area viewed in a vertical cross section perpendicular to the convective line (from Houze et al. 1989).

equivalent potential temperature (θ_e) air into the trailing stratiform region from the boundary-layer ahead, and a rear-to-front (RTF) midlevel current (or rear inflow jet) that advects low-θ_e air into the cloudy region, leading to sublimation/evaporation such that the flow is forced to descend (see Smull and Houze 1985, 1987; Zhang and Gao 1989; Stensrud et al. 1991). As the adiabatic warming through the descending motion exceeds the diabatic cooling, a surface wake low can be found at the back edge of the stratiform region (Johnson and Hamilton 1988; Zhang and Gao 1989).

The previous studies have shown that the trailing stratiform precipitation can contribute to as much as 40 % of the total precipitation of a squall system (see Houze 1977; Churchill and Houze 1984; Johnson and Hamilton 1988). In earlier studies, it is hypothesized that the trailing stratiform precipitation is produced as a result of a slower propagation of the convective cells with respect to the gust front, leaving a series of "old towers" in various stages of decay behind the leading convective line (Newton 1950; Zipser 1969, 1977; Houze 1977; Zipser et al. 1982). More recently, Smull and Houze (1985) found, from examination of water budgets, that the fallout of the rearwardly advected ice particles from the leading convective line was responsible for most of the trailing stratiform precipitation. These results are consistent with those of Biggerstaff and Houze (1991a), who showed that the strongest stratiform precipitation tends to be located immediately behind the most intense portions of the convective line, and that the width of the stratiform region depends on both the FTR wind velocity and microphysical fallout scales. Zhang and Cho (1992) proposed that the mid to upper levels of the FTR ascending flow could be unstable slantwisely after conditional instability is relieved along the leading line.

Stratiform regions are often correlated to the development of some important mesoscale features, such as midlevel mesolows (see Smull and Houze 1987; Houze et al. 1989; Zhang and Gao 1989), mesovortices (see Leary and Rappaport 1987; Zhang and Fritsch 1987, 1988b; Brandes 1990; Biggerstaff and Houze 1991b; Zhang 1992), rear inflow jets (see Smull and Houze 1985, 1987; Rutledge et al. 1988; Zhang and Gao 1989; Schmidt and Cotton 1990; Weisman 1992), and upper-level mesohighs (see Fritsch and Maddox 1981a,b; Zhang and Gao 1989; Gallus and Johnson 1992; Lin and Johnson 1994). The midlevel mesolow results from diabatic heating within the stratiform region (see Smull and Houze 1987; Zhang and Gao 1989), whereas the upper-level mesohigh is due to the cooling associated with adiabatic expansion at the top of intense updrafts (see Fritsch and Brown 1982). Midlevel mesovortices can be initiated by tilting of horizontal vorticity due to the downward motion at the rear of stratiform regions (see Biggerstaff and Houze 1991b; Zhang 1992). Zhang (1992) showed that such mesovortices could move forward faster than the squall system and, in the dissipating stages, reach the convergence zone between the FTR and RTF circulations, where they intensify due to stretching of existing vorticity (see also Brandes 1990; Johnson and Bartels 1992). Smull and Houze (1987) hypothesized that rear inflow jets could result from a convectively-induced midlevel mesolow within the stratiform region. Schmidt and Cotton (1990) argued that the downward deflection and channeling of ambient RTF flow by upper-level divergent outflow related to the convectively-induced mesohigh could also lead to the formation of rear inflow jets (see Nachamkin et al. 1994). Other mechanisms were also proposed by Lafore and Moncrieff (1989), Zhang and Gao (1989), and Weisman (1992). However, the along-line variability of these internal structures has received little attention. In the case of long squall lines, there are considerable variabilities even in the large-scale flow. Convectively generated mesovortices also contribute to the development of three-dimensional structures of squall lines.

1.2 Numerical prediction of MCSs

Due to the lack of appropriate initial conditions and the complexity of the physical processes involved in the development of MCSs, only a few successful real-data simulations of MCSs have been presented in the literature. Using the Penn State

University / National Center for Atmospheric Research (PSU/NCAR) model, Zhang and Fritsch (1986, 1988b) and Zhang et al. (1989) performed simulations of three well-documented midlatitude MCSs that compared very well against observations. The mesoscale structures of the squall line that occurred on 10-11 June 1985, such as the leading convective line, trailing stratiform region, surface pressure perturbations, rear inflow jet, and midlevel mesovortices, were particularly well simulated (see Zhang and Gao 1989; Zhang 1992). Other mesoscale models that have been used to obtain reasonable simulations of squall lines include the Colorado State University / Regional Atmospheric Modeling System (CSU/RAMS) (Cram et al. 1992b) and the Mesoscale Compressible Community (MC2) model (Tremblay 1994).

It should be mentioned that these previous numerical studies were only limited to a research mode, because the lateral boundary conditions used in these models were specified by observations. Operational prediction of these internal structures of MCSs has not been possible due to the use of coarse grid resolution and poor physical representations. Because of the rapid increases in computing power in recent years, operational models will be soon able to resolve MCSs. Thus, in order to improve mesoscale weather forecasts, considerable work is currently done in operational centres such as those in Canada, the United States, and Europe, to decrease the horizontal grid length for future versions of the operational models. Although it is easy to understand the relationship between grid resolution and mesoscale structures, it is unclear how this improvement could occur. Previous studies with the United States operational model show that even if the large-scale circulation and pressure patterns are well predicted, mesoscale processes generate embedded weather features that are considerably far from what would be expected from the large-scale conditions (see Sanders 1979; Charba and Klein 1980; Gyakum 1986). Moreover, because precipitation is mostly organized on the mesoscale (see Heideman and Fritsch 1988), progress for the quantitative precipitation forecasts (QPFs) and severe weather warnings has been slow, compared to that for the large-scale forecasts.

Anthes et al. (1989) demonstrated with the PSU/NCAR model that the latent heating due to condensation/evaporation and surface fluxes can have a significant impact on the model's performance. They showed that although simple physical parameterization schemes are enough for usual weather systems, more sophisticated physics packages are needed for more complicated extreme cases such as MCSs and explosive cyclones. Thus, the improvement of the horizontal resolution in NWP models is not enough to refine the prediction of mesoscale features, and better treatments of physical processes, such as planetary boundary layer (PBL), condensation/evaporation and radiation, must be incorporated into those models.

In particular, the treatment of heating, moistening and precipitation due to condensation/evaporation is of primary importance for a realistic prediction of MCSs (Zhang et al. 1988, 1994; Zhang 1989; Molinari and Dudek 1992). These cloud processes can be represented in numerical models in an implicit or explicit manner. The explicit representation, in which the clouds are resolved on the grid scale, uses cloud water (ice), and rainwater (snow) as prognostic variables. Most of the explicit schemes are based on the bulk method introduced by Kessler (1969) and described as the "direct method" (e.g., Sundqvist et al. 1989; Zhang 1989). In models with grid lengths small enough to resolve individual convective elements (i.e., $\Delta x < 5$ km), the explicit approach could represent reasonably cloud processes. However, as the horizontal resolution decreases, the use of a convective parameterization (or implicit scheme) is necessary to account for the subgrid-scale transport. The implicit treatment of clouds requires the evaluation of heating, moistening and precipitation due to these subgrid-scale effects in terms of resolvable-scale variables. The widely used convective parameterization schemes include the Manabe et al. (1965) moist adjustment, the Kuo (1965, 1974) moisture convergence, the Arakawa and Schubert (1974) quasi-equilibrium, the Kreitzberg and

Perkey (1976) and the Fritsch and Chappell (1980) schemes. Due to the complexity in the convective parameterization, different hypotheses and closure assumptions may not be suitable for all scales. In other words, convective parameterization schemes designed for larger-scale models (e.g., the Kuo or Manabe schemes) may prove inadequate for fine-mesh models, and vice-versa (see Frank 1983). In addition, at the scale of 10~40 km, it is important that the implicit and explicit schemes be coupled in order to allow a broader scale interaction between the deep convection and its large-scale environment (see Zhang et al. 1988; Zhang and Fritsch 1988c).

1.3 General objectives and thesis outline

The purpose of this thesis is to demonstrate that the internal structures and evolution of midlatitude squall lines as well as their quantitative aspects of precipitation could be predicted using an improved version of the Canadian operational model, namely, the regional finite-element (RFE) model. Specific objectives focusing on numerical predictions of squall lines are to

• determine the sensitivity of numerical predictions of squall lines to different implicit and explicit condensation schemes and different initial conditions;

• examine the role of gravity waves in the development of a squall line and the sensitivity of the convection-gravity waves structure to different convective parameterizations;

• investigate the dynamical and physical processes responsible for the development of trailing stratiform precipitation;

• discuss the effects of the large-scale environment and convectively-induced midlevel mesolows in producing along-line variabilities in a squall line;

• clarify the dynamic processes involved in the development of a rear inflow jet.

Based on the previous studies, it is important to have more realistic physical representation in the RFE model in order to achieve the above-mentioned objectives.

Thus, as part of the project, we incorporate the improved version of the Fritsch and Chappell (1980) convective parameterization (see Zhang and Fritsch 1986) and the explicit moisture scheme (see Zhang 1989) containing cloud water (ice) and rainwater (snow) as prognostic variables. Furthermore, we need to make sure that these schemes could interact properly and are coupled with other dynamic as well as physical processes in the RFE model. Thus, a well-documented squall line case, i.e., that occurred during 10-11 June 1985, will be used to test the capability of the RFE model in reproducing the basic internal structures of the system as verified against high-resolution network data. Then, the model will serve as a numerical tool to investigate the interesting features of other midlatitude squall lines, namely the 14 July 1987 squall system near Montreal and the 26-27 June 1985 PRE-STORM squall line.

In the next chapter, the important dynamical and physical aspects of the RFE model are described. In chapter 3, we test the capability of the RFE model in reproducing the precipitation and mesoscale structures of the 10-11 June 1985 squall line (e.g., Johnson and Hamilton 1988; Rutledge et al. 1988; Zhang et al. 1989; Zhang and Gao 1989; Biggerstaff and Houze 1991a,b). Chapter 4 shows the importance of gravity waves in the development of the squall system associated with the 14 July 1987 Montreal flood. The dynamical and physical processes leading to the development of a stratiform rainband behind the squall line are investigated in chapter 5. In chapter 6, we use the numerical prediction of the 26-27 June 1985 PRE-STORM squall line to examine the along-line variability of the internal flow structures. Presentations given in chapters 3-6 represent materials, each as an article, submitted for publication in the journals of *Wea. and Forecasting*, *Atmos.-Ocean*, and *Mon. Wea. Rev.* A summary and future work are described in chapter 7.

Chapter 2

The regional finite-element model

The RFE model, which is now used operationally for forecasts up to 48 h at the Canadian Atmospheric Environment Service (AES), is an ensemble of subroutines treating an extensive range of atmospheric processes with state-of-the-art techniques. The model is divided into two parts to handle the dynamical and physical aspects separately. Figure 2.1 shows graphically the main philosophy and structure of the RFE model. A brief description of the important aspects of the model is given as follows.

2.1 The dynamics

The dynamical and numerical aspects of this model were first introduced by Staniforth and Daley (1979), and recently described by Tanguay et al. (1989). The governing equations of the model are the hydrostatic primitive equations on a polar-stereographic projection using the σ (normalized pressure) vertical coordinate. The horizontal momentum, thermodynamic, continuity, moisture and hydrostatic equations are:

$$\frac{dU}{dt} + \frac{\partial \phi}{\partial X} + RT\frac{\partial \ln p_s}{\partial X} = fV - \left(\frac{U^2 + V^2}{2}\right)\frac{\partial S}{\partial X} + F^u \tag{2.1}$$

$$\frac{dV}{dt} + \frac{\partial \phi}{\partial Y} + RT\frac{\partial \ln p_s}{\partial Y} = -fU - \left(\frac{U^2 + V^2}{2}\right)\frac{\partial S}{\partial Y} + F^v \tag{2.2}$$

$$\frac{dT}{dt} - \frac{RT}{c_p}\left(\frac{d\ln p_s}{dt} + \frac{\dot{\sigma}}{\sigma}\right) = F^T \tag{2.3}$$

$$\frac{d\ln p_s}{dt} + D + \frac{\partial \dot{\sigma}}{\partial \sigma} = 0 \tag{2.4}$$

$$\frac{dq_v}{dt} = F^{q_v} \tag{2.5}$$

DYNAMICS-ADIABATIC

Solve the primitive equations with no physical forcing.

$(u,v,T,q_v,q_c,q_r)^F = 0$

Solve a Helmoltz equation for W and recover all the other variables. Finite-elements, semi-implicit time discretization and semi-Lagrangian 3D advection

$$\frac{G^{(1)}-G^{(n-1)}}{2\Delta t} + NG = 0$$

with

$$G = (Q, D, T, Ln\, p_s, q_v, q_c, q_r)$$

HORIZONTAL DIFFUSION

$$\frac{G^{(2)}-G^{(1)}}{2\Delta t} = F_1 G^{(1)}$$

where

$$F_1 = \gamma\nabla^2$$

RADIATION PACKAGE

Calculate the influence of solar radiation on the ground properties (considering clouds) and also the infrared cooling-warming at each level

PBL PACKAGE

Calculate vertical diffusion coefficient as well as surface and deep soil variables

IMPLICIT VERTICAL DIFFUSION (PBL and radiation)

$$\frac{G^{(3)}-G^{(2)}}{2\Delta t} = F_2 G^{(2)}$$

where

$$F_2^{u,v} = \frac{\partial}{\partial\sigma}\left(A^2 K_m \frac{\partial(u,v)}{\partial\sigma}\right);$$

$$F_2^T = \frac{\partial}{\partial\sigma}\left[A^2 K_T \sigma^K\left(\frac{\partial T}{\partial\sigma} - \frac{KT}{\sigma} - \gamma_{CG}^T\right)\right]$$

$$F_2^{q_v} = \frac{\partial}{\partial\sigma}\left(A^2 K_T \frac{\partial q_v}{\partial\sigma}\right)$$

CONDENSATION SCHEME

Implicit and explicit condensation

$$\frac{G^{(n+1)} - G^{(3)}}{2\Delta t} = F_3 G^{(3)}$$

for the temperature, specific humidity, cloud water/ice and rainwater/snow

ROBERT TIME FILTER

The historical variables of the model are filtered according to:

$$F_n(t) = F(t) + \frac{v}{2}\left[F(t+\Delta t) - 2F(t) + F(t+\Delta t)\right]$$

Fig. 2.1 Main flow chart of the RFE model.

$$\frac{\partial \phi}{\partial \sigma} = -\frac{RT}{\sigma} \tag{2.6}$$

Here, p is the pressure, p_s is the surface pressure, $\dot{\sigma} = d\sigma/dt$, ϕ is the geopotential height, T is the virtual temperature, q_v is the specific humidity, $S = m^2$, m is the map-scale factor, $(U,V) = (u/m, v/m)$ are the wind images, (u,v) are the wind component along the (X,Y) axes of the polar stereographic domain, $D = S(U_X + V_Y)$ is the horizontal divergence, f is the Coriolis parameter, R is the gas constant, c_p is the specific heat of air, and F represents the parameterized forcing terms. The vorticity equation is obtained by taking the curl of the momentum equations:

$$\frac{dQ}{dt} = S\left[-\frac{\partial}{\partial X}\left(RT\frac{\partial \ln p_s}{\partial Y}\right) + \frac{\partial}{\partial Y}\left(RT\frac{\partial \ln p_s}{\partial X}\right)\right] - QD$$
$$+ S\left(\frac{\partial U}{\partial \sigma}\frac{\partial \dot{\sigma}}{\partial Y} - \frac{\partial V}{\partial \sigma}\frac{\partial \dot{\sigma}}{\partial X}\right) + S\left(\frac{\partial F^v}{\partial X} - \frac{\partial F^u}{\partial Y}\right) \tag{2.7}$$

where $Q = S(V_X - U_Y) + f$ is the vertical component of absolute vorticity.

The model boundary conditions are chosen such that the mass is self contained. In other words, there is no flow across the top, bottom or lateral boundaries, i.e., $\dot{\sigma} = 0$ for the top and bottom boundaries, and $\vec{V} \cdot \vec{n} = 0$ for the lateral boundaries, where $\vec{V} = (u,v)$ is the horizontal wind vector and $\vec{n}$ is the normal vector.

The model integrates the governing equations using a semi-implicit method (see Robert et al. 1972), in which the fast-evolving linear terms are treated implicitly while the slow-evolving non-linear terms are treated explicitly. This method permits the use of rather long time steps, as compared to those in models with the leapfrog scheme (Staniforth and Côté 1991). A semi-Lagrangian technique is adopted in the RFE model to calculate the advection terms, thus allowing a further increase in time step, with no loss of accuracy (Staniforth and Temperton 1986; Staniforth and Côté 1991).

The time-discretized equations are reduced to a single equation (Helmoltz problem) for a new variable, *W*, which is related to the divergence as

$$D = -\frac{\partial W}{\partial \sigma} \tag{2.8}$$

The Helmoltz equation is discretized spatially according to the finite-element technique (Strang and Fix 1973) that consists in expanding the dependent variables into piecewise functions for all three directions (x,y,σ). In the formulation adopted in the RFE model, the basis functions are triple product of the unidimensional Chapeau functions $e^i(w)$ (see Fig. 2.2):

$$e^i(\omega) = \frac{\omega_{i+1}-\omega}{\omega_{i+1}-\omega_i}\,;\ \omega_i \langle \omega \langle \omega_{i+1} \tag{2.9}$$

$$e^i(\omega) = \frac{\omega-\omega_{i-1}}{\omega_i-\omega_{i-1}}\,;\ \omega_{i-1} \langle \omega \langle \omega_i \tag{2.10}$$

$$e^i(\omega) = 0\ ;\ \text{elsewhere} \tag{2.11}$$

where ω is one of the three directions x, y or σ and i=1, 2, 3,..., N represents the nodes on each directional axis. The dependent variables are expanded as:

$$F(x,y,\sigma) = \sum_{i,j,k=1}^{N_i,N_j,N_k} F_{ijk}\theta^{ijk}(x,y,\sigma) \tag{2.12}$$

$$\theta^{ijk}(x,y,\sigma) = e^i(x)\, e^j(y)\, e^k(\sigma) \tag{2.13}$$

where $F_{ijk} = F(x_i,y_j,\sigma_k)$. Since the basis functions are almost orthogonal to each other, they only interact locally. Therefore, mathematical operations on functions expanded with this method give rise to simple matrices, which can be manipulated efficiently at low computational cost. The Helmoltz equation for *W* is solved using the Galerkin method (Strang and Fix 1973), according to which the error caused by the use of these piecewise

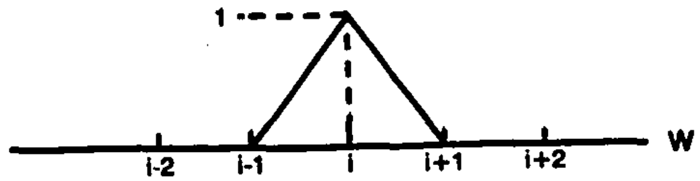

Fig. 2.2 Form of the Chapeau functions $e^i(w)$ used as a basis for the finite-element spatial discretization.

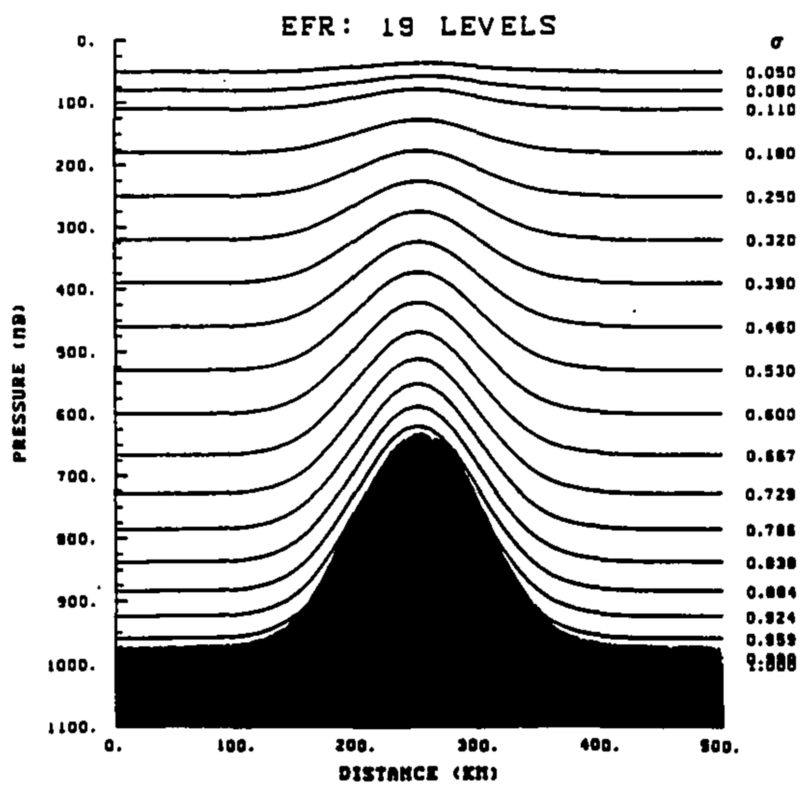

Fig. 2.3 Example of the vertical distribution of the σ levels in the RFE model.

polynomials is orthogonalized to the basis functions (see details in Staniforth 1987). Then, all the historical model variables are calculated back from W.

One major advantage of the finite-elements technique over other methods is that it allows the use of a variable-resolution grid in all three directions. For example, the vertical levels are unequally spaced with an aggregate of levels in the lowest atmosphere (see Fig. 2.3). Of more originality is the use of a variable-horizontal resolution grid that was introduced by Staniforth and Mitchell (1978) (see Fig. 2.4). In this grid configuration, the central domain has a uniform resolution and is surrounded by a variable-resolution mesh with grid-length increasing by a constant factor (generally kept smaller than 1.15) until it reaches the equator. This variable resolution self-nesting strategy is an original way to have a model that is regional as well as hemispheric, thereby simplifying the specification of the lateral boundary conditions.

2.2 The physics

The physical processes in the RFE model, including both subgrid and grid-scale diabatic processes, appear in the form of parameterized forcing terms given in Eqs. (2.1)-(2.6). Table 2.1 lists the basic physical schemes that are available in the RFE model and provides the associated references. In the next, we only describe the PBL, the implicit and explicit condensation schemes, and the treatment of radiation.

a. Boundary layer parameterization

The surface temperature (T_s) is predicted for every land and ice dominated grid points using the force-restore method, as described in Deardorff (1979). This surface temperature is influenced by solar and infrared radiation, eddy exchanges of heat and vapor with the air, precipitation mass flux and heat and water diffusion into the soil. Its time variation is computed from

$$\frac{\partial T_s}{\partial t} = \frac{-2\sqrt{\pi}}{C_s d_T}\left[H_s + L_v E_s + \varepsilon_s\left(\sigma_{SB} T_s^4 - F_{I_s}\right) - (1-\alpha) F_{S_s}\right] - \frac{2\pi}{\tau}\left(T_s - T_p\right) \qquad (2.14)$$

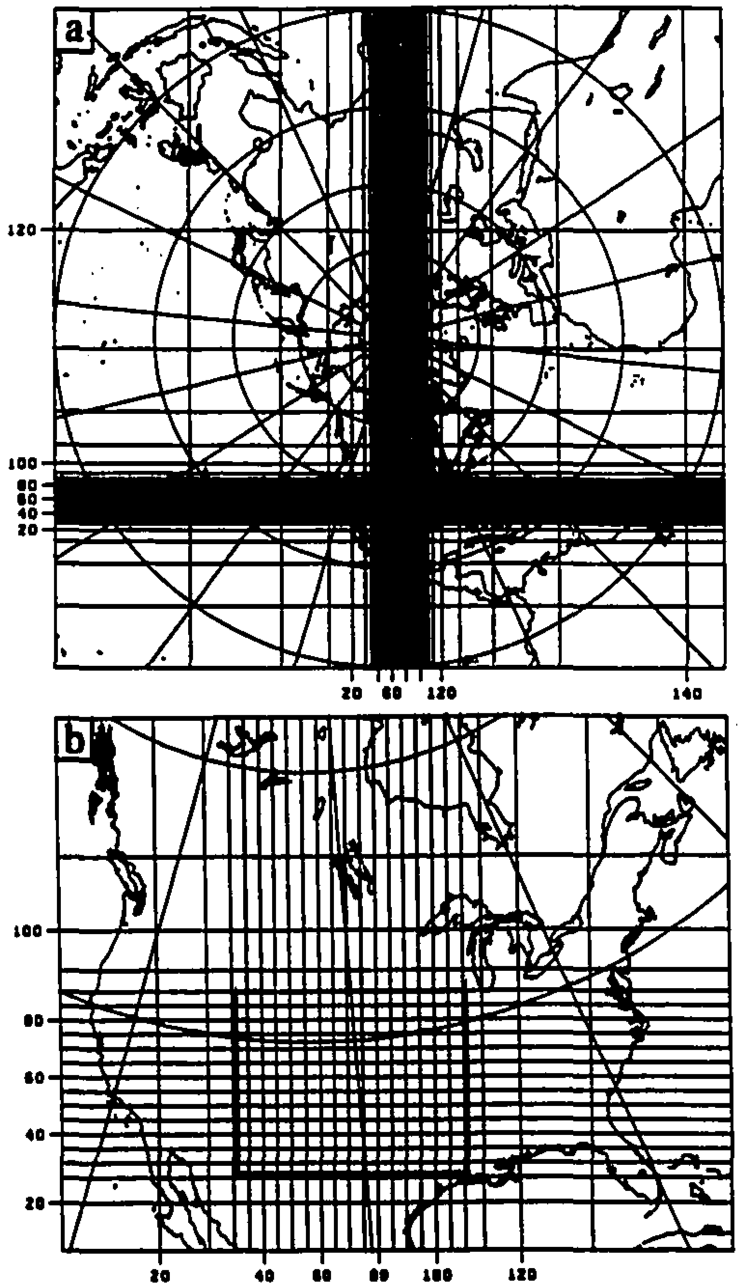

Fig. 2.4 Example of the hemispheric variable grid mesh projected on a polar stereographic plane. The heavy rectangle indicates uniform high resolution of 25 km with the grid size increasing by the constant factors 1.134 northward, 1.142 eastward, 1.140 southward and 1.145 westward. Lines are drawn every 5 points. a) represents the complete 141 x 125 grid while b) is only a portion of it.

TABLE 2.1: Physical schemes of the RFE model

Surface energy budget	Force-restore method	Benoit et al. (1989) Deardorff (1979)
Planetary boundary layer	Turbulent kinetic energy	Mailhot and Benoit (1982) Benoit et al. (1989)
Convective parameterization	Fritsch-Chappell scheme	Fritsch and Chappell (1980) Zhang and Fritsch (1986)
	Kuo scheme	Mailhot et al. (1989)
	Manabe convective adjustment scheme	Daley et al. (1976)
Grid-scale condensation	Explicit moisture scheme	Zhang (1989) Hsie et al. (1980)
	Sundqvist scheme	Pudykiewicz et al. (1992)
	Supersaturation removal scheme	Mailhot et al. (1989)
Infrared radiation	Sasamori scheme	Sasamori (1972)
	Garand scheme	Garand (1983)
Solar radiation	Simple scheme	Delage (1979)
	Fouquart-Bonnel scheme	Fouquart and Bonnel (1980)
Horizontal diffusion	∇^2 on σ surfaces	Benoit et al. (1989)

where ε_S and C_S are the soil emissitivity and capacity, respectively; α is the albedo; τ is the Earth rotation period; d_T is the depth of soil diffusion diurnal wave; L_V is the latent heat of vaporisation; F^{-}_{IS}, F^{-}_{SS} are the incoming infrared and solar radiation at surface, respectively; H_S and E_S are the turbulent fluxes of sensible heat and vapor; and σ_{SB} is the Stefan-Boltzmann constant.

In the surface layer, which is the first turbulent layer above the roughness length (Z_0), the vertical fluxes of momentum, heat, and moisture, are determined by

$$\left|\overline{w'V'}\right|_s = (C_M |V_a|)^2 \tag{2.15}$$

$$\left(\overline{w'\theta'}\right)_s = C_M\, C_T |V_a| (\theta_s - \theta_a) \tag{2.16}$$

$$\left(\overline{w'q_v'}\right)_s = C_M\, C_T |V_a| (q_{vs} - q_{va}) \tag{2.17}$$

Here, C_M and C_T are functions of Z_a / Z_0 and the bulk Richardson number

$$R_{iB} = \frac{g}{\theta_{vs}} \frac{\theta_{va} - \theta_{vs}}{V_a^2 + w_*^2} Z_a \tag{2.18}$$

The subscripts *s* and *a* refer to the surface and anemometer levels, $w_*^3 = g\left(\overline{w'\theta_v'}\right)_s h/\theta_{vs}$ is the convective velocity scale, and *h* is the PBL height. Using this formulation, the vertical fluxes are large when the surface layer becomes unstable (i.e., when $R_{iB} < 0$) (see Benoit et al. 1989; Mailhot 1994).

Above the surface layer, the parameterized forcing terms are computed following

$$[\, V, \theta, q_v \,]_t^F = -\frac{1}{\rho} \frac{\partial}{\partial Z} \rho\, \overline{w' [\, V', \theta', q_v' \,]} \tag{2.19}$$

where

$$\overline{w'V'} = -K_M \frac{\partial V}{\partial Z} \tag{2.20}$$

$$\overline{w'q_v'} = -K_T \frac{\partial q_v}{\partial Z} \tag{2.21}$$

$$\overline{w'\theta'} = -K_T\left(\frac{\partial\theta}{\partial Z} - \gamma_\theta H(k,k_+)\right) \tag{2.22}$$

and $[\ ]_t = d/dt$, K_M and K_T are the vertical diffusion coefficients for momentum and temperature. Note that the counter-gradient term γ_θ is used here to allow the presence of upward fluxes in an inversion layer above the well-mixed boundary layer. This term is weighted by a step function H that varies with height. The vertical diffusion coefficients K_M and K_T are evaluated using the turbulent kinetic energy ($TKE = E$):

$$2E = \overline{u'u'} + \overline{v'v'} + \overline{w'w'} \tag{2.23}$$

and the relations for K_M and K_T are:

$$K_M = a\sqrt{E}\lambda\ ;\ \ K_T = \frac{K_M}{P_r} \tag{2.24}$$

where λ is a mixing length, a is a non-dimensional universal constant and P_r is the Prandtl number which is the ratio of the momentum and heat turbulent diffusivities. The TKE is predicted every time step using

$$\frac{dE}{dt} = BE^{1/2} - CE^{3/2} + \frac{\partial}{\partial Z}\left(K_M\frac{\partial E}{\partial Z}\right) \tag{2.25}$$

where $BE^{1/2}$ is a source term, $CE^{3/2}$ represents viscous dissipation and the last term on the rhs represents the vertical redistribution of TKE. For a more complete discussion of the PBL parameterization, the reader is referred to Benoit et al. (1989).

b. Condensation physics

The treatment of clouds in numerical models has been known for a long time to have a significant impact on numerical prediction of severe summertime weather systems (see Frank 1983; Zhang and Fritsch 1988c; Molinari and Dudek 1992). In this section, we describe two schemes that are newly incorporated into the RFE model as part of the present thesis work.

The convective (implicit) scheme used for this thesis is the Fritsch and Chappell (1980; hereafter FC) scheme, also described in Zhang and Fritsch (1986). The FC scheme assumes that 90% to 100% of the CAPE must be removed during a convective time scale τ_C, which is specified to be between 30 and 60 min. For a parcel lifted vertically along a moist adiabat, the CAPE is defined as:

$$\mathrm{CAPE} = \int_{\mathrm{LFC}}^{\mathrm{ETL}} g\left(\frac{T_u(z) - T(z)}{T(z)}\right)dz \qquad (2.26)$$

where *LFC* is the level of free convection, *ETL* is the level of equilibrium temperature at which the temperature of the upward lifted parcel, T_u, is the same as that of the environment, T. In the FC convective scheme, the feedback to the grid-scale temperature and humidity tendencies is proportional to the CAPE in one atmospheric column. The model convection is triggered when the following two conditions are met: first, the column is convectively unstable for a deep enough layer and second, the low-level vertical velocity is strong enough to lift the parcel to its lifting condensation level (LCL). The cloud top is calculated as the level where the negative area equals the positive area in skew T / lop p diagrams.

Once convection is initiated, the grid area is divided at every level in three parts: (i) a convective updraft area (A_u), (ii) a convective downdraft area (A_d), and (iii) an environmental subsidence area (A_e). As the air in the updraft area is lifted, condensate is produced and then falls to the ground as convective precipitation or evaporates in the anvil and in the convective downdrafts. Driven by mechanisms similar to that of the updrafts, moist downdrafts have their origin at the level of free sink (LFS), which is the analog of the LFC for the updrafts and is often located at the level of minimum θ_e. The downdraft parcels descend until they become buoyant. Otherwise, they reach the ground, filling up the lowest layers. The moist downdraft effect has been considered to be of primary importance in the parameterization of convection (Zhang and Fritsch 1988c; Molinari and

Dudek 1992). The tendencies for specific humidity and temperature are then calculated from:

$$\left(\frac{\partial T}{\partial t}\right)_{FCP} = \frac{\widehat{T} - T_0}{\tau_c} \tag{2.27}$$

$$\left(\frac{\partial q_v}{\partial t}\right)_{FCP} = \frac{\widehat{q_v} - q_{v0}}{\tau_c} \tag{2.28}$$

where

$$\widehat{T}(z) = \frac{T_u(z)A_u(z) + T_d(z)A_d(z) + T_e(z)A_e(z)}{A_u(z) + A_d(z) + A_e(z)} \tag{2.29}$$

$$\widehat{q_v}(z) = \frac{q_{vu}(z)A_u(z) + q_{vd}(z)A_d(z) + q_{ve}(z)A_e(z)}{A_u(z) + A_d(z) + A_e(z)} \tag{2.30}$$

and T_O, q_{VO} are the grid-scale vertical profiles of temperature and specific humidity. First guess of convective downdraft and updraft areas are used to calculate the CAPE of the convectively-adjusted environment after the stabilization. The grid areas $A_u(z)$, $A_d(z)$, and $A_e(z)$ are then adjusted in such a way to allow the scheme to remove the right amount of buoyant instability (i.e., between 90% and 100%).

To complete the treatment of clouds in the RFE model, an explicit moisture scheme, based on Zhang (1989), Hsie et al. (1984) and Dudhia (1989), is coupled with the FC scheme. This explicit scheme requires the incorporation of two additional prognostic variables: cloud water/ice content q_c, and rainwater/snow content q_r. For efficiency and economy reasons, a simple strategy is adopted in which the liquid phase is allowed to exist only beneath the 0°C isotherm, and the solid phase above. The dynamical equations are given as:

$$\left(\frac{\partial q_v}{\partial t}\right)_{ex} = P_{CED} + P_{RED} - P_{GCI} \tag{2.31}$$

$$\left(\frac{\partial q_c}{\partial t}\right)_{ex} = P_{GCI} - P_{CED} - P_{AUT} - P_{ACR} + F_{HD}(q_c) + F_{VD}(q_c) \tag{2.32}$$

$$\left(\frac{\partial q_r}{\partial t}\right)_{ex} = P_{AUT} + P_{ACR} - P_{RED} - \frac{g}{p_s}\frac{\partial(\rho q_r v_t)}{\partial\sigma} + F_{HD}(q_r) \tag{2.33}$$

$$\left(\frac{\partial T}{\partial t}\right)_{ex} = \frac{L}{C_{pm}}(P_{GCI} - P_{CED} - P_{RED}) - \frac{\delta L_f}{C_{pm}}\left(\frac{\dot{\sigma}(q_c+q_r) + \rho g v_t q_r}{\Delta\sigma}\right) \tag{2.34}$$

where the subscript "ex" denotes tendencies due to the explicit scheme, P_{GCI} is the generation rate of cloud water/ice from supersaturation; P_{AUT} represents the autoconversion rate of cloud water/ice to rainwater/snow; P_{ACR} is the accretion rate of cloud water/ice by rainwater/snow; P_{CED} is the evaporation/sublimation rate of cloud water/ice or deposition growth of cloud ice; P_{RED} represents the evaporation/sublimation rate of rainwater/snow or deposition growth of snow; F_{HD}, F_{VD} are respectively the horizontal and vertical diffusion terms; and v_t is the terminal velocity of the rainwater (snow). The fourth term on the rhs of (2.33) represents the fallout of the rainwater (snow), and the last term on the rhs of (2.34) is for the melting/freezing at the 0°C isotherm. The other symbols assume their standard meteorological meaning.

An important consequence of the incorporation of these two prognostic variables is that the water loading effect due to the liquid and solid phases can now be represented in the model. This is done by modifying the hydrostatic relation (see Zhang et al. 1988):

$$\frac{\partial\varphi}{\partial\sigma} = -\frac{RT_w}{\sigma} \tag{2.35}$$

where the new "wet" temperature T_w is:

$$T_w = T_v\left[1 + \frac{q_c+q_r}{1+q_v}\right]^{-1} \tag{2.36}$$

where T_v is the virtual temperature. As expressed in (2.36), the presence of the liquid and solid phases has the same effect as cooling, and thus it either slows down upward motion or accelerates downward motion. Thus, the explicit moisture scheme contains the effects of virtual temperature, hydrostatic water loading, condensation/evaporation, deposition/sublimation, freezing/melting, and the fallout of rainwater/snow.

c. Radiation

The radiation scheme used for the numerical simulations presented in this thesis is simple (see Benoit et al. 1989). Its main purpose is to represent the effect of solar and infrared radiation in the lower atmosphere. The incoming solar flux at the surface is given by:

$$F^{-}_{Ss} = S_0 \, \tau_d \, \tau_c \, \mathrm{MAX}(\, 0 \, , \cos \mathrm{ZEN} \,) \tag{2.37}$$

where S_o is the solar constant (1370 W m^{-2}), τ_d is the assumed clear air transmission factor, τ_c is a reduction factor associated with the amount of cloudiness and *ZEN* is the solar zenith angle.

The infrared (or long-wave) radiation includes the absorption by water vapor and carbon dioxide at each level according to the scheme developed by Sasamori (1972). No water or cloud masking is considered in the infrared cooling/warming of the surface. The incoming infrared radiation at the surface is given by:

$$F^{-}_{Is} = 0.67 \left[\frac{p_s \, q_{va}}{0.622}\right]^{0.08} B(Z_a) + \Delta F^{-}_{Is} \tag{2.38}$$

where ΔF^{-}_{Is} is an enhancement of infrared radiation at the surface in the presence of clouds, $B = \sigma_{SB} T^4$, and q_{va} is the specific humidity at the anemometer level. For more details on the treatment of radiation in the RFE model, see Mailhot (1994).

Chapter 3

Numerical prediction of the 10-11 June 1985 squall line

3.1 Presentation of article 1

Before using the improved mesoscale version of the RFE model to investigate the dynamical and physical processes leading to the generation of particular mesoscale structures within midlatitude squall lines, it is important to verify first that this model is indeed capable of realistically predicting the initiation, evolution and internal structures of such MCSs. Thus, we validate the model using the prediction of the squall line that occurred during 10-11 June 1985 PRE-STORM. This case study was logically chosen because this MCS has been well documented by Johnson and Hamilton (1988), Rutledge et al. (1988), Biggerstaff and Houze (1991a,b), and Gallus and Johnson (1992); and well simulated by research models (Zhang et al. 1989; Zhang and Gao 1989; Zhang and Cho 1992; Grell 1993). Thus, strict and careful comparisons between the predictions, the observations, and previous simulations are possible. This would greatly facilitate understanding of the problems related to severe weather warnings and quantitative forecasts of precipitation, as well as confirming the validity of subsequent squall line studies using the model. Moreover, comparisons with the predictions using the current version of the operational model with different physical parameterizations would provide information on the importance of various physics treatments in the future improvement of the operational model.

3.2 Article 1

Numerical prediction of the 10-11 June 1985 squall line with the Canadian regional finite-element model. By Stéphane Bélair, Da-Lin Zhang, and Jocelyn Mailhot

Wea. Forecasting, **9**, 157-172.

Reprinted from WEATHER AND FORECASTING, Vol. 9, No. 2, June 1994
American Meteorological Society

Numerical Prediction of the 10–11 June 1985 Squall Line with the Canadian Regional Finite-Element Model

STÉPHANE BÉLAIR AND DA-LIN ZHANG

Department of Atmospheric and Oceanic Sciences, McGill University, Montreal, Quebec, Canada

JOCELYN MAILHOT

Recherche en Prévision Numérique, Atmospheric Environment Service, Dorval, Quebec, Canada

(Manuscript received 11 June 1993, in final form 8 November 1993)

ABSTRACT

In an effort to improve operational forecasts of mesoscale convective systems (MCSs), a mesoscale version of the operational Canadian Regional Finite-Element (RFE) Model with a grid size of 25 km is used to predict an intense MCS that occurred during 10–11 June 1985. The mesoscale version of the RFE model contains the Fritsch–Chappell scheme for the treatment of subgrid-scale convective processes and an explicit scheme for the treatment of grid-scale cloud water (ice) and rainwater (snow).

With higher resolution and improved condensation physics, the RFE model reproduces many detailed structures of the MCS, as compared with all available observations. In particular, the model predicts well the timing and location of the leading convective line followed by stratiform precipitation; the distribution of surface temperature and pressure perturbations (e.g., cold outflow boundaries, mesolows, mesohighs, and wake lows); and the circulation of front-to-rear flows at both upper and lower levels separated by a rear-to-front flow at midlevels.

Several sensitivity experiments are performed to examine the effects of varying initial conditions and model physics on the prediction of the squall system. It is found that both the moist convective adjustment and the Kuo schemes can reproduce the line structure of convective precipitation. However, these two schemes are unable to reproduce the internal flow structure of the squall system and the pertinent surface pressure and thermal perturbations. It is emphasized that as the grid resolution increases, reasonable treatments of both parameterized and grid-scale condensation processes are essential in obtaining realistic predictions of MCSs and associated quantitative precipitation.

1. Introduction

Due to rapid increases in computer power in recent years, operational numerical models have improved markedly by refining their numerical and physical schemes, and by increasing their grid resolution, which very soon will be high enough to resolve mesoscale convective systems (MCSs). As a consequence, growing attention is now being paid to improve mesoscale weather forecasts at numerous operational meteorological centers. These improvements have led to remarkable progress in operational prediction of large-scale pressure systems (e.g., extratropical cyclones). However, the progress in quantitative precipitation forecasts (QPFs) and severe weather warnings has lagged substantially behind the large-scale forecasts (e.g., Charba and Klein 1980; Sanders 1979). This is particularly true during the warm season when a large portion of annual precipitation is produced by MCSs (e.g., Fritsch et al. 1981; Heideman and Fritsch 1988), which are generally too small to be resolved by the conventional data network and handled by current operational models. Therefore, the improvement of the average skill in QPFs for the warm season has occurred much slower than that for the cold season (Ramage 1982). Similarly, the average skill in QPFs for precipitation systems forced by mesoscale mechanisms has been much lower than those forced by large-scale processes (Fawcett 1977; Heideman and Fritsch 1988; Fritsch and Heideman 1989). Thus, it appears that significant improvements in QPFs and severe weather warnings are possible when mesoscale weather systems can be better predicted by operational models.

Although the relationship between the grid resolution and the mesoscale structure is easy to understand, it is not clear how an increase in horizontal resolution will improve numerical prediction of mesoscale quantitative precipitation and severe weather events. First, since numerical weather prediction is an initial-value problem, the details contained in the initial conditions are of primary importance. Numerous studies have shown that numerical simulations of MCSs are very

Corresponding author address: Stéphane Bélair, Department of Atmospheric and Oceanographic Sciences, McGill University, 845 Sherbrooke Street West, Montreal, Quebec H3A 2T5, Canada.

sensitive to changes in the initial humidity, temperature, and horizontal winds (Kelly et al. 1978; Zhang and Fritsch 1986a; Chang et al. 1986). Clearly, this imposes a severe limit on the quality of mesoscale weather forecast, particularly considering that the initial conditions in an operational setting are far from adequate in providing mesoscale details. Second, as the grid resolution increases, solutions corresponding to more energetic and transient circulations may become important. Their interactions with diabatic heating/cooling and boundary-layer processes may produce significant undesirable small-scale perturbations. Thus, certain physical parameterization schemes designed for coarse-mesh models may prove inadequate for fine-mesh models. This is especially true for the treatment of moist convection that could change drastically as the horizontal grid size decreases from hundreds of kilometers to tens of kilometers (Frank 1983). For instance, the large-scale models need to parameterize both deep convection *and* mesoscale circulations, whereas mesoscale models need *only* to parameterize deep convection, since the mesoscale circulation can be explicitly resolved. As the grid size is further reduced (e.g., <5 km), all convective elements can be explicitly resolved, and convective parameterization can be bypassed. But even for a grid mesh of 10 km, some type of parameterization is still needed in order to remove rapidly conditional instability in a vertical column and help activate grid-box saturation at the right time and location (Zhang et al. 1988). Therefore, for models with intermediate grid size (i.e., 20–30 km), it is essential that a realistic convective parameterization be coupled with an explicit scheme treating solid, liquid, and vapor phases (Zhang et al. 1988; Molinari and Dudek 1992). Such an approach has proven to provide a broader spectrum of interactions between the subgrid- and the grid-scale circulation, and thus, it will also be adopted for the present study.

Using the above-mentioned approach with The Pennsylvania State University/National Center of Atmospheric Research (PSU/NCAR) Mesoscale Model (Anthes et al. 1987), in which the Fritsch–Chappell (1980, hereafter FC) convective scheme and an explicit scheme were incorporated, Zhang et al. (1989, hereafter ZGP) have obtained a successful simulation of an intense squall line that occurred on 10–11 June 1985 during Preliminary Regional Experiments for STORM-Central (PRE-STORM, Cunning 1986). For this case, the Limited-Area Fine-Mesh Model at the National Meteorological Center (NMC) and the spectral model at the Canadian Meteorological Centre (CMC) failed in predicting total precipitation and severe weather events associated with this MCS. Clearly, the coarse grid meshes used at the time in these models (for example T59 for the Canadian spectral model) could partly explain the failure. It is unlikely, however, that the squall system could be well predicted by simply increasing the horizontal resolution to 20–30 km. Therefore, a first objective of this study is to demonstrate, with the Canadian Regional Finite-Element (RFE) Model, the potential for operational models to predict the internal structure and evolution of MCSs and to significantly improve QPFs and severe weather warnings if both high grid resolution and compatible model physics are implemented. A second objective is to determine the sensitivity of the numerical prediction of the 10–11 June 1985 squall line to different implicit and explicit condensation schemes and to different sets of initial conditions.

Mesoscale versions of the RFE model have been applied in the research mode to a wide variety of wintertime meteorological events, including explosive marine cyclogenesis (Benoit et al. 1989; Mailhot et al. 1989; Mailhot and Chouinard 1989), springtime continental cyclonic development (Staniforth and Mailhot 1988), polar air mass transformation (Mailhot 1992), and polar lows (Roch et al. 1991). However, the model has not been fully tested with summertime cases in which larger-scale forcing is relatively weak and the atmosphere is less stable. Hence, the present study represents the first effort to assess more thoroughly the performance of the RFE model in predicting the internal structure and evolution of MCSs, through the case of the 10–11 June 1985 squall system.

The presentation of the results is organized as follows. Section 2 describes the mesoscale version of the RFE model. Section 3 provides verification of the control prediction against detailed observations. Section 4 presents the sensitivity of the model forecast to varying model physics and initial conditions. A summary and concluding remarks are given in the final section.

2. Model system and initialization

The mesoscale version of the RFE model used to simulate the 10–11 June 1985 MCS is very similar to the current version of the operational model. The main differences include (i) a decrease of the horizontal grid size to 25 km (as compared to 50 km in the recently implemented operational version) in the core region of the variable grid (Fig. 1), (ii) the incorporation of an explicit moisture scheme and a more appropriate convective parameterization; and (iii) the enhancement of the CMC analysis to include some mesoscale details. Table 1 summarizes the basic features of the RFE model used for this study.

a. Dynamics

Staniforth and Daley (1979) and Tanguay et al. (1989) provide a detailed description of the dynamical and numerical aspects of the RFE model. The hydrostatic primitive equations in σ coordinates (pressure normalized by surface pressure) are integrated using a semi-implicit temporal discretization and a finite-element spatial discretization. The finite-element tech-

TABLE 1. Summary of the mesoscale RFE model.

Numerics
- 3D hydrostatic primitive equations
- semi-implicit time discretization
- semi-Lagrangian scheme for 3D advection (time step: 300 s)
- linear finite elements in (x, y, σ)
- variable horizontal resolution grid overlaid on a polar stereographic projection (25 km in fine grid)
- 19 σ levels with high resolution in the lowest 150 mb
- second-order horizontal diffusion for temperature, vorticity, and divergence
- 0.5° orography field

Physics
- planetary boundary layer (PBL) based on turbulent kinetic energy
- diagnostic PBL height
- implicit vertical diffusion
- surface energy budget based on force–restore method
- diurnal cycle with solar and infrared fluxes at ground modulated by clouds
- infrared and solar radiation fluxes calculated at all levels
- diagnostic cloud cover
- Fritsch–Chappell scheme for parameterized moist convection
- explicit moisture scheme containing prognostic equations for cloud water/ice and rainwater/snow

nique provides the flexibility to use a uniform, high-resolution mesh in the central domain surrounded by a smoothly varying resolution mesh in which the grid size increases by a constant factor until the equator is reached (Fig. 1). This variable resolution self-nesting strategy is quite useful for regional-scale and mesoscale modeling (Staniforth and Mitchell 1978; Staniforth and Mailhot 1988) and has several advantages (Gravel and Staniforth 1992). Solid wall flow conditions are imposed at the lateral boundaries tangent to the equator. A semi-Lagrangian scheme is used to treat horizontal and vertical advection, which allows a much longer time step (with no loss of accuracy) than Eulerian-based advection schemes whose time step is limited by numerical stability. Here, a time step of 300 s is used for the present model integration with a fine-mesh size of 25 km.

b. Physics

The RFE model contains a comprehensive set, with several options, of parameterization schemes of physical processes (Benoit et al. 1989; Mailhot et al. 1989). In the present study, several important additions and improvements to the physics have been incorporated in order to better address the numerical prediction of summertime MCSs and severe weather events. In particular, a detailed convective parameterization scheme including moist downdrafts and an explicit microphysical scheme have been added. The basic properties of these two schemes are described briefly herein.

In the mesoscale version of the RFE model, an improved version of the Fritsch and Chappell (1980) convective parameterization scheme has been incorporated (Zhang and Fritsch 1986b). In this scheme, the convective available potential energy (CAPE) determines the amount of convective heating, moistening, and precipitation, and it is removed during a convective time scale τ_c (time needed for midlevel winds to advect horizontally the parameterized clouds across one grid length; in the scheme, this parameter is forced to lie between 30 and 60 min). The scheme divides a grid box into three parts: convective updrafts, moist downdrafts, and compensating subsidence. It is assumed that convective effects are dominated by deep clouds; thus, this scheme is most suitable for a grid length of about 20–25 km. Deep convection is triggered when the mixed boundary-layer air is warmer than its environment after it is raised to the lifting condensation level and warmed by a temperature perturbation being proportional to $w^{1/3}$, where w is the grid-scale vertical velocity. The air parcel accelerates upward as long as it is buoyant; it entrains environmental air while moving upward and detrains condensate after reaching the equilibrium level. Moist downdrafts behave in a way similar to updrafts, except that they are initiated at the level of free sink, which is often the level with the minimum equivalent potential temperature (see Fritsch and Chappell 1980). The inclusion of moist downdrafts has been shown to be essential in reproducing many important meso-β-scale structures of MCSs, particularly for those that occurred within weak gradient environments (Zhang and Fritsch 1988; Zhang and Gao 1989).

The resolvable-scale moist physics scheme used follows that described in Hsie et al. (1984), Zhang (1989), and Dudhia (1989). This scheme treats cloud water (ice) and rainwater (snow) as prognostic variables. Thus, two additional equations are solved and the equations for specific humidity and temperature are modified to account for the effects of all diabatic processes. They include (i) virtual temperature in the ideal gas law, (ii) water loading in the hydrostatic equation, (iii) condensation/evaporation, freezing/melting, and sublimation/deposition of condensate, (iv) autoconversion and accretion of cloud water/ice into rainwater/snow, and (v) fallout of rainwater/snow. A simple and economic strategy is adopted to treat cloud water/ice and rainwater/snow, in which the solid phases are allowed to exist at levels with temperature less than 0°C and the liquid phases (i.e., cloud water and rainwater) at temperature above 0°C.

c. Initialization procedures

As in other national centers (e.g., Mills and Seaman 1990; DiMego et al. 1992), CMC has recently implemented a regional data assimilation spinup cycle to replace the previous global analysis system for initializing the RFE model (Chouinard et al. 1994). Apart from providing higher-resolution initial conditions, this

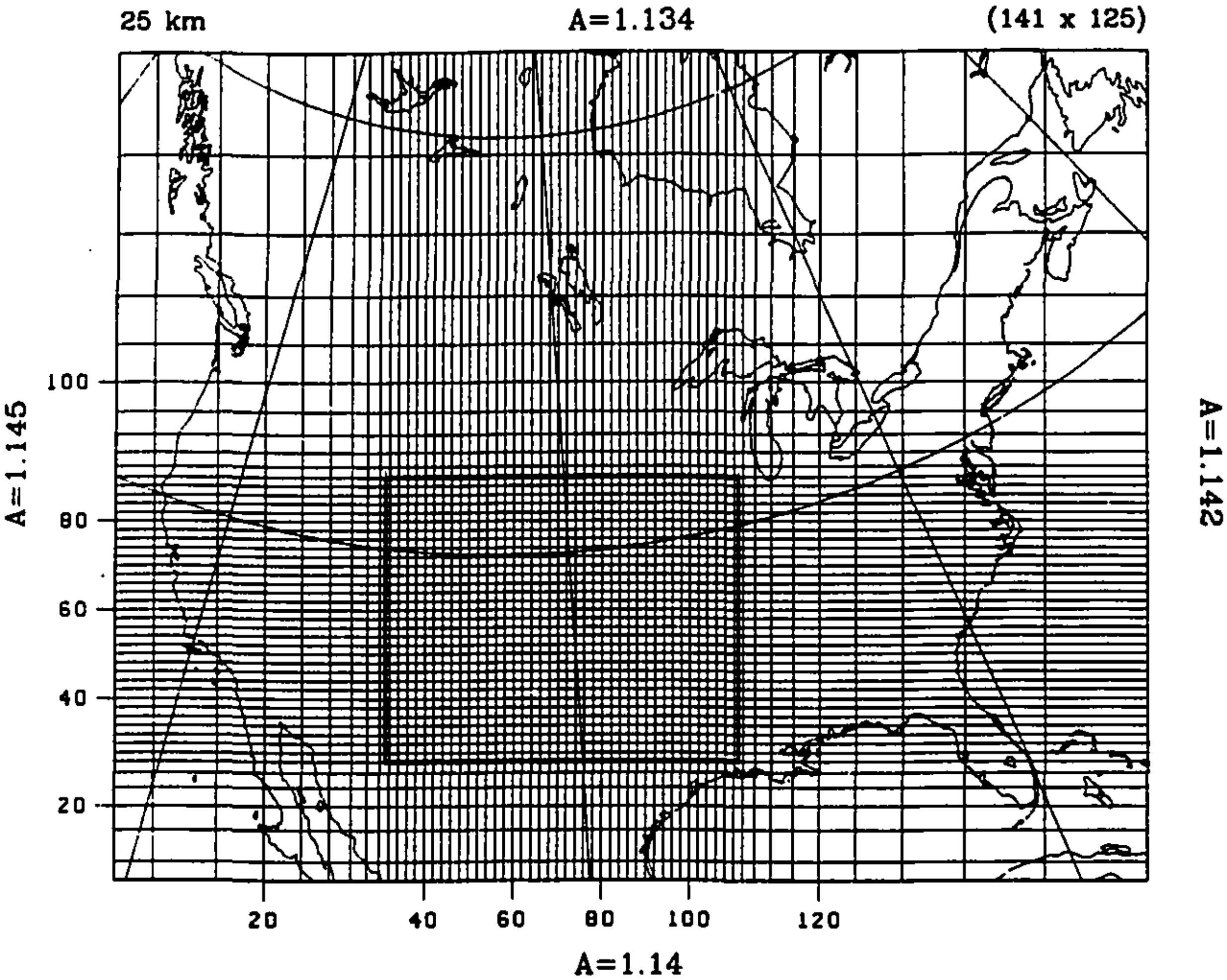

FIG. 1. Portion of the 141 × 125 hemispheric variable grid mesh projected on a polar stereographic plane. The heavy rectangle indicates uniform high resolution of 25 km with the grid size increasing by the constant factors 1.134 northward, 1.142 eastward, 1.140 southward, and 1.145 westward.

assimilation system provides dynamically balanced fields to reduce initial moisture and precipitation spinup problems. However, this regional analysis system was not readily available for the present study, so a simple procedure, described in the following, was adopted to obtain better initial conditions. The RFE model is initialized at 1200 UTC 10 June 1985 with a blend of initial conditions from the CMC archived analysis and the limited-area PSU/NCAR analysis used by ZGP. Specifically, the initialization procedure begins by interpolating the archived CMC objective analysis from low resolution (the resolution was around 300 km at that time) to the variable resolution grid mesh. To add mesoscale details to the CMC analysis, the initial conditions used by ZGP are employed to enhance the analysis over a limited area covering most of North America. The ZGP initial conditions are obtained using the PSU/NCAR analysis package. This analysis essentially uses the NMC global analysis as first-guess fields, which are enhanced with the standard rawinsonde observations over North America using a Cressman-type objective analysis technique (Benjamin and Seaman 1985). The high-resolution fields resulting from this analysis over a limited area are then incorporated into the CMC analysis by a Cressman (1959) analysis and will be referred to as the enhanced analysis (to contrast with the original CMC analysis). No balancing between mass and wind field is done; only the vertically integrated divergence is removed from the wind fields to minimize the noise early in the model integration. No further initialization procedure is performed for the present study. Note that only conventional data are used in the procedures described above, since the PRE-STORM network did not collect supplementary data until 2100 UTC 10 June when the squall line developed and began to move into the network.

3. Model verification

Figure 2 shows larger-scale conditions at the surface and 700 mb at the model initial time (i.e., 1200 UTC 10 June 1985). A southwest–northeast-oriented shallow surface cold front and a midlevel short-wave trough were located in the western part of Colorado. Later, they moved southeast toward the PRE-STORM network and provided an important triggering mechanism for the development of the squall line. A weak surface cyclonic vortex was present near the intersection of Wyoming, Nebraska, and South Dakota. Worthy of notice is the presence of a decaying MCS that was responsible for high relative humidity over the network region at the model initial time. A low-level jet brought warm and moist air over Texas into the PRE-STORM network.

Figure 3 compares the model-predicted sea level pressure, surface temperature, and accumulated rainfall distribution to the mesoscale analysis by Johnson and Hamilton (1988, hereafter referred to as JH). The JH analysis shows that the squall line was initiated around 2100 UTC 10 June ahead of the surface cold front. Then, the squall line intensified rapidly as it propagated southeastward into the network. At 0000 UTC (Fig. 3a), the squall gust front intersected a weak outflow boundary associated with the decaying MCS in eastern Kansas. The squall system entered its mature stage at 0300 UTC (Fig. 3b). Its surface pressure distribution is characterized by a presquall mesolow, a mesohigh, and a wake low. By 0600 UTC, the squall line began to dissipate as it was about to move out of the network (Fig. 3c). A mesohigh and two wake lows were quite evident in the JH analysis. The passage of the squall system during its life cycle has also been well captured by rawinsondes, conventional and Doppler radars, and wind profilers (see JH; Rutledge et al. 1988; Biggerstaff and Houze 1991a,b).

Although the RFE model was initialized with conventional observations, it reproduces very well many observed mesoscale details of the event. First, the model predicts reasonably the initiation of the squall line at nearly the right time and location, and it also captures the dissipating MCS over eastern Kansas and Oklahoma during the initial hours (not shown). At 0000 UTC (Fig. 3d), the predicted squall position and the outflow boundary associated with the decaying MCS conform reasonably well to that observed. Second, as the system moves southeastward and enters the mature stage, the model reproduces the presquall mesolow, mesohighs, and wake lows (Figs. 3e, f). The orientation and propagation of the squall line also compares favorably to the JH analysis. Third, the RFE model predicts a temperature gradient of about 6°C across the squall line, which agrees with the 5°–8°C values analyzed by JH. Note that the arc-shaped portion of the squall line is also well depicted by the forecast. These results are very encouraging, particularly when considering that all these meso-β-scale features are generated from initial conditions using only conventional data. The results suggest that the boundary layer, the convective parameterization scheme, and the explicit moisture physics used in the model are realistic enough to reproduce the evolution of the squall system.

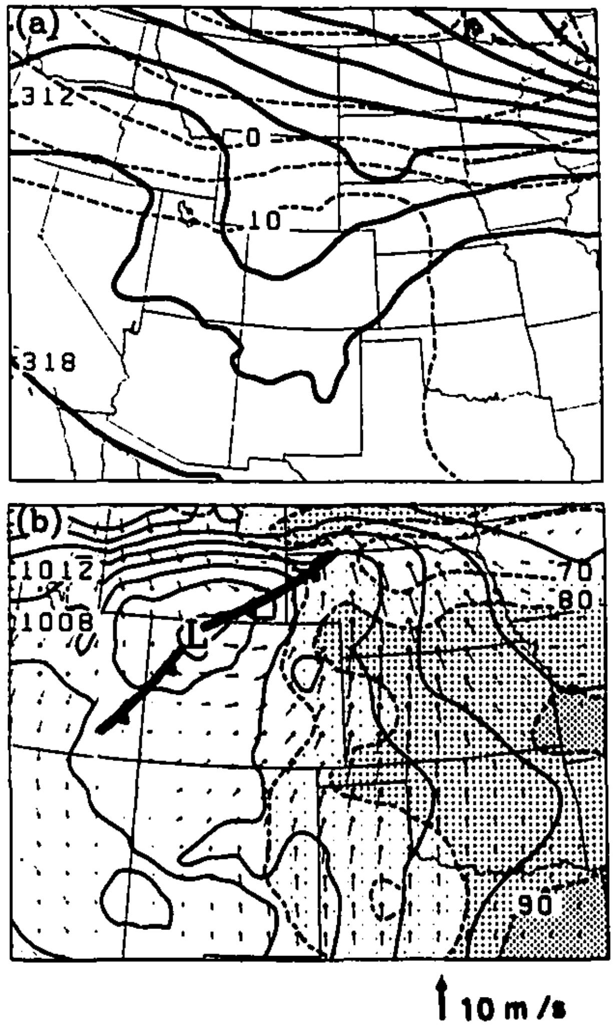

FIG. 2. Enhanced initial conditions at 1200 UTC 10 June 1985. (a) 700-mb geopotential height (solid, every 3 dam) and temperature (dashed, every 5°C); (b) surface relative humidity (dashed, every 10%), surface wind vectors, and sea level pressure (solid, every 2 mb). Different shadings are used to indicate values of relative humidity greater than 70%, 80%, and 90%.

The realistic prediction of the squall system is further evidenced by the evolution of resolvable-scale and parameterized rainfall rates (see Figs. 3g–i). The distribution and orientation resemble the radar reflectivity analysis (Fig. 4) by Rutledge et al. (1988) and the composite radar reflectivity constructed by Biggerstaff and Houze (1991a). Specifically, the model handles reasonably well two different types of precipitation mechanisms, namely, a line of (parameterized or implicit) convective precipitation that is trailed by a zone

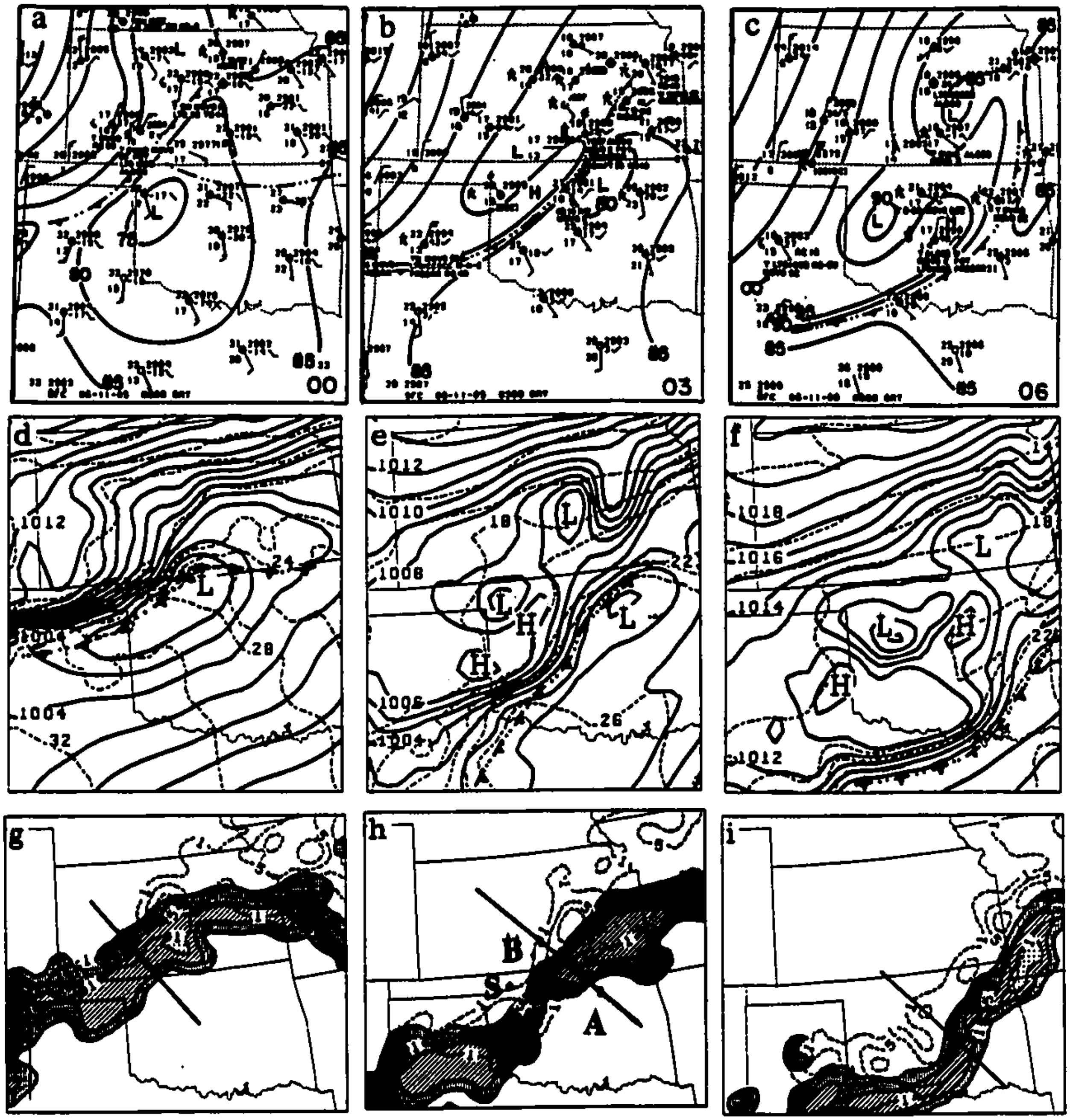

FIG. 3. The upper panel shows surface mesoanalyses from Johnson and Hamilton (1988) at (a) 0000 UTC, (b) 0300 UTC, and (c) 0600 UTC 11 June 1985. Dashed double-dot lines indicate outflow boundaries. Pressures are converted to 518 m; units are in Hg—for example, 85 = 29.85 in Hg (note that 1 in Hg = 33.9 mb). Wind speeds are denoted with a full barb equal to 5 m s^{-1}. The middle panel shows the predicted sea level pressure (solid, every 1 mb) and surface temperature (dashed, every 2°C) from (d) 12-h, (e) 15-h, and (f) 18-h control integration. The lower panel shows the predicted grid-scale (dashed) and convective (shaded) rainfall rates with contours denoting 1, 5, 10, and 20 mm h^{-1} valid at (g) 0000, (h) 0300, and (i) 0600 UTC 11 June 1985. The predicted sounding at point S is given in Fig. 7, and vertical profiles of θ_e ahead and behind the line (points A and B) are shown in Fig. 10.

of (resolvable or explicit) stratiform precipitation. The magnitude of the stratiform precipitation increases with time and reaches its maximum extent near 0600 UTC. It is interesting to note that the model produces one convective rainfall maximum to the south and another one to the north along the leading line during the ma-

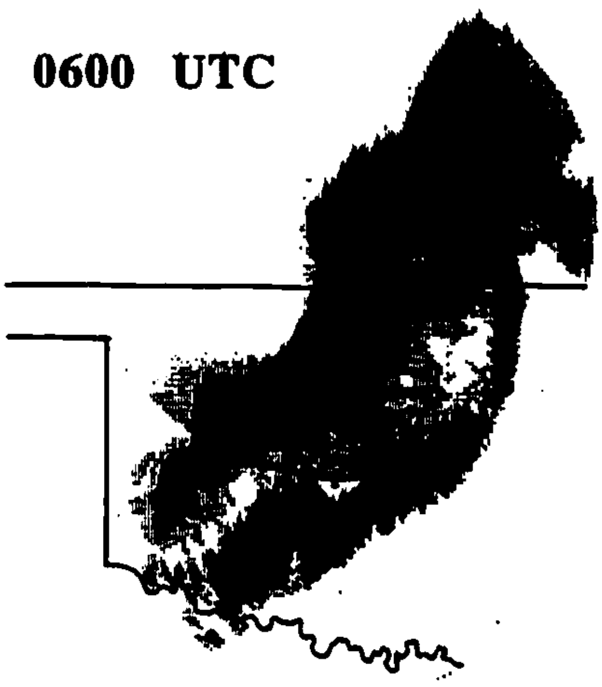

FIG. 4. Radar reflectivity analysis at 0600 UTC 11 June 1985 (from Rutledge et al. 1988).

ture and decaying stages, with two corresponding rainfall maxima in the trailing stratiform region. Between these two types of rainfall maxima there is a zone of weaker precipitation called the "transition zone" (Smull and Houze 1985). According to Biggerstaff and Houze (1991a), the enhanced stratiform precipitation resulted from a cooperative process in which precipitation-sized particles are supplied by the convective portions ahead and increased by condensation/depositional growth in the strong mesoscale ascent (see their Fig. 15).

Figure 5 compares the predicted accumulation of precipitation to the JH analysis. In general, the distribution and amount compare favorably with that observed. For example, the model predicts a maximum of more than 60 mm of total precipitation in the northern part of the PRE-STORM network, of which the implicit (or FC) scheme accounts for 60% of the total production. The explicit scheme also produces a significant fraction of precipitation associated with the squall system, with two maxima located near the major wake lows. Note that the predicted grid-scale precipitation is larger than the analyzed. This appears to be due to the use of different procedures to partition total precipitation into convective and stratiform components. The observational analysis of precipitation in JH is based on the magnitude of relative rainfall rates (i.e., a rainfall rate of <5 mm h^{-1} is defined as "stratiform"; otherwise defined as "convective"), whereas the modeled grid-scale precipitation is generated by grid-box (25 km $\times$ 25 km) saturation, in which some portion could be treated as "convective." Therefore, the predicted stratiform rainfall accounts for roughly 45% of the total accumulations, as compared to 29% analyzed by JH.

Of further importance for this integration is the model's capability to predict other important meso-β-scale elements (see Fig. 6). Specifically, it is encouraging that the model reproduces remarkably well an overturning updraft along the leading line, a front-to-rear (FTR) ascending flow extending from the boundary layer ahead of the system to the trailing stratiform region near the tropopause, and a rear-to-front (RTF) descending flow beneath the stratiform clouds. Note how the area of grid-box saturation and precipitable water content expands rearward as the system evolves. By 0600 UTC, a stratiform region of 300 km in width has formed behind the convective line, with the corresponding internal circulations tilting upshear. This upshear tilt is a typical characteristic of squall systems at the decaying stage (Rotunno et al. 1988). Zhang and Gao (1989) have demonstrated that these circulation structures can be realistically reproduced mainly because of the use of a coupled explicit-convective parameterization package that includes the effects of moist downdrafts. This point will be further shown in the next section. Specifically, with an explicit moisture scheme, condensate is generated in and allowed to move with the FTR ascending flow. As condensate falls into a subsaturated column, grid-scale downdrafts could be induced by cooling from sublimation, melting, and evaporation. As a result of the latent heating and cooling occurring at different locations, various internal structures of the squall system can be induced. In the present case, whether or not the RTF descending flow can be well generated determines the development of other meso-β-scale elements within the squall system (Zhang and Gao 1989; Zhang 1992). As shown in Fig. 6b, the descending flow is most intense along the interface between the leading edge of a dry pocket and the stratiform cloud boundary, thus corresponding to more pronounced cooling by sublimation, melting, and evaporation. Toward the rear, less precipitable water is available for evaporation, so adiabatic warming exceeds diabatic cooling, which gives rise to an onion-shaped sounding near the center of a wake low (see Fig. 7). This process is also responsible for the generation of surface wake lows (see discussions in JH and ZGP). The role of cold outflow (Figs. 3d–f) in helping to trigger new convection ahead of the leading line is also evident from Fig. 6b.

4. Sensitivity experiments

After documenting in the preceding section the remarkable agreement between the predicted and the observed events, it is now possible to use that forecast as a control run to assess the relative importance of various processes in obtaining the successful prediction.

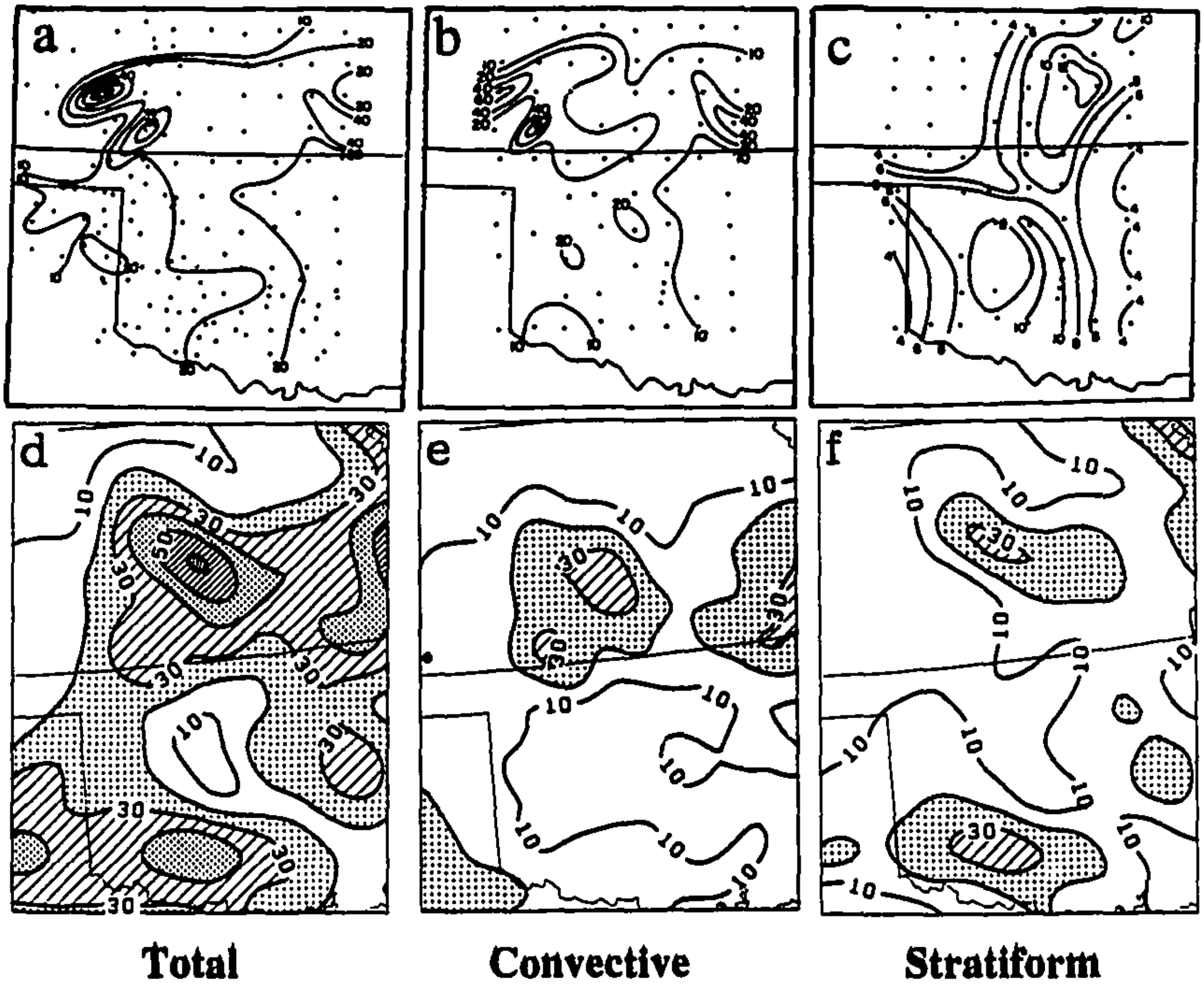

FIG. 5. The upper panel shows the observed accumulated rainfall amount (every 10 mm) analyzed for (a) entire squall system, (b) convective portion, and (c) stratiform portion (from Johnson and Hamilton 1988). The lower panel shows the predicted rainfall amount (every 10 mm) between 2100 UTC 10 June and 1200 UTC 11 June 1985 for (d) total precipitation, (e) convective portion, and (f) grid-scale portion.

This can be done by determining the sensitivity of the model solution to changes in certain parameters while holding all other parameters identical to those in the control run. Four sensitivity experiments are conducted to test the effects of different parameterization schemes for condensation and the impact of the initial conditions (see Table 2). The impacts of evaporation, ice microphysics, parameterized moist downdrafts, and water loading have been investigated by Zhang and Gao (1989), and the effects of using the Arakawa-Schubert (1974) convective scheme has been tested by Grell (1993), both with the PSU/NCAR Mesoscale Model.

a. The moist convective adjustment scheme (MCA)

Due to its attractive simplicity, the moist convective adjustment (MCA) scheme introduced by Manabe et al. (1965) to handle convective precipitation has been widely used in large-scale models (e.g., Kurihara 1973; Krishnamurti et al. 1980) and, until recently, in the operational RFE model. In this scheme, vertical adjustment of temperature and moisture takes place only for the part of the sounding for which the relative humidity and the lapse rate exceeds 90% and the moist adiabatic lapse rate, respectively. Thus, the purpose of this experiment is to examine the performance of the RFE model in predicting the 10–11 June 1985 squall events when the FC implicit scheme is replaced by an MCA-type scheme.

Despite the simplicity of the MCA scheme, the model reproduces a line of intense precipitation that propagates southeastward across the network (see Fig. 8). However, there are several deficiencies with the integration. First, the squall line is initiated around

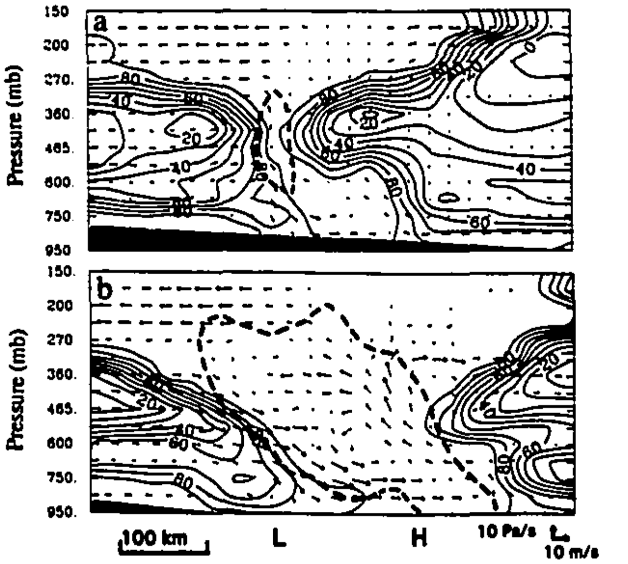

FIG. 6. Vertical cross section of relative humidity (solid lines, every 10%) and precipitable water boundaries (>1 g kg^{-1}, dashed lines), superposed with relative flow vectors normal to the squall line at (a) 0000 UTC and (b) 0600 UTC 11 June 1985. The cross sections are taken along lines given in Figs. 3g,i.

0000 UTC 11 June, which is 3 h later than that in the control run. This delay appears to be related to the initial model spinup problem in which a critical relative humidity value has to be reached before allowing vertical adjustment, whereas in the control run the activation of the FC scheme does not require such a condition to be met. This 3-h delay also accounts for the lag of the predicted squall system in the MCA run. Second, the squall system displays an east–west orientation, as compared to the actual northeast–southwest orientation of the system (cf. Figs. 4 and 8). This could also be attributed to the basic assumption involved in the MCA scheme. Specifically, because of the relatively moist atmosphere over central and eastern Kansas, the convective adjustment and the associated forcing take place earlier than that to the west. This can be seen from the more extensive parameterized and explicit rainfall over the region (see Fig. 8a). Third, the MCA integration produces a wider convective region and a more extensive area of stratiform rainfall, as compared to the control run. In particular, a large area of these two rainfall regimes is overlapped, indicating that much of the explicit heating occurs under convectively unstable conditions. As a result, strong upward motion (>1 m s^{-1}) has developed in the convective region (not shown).

Figure 9 shows the distribution of sea level pressure and surface temperature from 18-h prediction using the MCA scheme. Clearly, the scheme could produce low-level cooling in the lower layers that leads to the generation of strong temperature and pressure gradients across the squall system. However, the model when using the MCA fails to reproduce the mesohighs associated with cold downdrafts (parameterized and resolvable-scale) and wake lows associated with descending rear inflow, even though a significant amount of precipitable water is available behind the convective line. This appears to be attributable to the lack of strong grid-scale cooling. In particular, as suggested by the extensive area of explicit precipitation given in Figs. 8a–c, the atmosphere behind the convective region is saturated throughout the troposphere (not shown), so very weak grid-scale sublimation and evaporation occur. Zhang and Gao (1989) showed that the grid-scale cooling is instrumental in generating the intense descending rear inflow and surface pressure perturbations.

To gain further insight into the role of different convective schemes in stabilizing a vertical column, Fig. 10 displays vertical profiles of equivalent potential temperature (θ_e) that are taken ahead of and behind the squall system. It is obvious that the FC scheme removes efficiently almost all of the CAPE by heating/moistening the upper troposphere and cooling/drying the lower troposphere. In contrast, the MCA scheme produces a deep layer of substantial cooling and drying in the lower half-portion of the atmosphere, but it hardly affects the θ_e profile aloft. Apparently, this is because the vertical adjustment scheme acts only locally and it could not penetrate into the potentially stable layers in the upper troposphere. As a result, the vertical stabilization is not as complete as that in the control run.

b. The Kuo scheme (KUO)

The RFE model physics contains, as an option, the Kuo (1974) cumulus parameterization scheme (see Mailhot et al. 1989) that includes a simplified description of microphysical processes, such as evaporation of precipitation, formation of liquid/solid precipitation, and freezing/melting of precipitation phases. The Kuo scheme is activated when the column-integrated

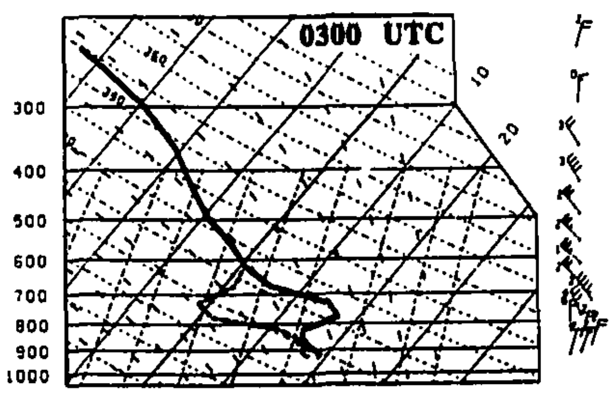

FIG. 7. Predicted sounding near the center of the southern wake low, valid at 0300 UTC 11 June 1985. (See point S in Fig. 3h for the location.)

TABLE 2. Experimental design.

Experiment	Implicit scheme	Explicit scheme	Initial conditions
CONTROL	Fritsch–Chappell	Explicit moisture scheme	Enhanced analysis
MCA	Moist convective adjustment	Explicit moisture scheme	Enhanced analysis
KUO	Kuo	Explicit moisture scheme	Enhanced analysis
SES	Fritsch–Chappell	Simple supersaturation removal	Enhanced analysis
CMC	Fritsch–Chappell	Explicit moisture scheme	CMC analysis

moisture convergence exceeds a critical value and the sounding becomes conditionally unstable. Then a fraction (b) of total moisture convergence is stored and acts to increase the humidity of the column while the remaining fraction ($1 - b$) is condensed and precipitated. Since the Kuo type of convective scheme has been widely used for meso-α-scale or larger-scale simulations of extratropical cyclones, polar lows and MCSs, and also for a number of operational models (e.g., in the Nested-Grid Model at NMC and in the current 50-km version of the operational RFE model at CMC), the purpose of this experiment is to determine if it is capable of reproducing the observed meso-β-scale structures as well as quantitative precipitation associated with the 10–11 June 1985 squall line.

Unlike that with the MCA scheme, the model with the Kuo and explicit moisture schemes is able to initiate the squall line at nearly the right time and location (see Fig. 11). When a grid size of 50 km is used, however, the squall line is not initiated until 0000 UTC (not shown). This 3-h delay is a typical spinup problem associated with coarse-resolution models. Thus, the right timing and location in the current run indicate that the 25-km grid size is appropriate for examining the effects of various model physical processes on the subsequent evolution of the squall system.

While the RFE model with the Kuo scheme predicts reasonably the incipient stage of the squall system, it cannot cause the system to propagate as fast as the observed and the control run. By 0600 UTC, the simulated squall line lags at least 150 km behind. This slowness is again attributable to the lack of cold downdrafts in the Kuo scheme, since downdrafts are important dynamics in the movement of squall lines. Of further significance is that grid-scale precipitation is almost absent throughout the 18-h integration. Obviously, there are two possible reasons for this problem: (i) the convectively induced vertical circulation may be too weak to bring enough moisture upward for triggering grid-box saturation, or (ii) the Kuo scheme may remove too much moisture in a vertical column (i.e., a small "b" parameter), especially in the lower layers. The first possibility is not likely the case after comparing Figs. 3 and 11, for the Kuo scheme run produces greater convective precipitation rates along the leading line during the formative stage than that with the FC scheme. The maximum rainfall rates, generated to the north of the leading line, are of the order of 30 mm h^{-1}, which is equivalent to an average heating rate of 7.5°C h^{-1} throughout a vertical column. A comparison of the vertical θ_e profiles ahead of and behind the convective line indicates that the second possibility is most likely the case. Specifically, Fig. 10 shows that the Kuo scheme reduces substantially the magnitude of θ_e in the lower troposphere after the passage of the line, with little change occurring higher up. This reduction is mainly caused by a decrease in moisture content, since the Kuo scheme does not contain the cooling effect associated with moist downdrafts (also see Fig. 12). On average, the "b" parameter is of the order of 5%–15%. The greatest reduction of θ_e occurs in the lowest layer where ample moisture is stored. This suggests that

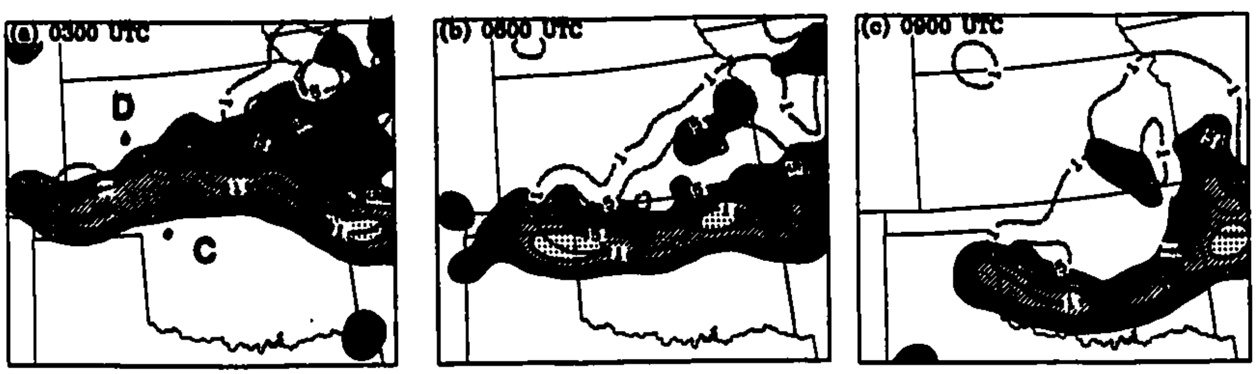

FIG. 8. As in Figs. 3g–i but for experiment MCA (moist convective adjustment). The letters "C" and "D" denote the locations of θ_e profiles shown in Fig. 10.

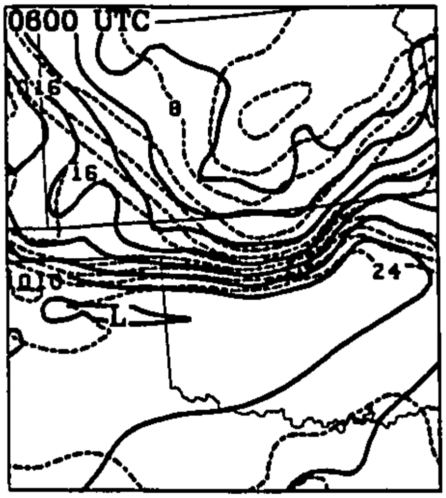

FIG. 9. As in Fig. 3f but for experiment MCA (moist convective adjustment). Note that the isobars are drawn every 2 mb.

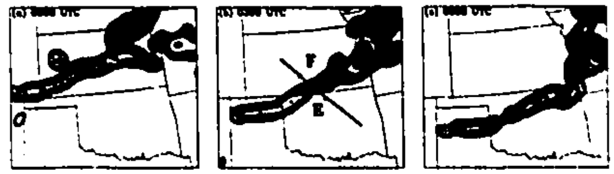

FIG. 11. As in Figs. 3g–i but for experiment KUO. The letters "E" and "F" denote the locations of θ_e profiles shown in Fig. 10.

the convective drying could be excessive in the boundary layer, so the grid-box saturation and grid-scale latent heat release are significantly delayed (Zhang et al. 1988). In the present case, this delay is further aggravated due to the absence of strong larger-scale forcing. By comparison, the FC scheme produces a marginally stable θ_e profile within a deep layer, although it has also removed a similar amount of θ_e in the lowest layer. However, the removed amount of θ_e by the FC scheme results from a combination of cooling and drying associated with moist downdrafts.

Because of the lack of downdraft cooling in the Kuo scheme and because of the negligible effect of grid-scale latent heat release in the present run, the model fails to produce significant surface pressure perturbations, such as mesohighs, wake lows, and cold outflow boundaries (Fig. 12). The elongated pressure trough ahead of the convective line is just a part of the surface frontal system; it can be traced back to the low pressure zone at the model initial time (see Fig. 2b). Similarly, without the downdraft cooling, the model is unable to reproduce the basic internal circulations of the squall system, as shown in Fig. 13b. Apparently, the rear inflow stays elevated as a consequence of little condensate available for evaporation. A well-organized FTR ascending flow does not develop, because the Kuo scheme fails to induce strong mass perturbations in the mid-troposphere and upper troposphere, as can also be seen from Fig. 10. The less significant role of the grid-scale latent heat release is also part of the reason. The results suggest that the Kuo scheme may be only suitable for predicting the timing and location of convective initiation, or the incipient organization of MCSs, but not appropriate for predicting the associated precipitation systems at the mature stage. In contrast, in the control run, the FC scheme tends to efficiently stabilize potentially unstable columns along the leading line and leave behind nearly saturated conditions, and then the explicit scheme takes over to generate latent heating in

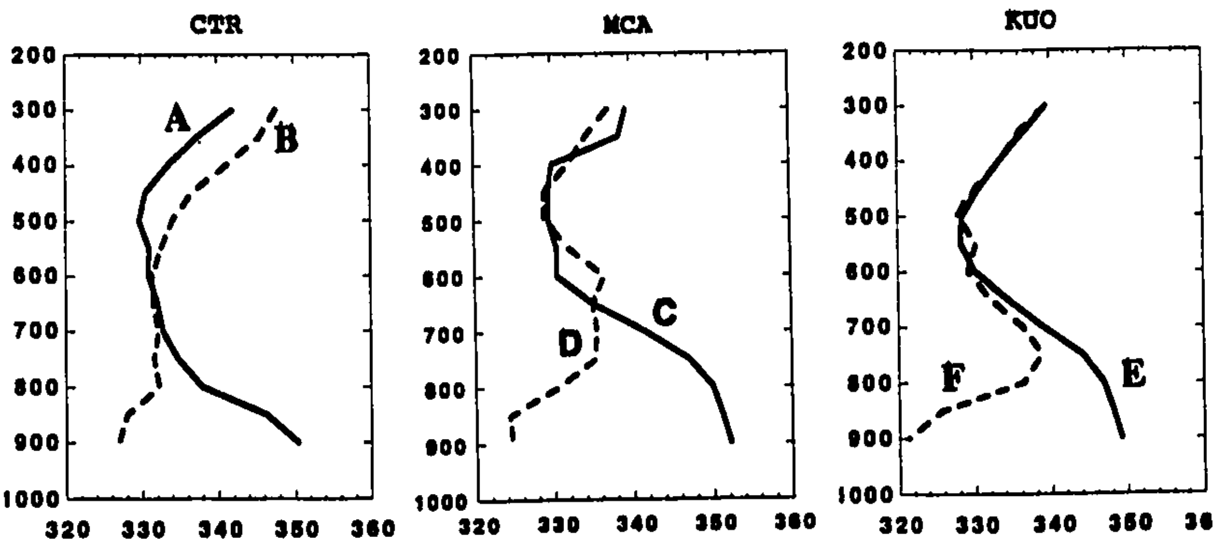

FIG. 10. Predicted equivalent potential temperature (θ_e) profiles taken ahead of and behind the leading convective line from 15-h integrations for (a) control run (see Fig. 3h for the locations), (b) experiment MCA (see Fig. 8a), and (c) experiment KUO (see Fig. 11b).

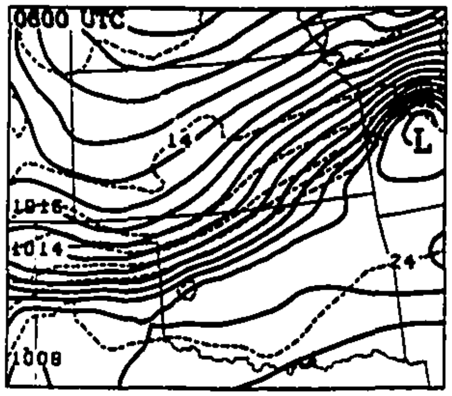

FIG. 12. As in Fig. 3f but for experiment KUO.

the FTR ascending flow and diabatic cooling in the RTF descending flow, thereby leading to the development of a well-organized slantwise circulation in the stratiform region. Such a slantwise circulation is instrumental in the production of stratiform precipitation, based on the analysis of moist potential vorticity by Zhang and Cho (1992).

c. *Simple explicit scheme (SES)*

After examining the model's sensitivity to different convective parameterization schemes, it is natural to evaluate the effect of the explicit moisture scheme, since Zhang et al. (1988) and Molinari and Dudek (1992) have emphasized the importance of coupling the parameterized with explicit convective processes in simulating the internal structure and evolution of MCSs. For this purpose, the prognostic explicit moisture scheme in the control run is replaced by the simple grid-box supersaturation removal scheme described in Mailhot et al. (1989), while subgrid-scale convective processes are still represented with the FC scheme.

It is apparent from Figs. 14 and 15 that use of the simple supersaturation removal scheme produces much less significant changes on the simulation of surface features, as compared to those with different convective parameterization schemes. For example, the orientation and propagation of the leading convection, as well as convective rainfall, are only slightly affected (cf. Figs. 3, 14, and 15), since they are mainly determined by parameterized moist downdrafts. More notable differences appear to the rear of the system. Specifically, the mesohighs and wake lows are significantly weaker and the extent of convectively generated pressure disturbances is much smaller than those in the control run. Because condensate is not allowed to move around, localized grid-scale precipitation develops over some regions. It is interesting that the model still produces reasonably the distribution of grid-scale precipitation that lags behind the parameterized convective precipitation, although the trailing stratiform region is relatively narrower. This phase lag appears to be determined by the squall's internal circulations. Obviously, the development of trailing grid-scale precipitation requires the presence of an FTR ascending flow that can generate and transport a sufficient amount of saturated air mass rearward (Zhang and Cho 1992). Momentum budgets by Gao et al. (1990) indicate that this type of FTR flow develops as a result of convectively generated mesohigh pressures aloft along the leading line, which are in turn determined by the convective heating and moistening. This process also helps explain why the Kuo scheme fails to induce the FTR flow, since it produces little changes of θ_e in the upper levels (cf. Figs. 10a,c).

While use of the supersaturation removal scheme only minimally affects the distribution and amount of surface precipitation, it has important dynamic impacts on the organization of the squall line's internal circulation. In particular, the lack of sublimative melting and evaporative cooling as well as condensate advection, owing to the instantaneous removal of conden-

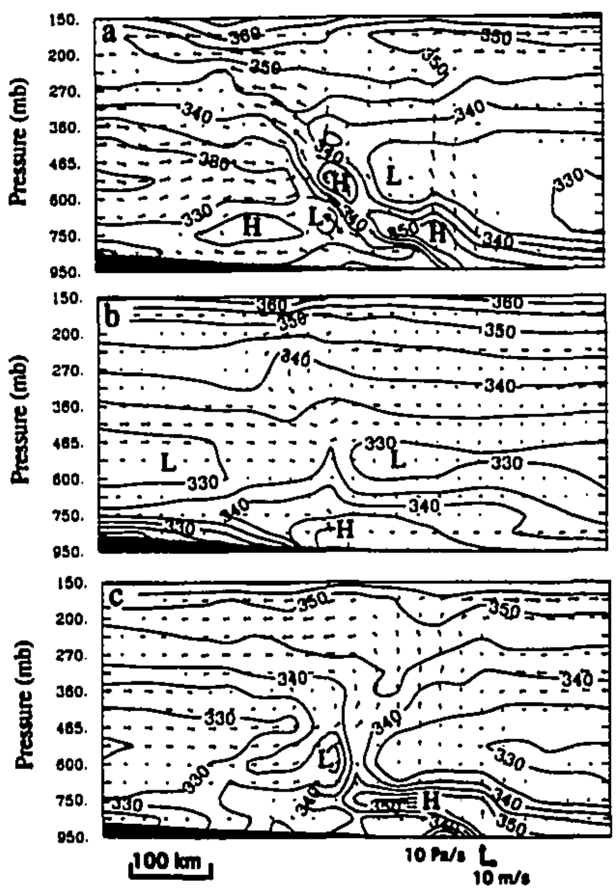

FIG. 13. Vertical cross sections of equivalent potential temperature (θ_e, every 5 K) superposed with relative flow vectors normal to the squall line from 15-h integration for (a) control run (see Fig. 3h for the location), (b) KUO (see Fig. 11b), and (c) SES (see Fig. 14b). The H's and L's refer to the thermal maxima and minima.

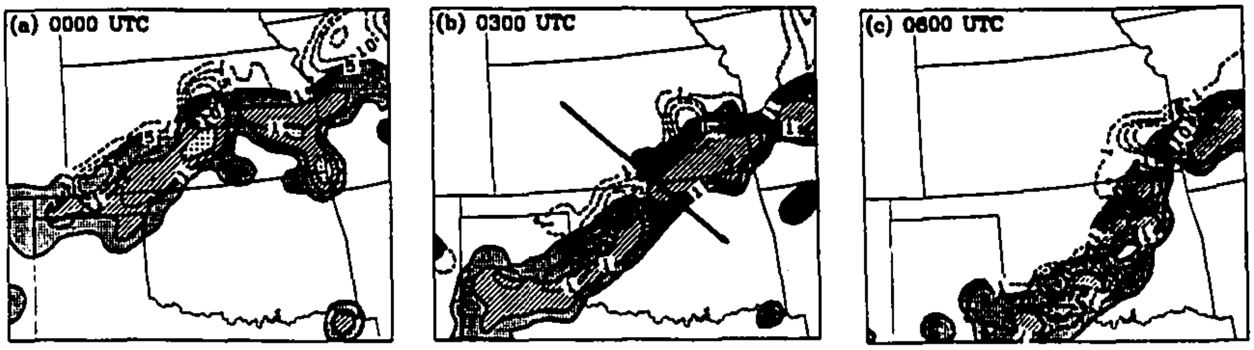

FIG. 14. As in Figs. 3g–i but for experiment SES.

sate, causes the RTF flow to stay elevated. The absence of strong descending rear inflow then leads to the generation of weak wake lows and a less evident arc-shaped structure of the leading line (cf. Figs. 3 and 14). Furthermore, a slantwise FTR ascending flow, present in the control run, never develops in the SES simulation (Weisman 1992). In the present case, horizontal vorticity associated with the FTR inflow appears to be balanced by that of the RTF inflow such that the updrafts along the leading line remain erect during most of the system's life cycle (cf. Figs. 13a,c). Overall, the squall line's circulation is much weaker than that in the control run. Since the vertical thermal structures along the leading line are nearly identical between the control run and experiment SES, the absence of the sloping flow limits the rearward transport of high-θ_e air from the boundary layer, which is crucial in the generation of trailing stratiform precipitation.

d. No enhanced analysis (CMC)

Due to the low resolution of the CMC analysis scheme used in 1985 (i.e., ~300 km), the initial conditions tend to miss certain important mesoscale details, particularly those that may be marginally resolved. For the present case, the CMC analysis produces a much weaker short-wave trough in the midtroposphere (Fig. 16a), a stronger northerly flow behind the surface front, and a slightly drier southerly flow over the PRE-STORM network, as compared to the enhanced analysis used for the control run. In addition, the location and orientation of the surface front as well as the rotational flow structure differ substantially from those in the high-resolution surface observations (cf. Figs. 2b and 16b). Thus, the purpose of this experiment is to examine the sensitivity of the predicted squall system to the use of different initial conditions. In particular, we wish to see how the intensity of the midlevel short wave and the distribution of the surface frontal system would affect the organization of the squall system.

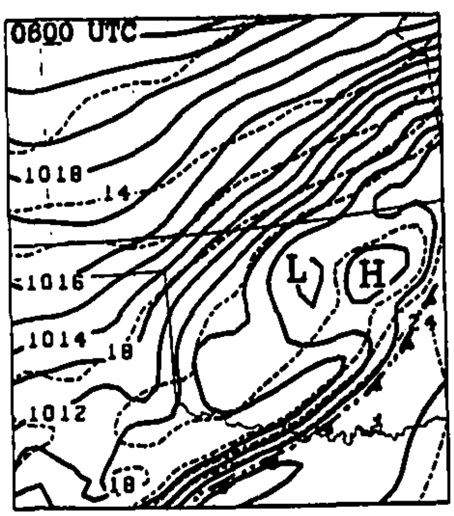

FIG. 15. As in Fig. 3f but for experiment SES.

With the CMC analysis as initial conditions, the model fails to reproduce the decaying MCS that occurred over the network during the initial few integration hours (not shown), although this system has little impact on the later development of the squall line (see ZGP). As expected, the squall line convection is initiated a couple of hours later than in the control run; this is again a typical spinup problem. Consequently, the organization of the squall line's circulation is delayed. Nevertheless, the model simulates well the orientation and propagation of the squall line and its associated convective and grid-scale precipitation after its initiation (see Figs. 17 and 18), except that its location at 0600 UTC lags 150 km behind the observed. Vertical cross sections (not shown) indicate that the model also reproduces the RTF descending and the FTR ascending flow, as evidenced by the predicted presquall mesolows, mesohighs, and wake lows in Fig. 18, but their intensity is much weaker than that in the control run. The results indicate that frontogenesis processes would sooner or later produce organized vertical circulations (Holton 1979) that are favorable for the development of MCSs, as long as the initial conditions contain reasonable magnitudes of baroclinicity. In the present case, cold advection behind the short-

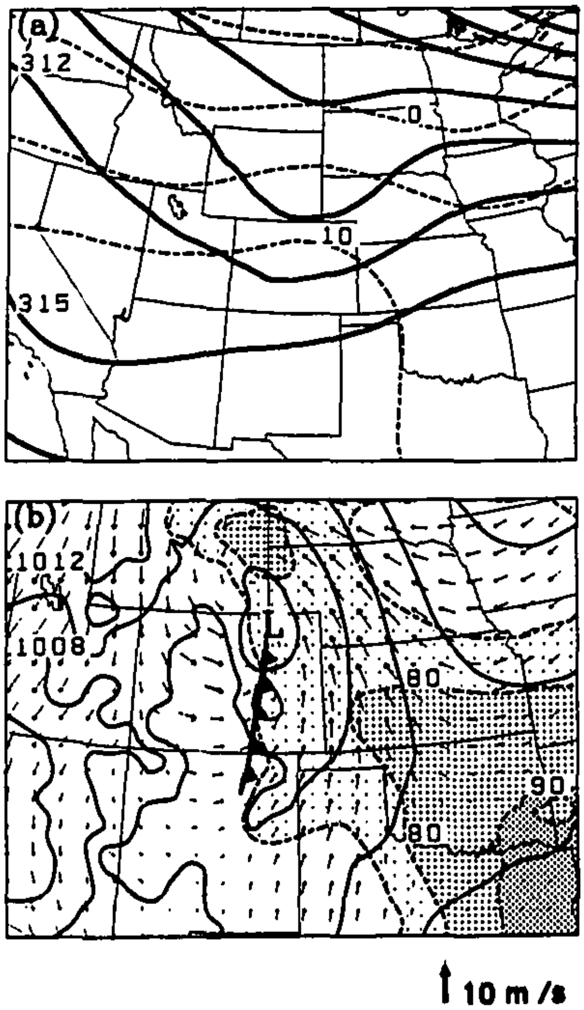

FIG. 16. As in Fig. 2 but from the CMC analysis without data enhancement.

wave trough appears to play an important role in assisting the initial spinup of vertical circulations.

Perhaps one of the most pronounced problems with this forecast is the appearance of a strong low pressure center over southeastern Nebraska. This feature can be traced back to the low pressure at the Colorado–Wyoming–Nebraska border at the initial time (cf. Figs. 2b and 16b). As can be visualized from Fig. 16, the strong cyclonic flow in combination with the pressure pattern has a strong resemblance to a typical extratropical cyclone with the squall line as the cold front part. The squall line forms along the north–south-oriented surface front and moves east with the "cyclone" system. In contrast, with the enhanced initial conditions, the low pressure center at the Colorado–Wyoming border is just a part of the frontal system and is pushed southeast by the cold air behind it. Thus, the low pressure in the control run evolves into an elongated presquall mesolow once the squall line becomes

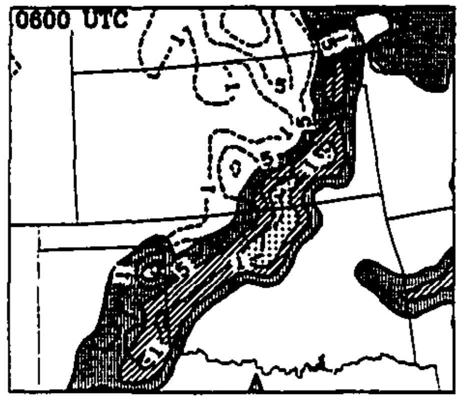

FIG. 17. As in Fig. 3i but for experiment CMC.

organized ahead of the surface front (Figs. 3d–f). In this regard, it is essential to have better-defined mesoscale details, such as baroclinic zones, moist tongues, and convergence zones in the initial conditions in order to obtain more realistic prediction of MCSs and larger-scale environments. Some recent studies have shown that model initial conditions can be readily improved if a regional data assimilation system can be developed to include all available observations (e.g., Miller and Benjamin 1992; Chouinard et al. 1994).

5. Summary and conclusions

In this study, an improved version of the operational Canadian regional finite-element (RFE) model has been used with a fine-mesh grid size of 25 km to examine the feasibility of operational prediction of an intense squall line that occurred during 10–11 June 1985. The model has been tested with different types

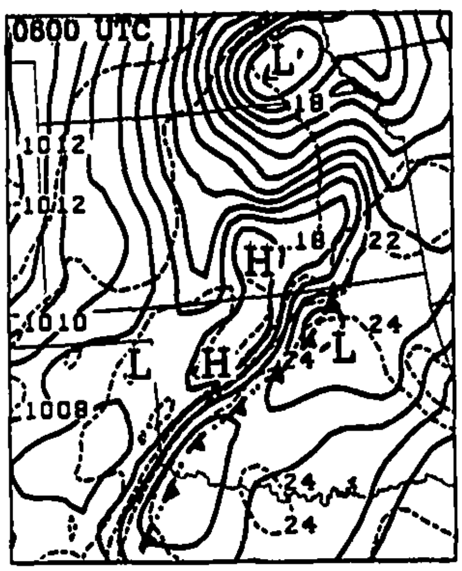

FIG. 18. As in Fig. 3f but for experiment CMC.

of condensation schemes and initial conditions. The study demonstrates the potential for the operational model to improve quantitative precipitation forecasts and severe weather warnings if realistic model physics, reasonable initial conditions, and high resolution are used. The most important conclusions of this study are briefly summarized in the following.

- In addition to focusing on smaller horizontal grid size, which will likely improve the timing and location of convective initiation, equal attention must be paid to improving the explicit moist physics and cumulus parameterizations used if one wants to better reproduce various types of meso-β-scale circulations and their associated precipitation, particularly for MCSs that develop in weak-gradient environments.
- When the Fritsch–Chappell convective parameterization and an explicit moisture scheme are simultaneously used, the RFE model reproduces remarkably well much of the observed internal structure and evolution of the squall system, such as surface mesohighs and mesolows, FTR ascending and RTF descending flows, and a cooling-induced midlevel mesovortex, even though the model is initialized with conventional observations. The predicted timing, location, propagation, and the precipitation amount and distribution of the squall system also compare favorably with the special network observations.
- When either the MCA or the Kuo scheme is incorporated, the model reproduces well the line structure of convective precipitation associated with the squall system. However, both schemes are unable to reproduce the observed internal flow structures of the system, as well as the associated surface pressure and thermal perturbations at the mature and decaying stages, owing partly to the lack of moist downdrafts. In addition, because of their inherent assumptions, the MCA scheme tends to delay the initiation of deep convection, while the Kuo scheme tends to remove too much moisture from the boundary layer such that the grid-scale precipitation is significantly underestimated. Thus, these two schemes do not appear to be suitable for being used to predict the internal structure and evolution of MCSs and their associated precipitation events.
- High-resolution initial conditions obtained from regional data assimilation systems at operational centers will have a positive impact on the successful prediction of the timing and location of MCSs, particularly when the environmental baroclinicity is weak. Poor resolution of mesoscale gradients, such as surface fronts, moist tongues, and convergence zones, may significantly alter the predicted structure and evolution of MCSs. In the present case, with a low-resolution analysis alone, the model produces a "cyclonelike" mesoscale circulation associated with the squall system.

It is important to point out that some of the above conclusions were obtained from a single case study, while others have been supported by previous numerical studies of summertime MCSs (e.g., Zhang and Fritsch 1988; Zhang et al. 1988; Zhang and Gao 1989). Whether or not they are valid for a wide range of circumstances needs to be tested with additional numerical studies of other MCSs. It should also be kept in mind that all the model results presented in this study were produced using a horizontal resolution of 25 km, which is higher than the one typically used in current operational models. Whether or not the preceding conclusions hold with a horizontal resolution of 40–50 km still needs to be verified. The research along this line is currently under way at the Montreal mesoscale community with a view to help improve operational forecasts of MCSs and their associated quantitative precipitation.

Acknowledgments. This work has been made possible through Environment Canada Contract KM156-0-9029 and a graduate fellowship from the Natural Sciences and Engineering Research Council of Canada. The authors are very grateful to Michel Béland of Recherche en Prévision Numérique/Atmospheric Environment Service for his continuing interest and generous support during the course of this project. Thanks also go to Michel Valin, Bernard Bilodeau, Monique Tanguay, André Tremblay, and Mario Lépine at RPN for their kindly assistance.

REFERENCES

Anthes, R. A., E.-Y. Hsie, and Y.-H. Kuo, 1987: Description of the Penn State/NCAR Mesoscale Model Version 4 (MM4). Tech. Note, NCAR/TN-282, 66 pp.

Arakawa, A., and W. H. Schubert, 1974: Interaction of a cumulus cloud ensemble with the large-scale environment, part I. *J. Atmos. Sci.*, **31**, 674–701.

Benjamin, S. G., and N. L. Seaman, 1985: A simple scheme for improved objective analysis in curved flow. *Mon. Wea. Rev.*, **113**, 1184–1198.

Benoit, R., J. Côté, and J. Mailhot, 1989: Inclusion of a TKE boundary layer parameterization in the Canadian Regional Finite-Element Model. *Mon. Wea. Rev.*, **117**, 1726–1750.

Biggerstaff, M. I., and R. A. Houze Jr., 1991a: Kinematic and precipitation structure of the 10–11 June 1985 squall line. *Mon. Wea. Rev.*, **119**, 3034–3065.

——, and ——, 1991b: Midlevel vorticity structure of the 10–11 June 1985 squall line. *Mon. Wea. Rev.*, **119**, 3066–3079.

Chang, C.-B., D. J. Perkey, and C. W. Kreitzberg, 1986: Impact of missing wind observations on the simulation of a severe storm environment. *Mon. Wea. Rev.*, **114**, 1278–1287.

Charba, J. P., and W. H. Klein, 1980: Skill in precipitation forecasting in the National Weather Service. *Bull. Amer. Meteor. Soc.*, **61**, 1546–1555.

Chouinard, C., J. Mailhot, H. Mitchell, A. Staniforth, and R. Hogue, 1994: The Canadian regional data assimilation system: Operational and research applications. *Mon. Wea. Rev.*, **122**, 1306–1325.

Cressman, G. P., 1959: An operational objective analysis system. *Mon. Wea. Rev.*, **87**, 367–374.

Cunning, J. B., 1986: The Oklahoma-Kansas preliminary regional experiment for STORM-Central. *Bull. Amer. Meteor. Soc.*, **67**, 1478–1486.

DiMego, G. J., K. E. Mitchell, R. A. Petersen, J. E. Hoke, J. P. Gerrity, J. C. Tuccilo, R. L. Wobus, and H. H. Juang, 1992: Changes to NMC's regional analysis and forecast system. *Wea. Forecasting*, 7, 185–198.

Dudhia, J., 1989: Numerical study of convection observed during the winter monsoon experiment using a mesoscale two-dimensional model. *J. Atmos. Sci.*, **46**, 3077–3107.

Fawcett, E. B., 1977: Current capabilities in prediction at the National Weather Service's National Meteorological Center. *Bull. Amer. Meteor. Soc.*, **58**, 143–149.

Frank, W. M., 1983: The cumulus parameterization problem. *Mon. Wea. Rev.*, **111**, 1859–1871.

Fritsch, J. M., and C. F. Chappell, 1980: Numerical prediction of convectively driven mesoscale pressure system. Part I: Convective parameterization. *J. Atmos. Sci.*, **37**, 1722–1733.

——, and K. F. Heideman, 1989: Some characteristics of the Limited-Area Fine-Mesh (LFM) Model quantitative precipitation forecasts (QPF) during the 1982 and 1983 warm seasons. *Wea. Forecasting*, **4**, 173–185.

——, R. A. Maddox, and A. G. Barnston, 1981: The character of mesoscale convective complex precipitation and its contribution to warm season rainfall in the U.S. Preprints, *Fourth Conf. Hydrometeorology*, Reno, NV, Amer. Meteor. Soc., 94–99.

Gao, K., D.-L. Zhang, M. W. Moncrieff, and H.-R. Cho, 1990: Mesoscale momentum budget in a midlatitude squall line: A numerical case study. *Mon. Wea. Rev.*, **118**, 1011–1028.

Gravel, S., and A. Staniforth, 1992: Variable resolution and robustness. *Mon. Wea. Rev.*, **120**, 2633–2640.

Grell, G. A., 1993: Prognostic evaluation of assumptions used by cumulus parameterizations. *Mon. Wea. Rev.*, **121**, 764–787.

Heideman, K. F., and J. M. Fritsch, 1988: Forcing mechanisms and other characteristics of significant summertime precipitation. *Wea. Forecasting*, **3**, 115–130.

Holton, J. R., 1979: *An Introduction to Dynamic Meteorology*. 2d ed. Academic Press, 391 pp.

Hsie, E.-Y., R. A. Anthes, and D. Keyser, 1984: Numerical simulation of frontogenesis in a moist atmosphere. *J. Atmos. Sci.*, **41**, 2581–2594.

Johnson, R. H., and P. J. Hamilton, 1988: The relationship of surface pressure features to the precipitation and airflow structure of an intense midlatitude squall line. *Mon. Wea. Rev.*, **116**, 1444–1472.

Kelly, G. A. M., G. A. Mills, and W. L. Smith, 1978: Impact of *Nimbus-6* temperature soundings on Australian region forecasts. *Bull. Amer. Meteor. Soc.*, **49**, 393–405.

Krishnamurti, T. N., Y. Ramanathan, H.-L. Pan, R. L. Pasch, and J. Molinari, 1980: Cumulus parameterization and rainfall rates. I. *Mon. Wea. Rev.*, **108**, 465–472.

Kuo, H. L., 1974: Further studies of the parameterization of the influence of cumulus convection on large-scale flow. *J. Atmos. Sci.*, **31**, 1232–1240.

Kurihara, Y., 1973: A scheme for moist convective adjustment. *Mon. Wea. Rev.*, **101**, 547–553.

Mailhot, J., 1992: Numerical simulation of air mass transformation over the Gulf of Mexico. *J. Appl. Meteor.*, **31**, 946–963.

——, and C. Chouinard, 1989: Numerical forecasts of explosive winter storms: Sensitivity experiments with a meso-α scale model. *Mon. Wea. Rev.*, **117**, 1311–1343.

——, and ——, R. Benoit, M. Roch, G. Verner, J. Côté, and J. Pudykiewicz, 1989: Numerical forecasting of winter coastal storms during CASP: Evaluation of the Regional Finite-Element Model. *Atmos.-Ocean*, **27**, 24–58.

Manabe, S., J. Smagorinsky, and R. F. Strickler, 1965: Simulated climatology of a general circulation model with a hydrologic cycle. *Mon. Wea. Rev.*, **93**, 769–798.

Miller, P. A., and S. G. Benjamin, 1992: A system for the hourly assimilation of surface observations in mountainous and flat terrain. *Mon. Wea. Rev.*, **120**, 2342–2359.

Mills, G. A., and R. S. Seaman, 1990: The BMRC regional data assimilation system. *Mon. Wea. Rev.*, **118**, 1217–1237.

Molinari, J., and M. Dudek, 1992: Parameterization of convective precipitation in mesoscale numerical models: A critical review. *Mon. Wea. Rev.*, **120**, 326–344.

Ramage, C. S., 1982: Have precipitation forecasts improved? *Bull. Amer. Meteor. Soc.*, **63**, 739–743.

Roch, M., R. Benoit, and N. Parker, 1991: Sensitivity experiments for polar low forecasting with the CMC Mesoscale Finite-Element Model. *Atmos.-Ocean*, **29**, 381–419.

Rotunno, R., J. B. Klemp, and M. L. Weisman, 1988: A theory for strong, long-lived squall lines. *J. Atmos. Sci.*, **45**, 463–485.

Rutledge, S. A., R. A. Houze Jr., M. I. Biggerstaff, and T. Matejka, 1988: The Oklahoma–Kansas mesoscale convective system of 10–11 June 1985: Precipitation structure and single Doppler radar analysis. *Mon. Wea. Rev.*, **116**, 1409–1430.

Sanders, F., 1979: Trends in skill of daily forecasts of temperature and precipitation, 1966–78. *Bull. Amer. Meteor. Soc.*, **60**, 763–769.

Smull, B. F., and R. A. Houze Jr., 1985: A midlatitude squall line with a trailing region of stratiform rain: Radar and satellite observations. *Mon. Wea. Rev.*, **113**, 117–133.

Staniforth, A. N., and H. L. Mitchell, 1978: A variable-resolution finite-element technique for regional forecasting with the primitive equations. *Mon. Wea. Rev.*, **106**, 439–447.

——, and R. W. Daley, 1979: A baroclinic finite-element model for regional forecasting with the primitive equations. *Mon. Wea. Rev.*, **107**, 107–121.

——, and J. Mailhot, 1988: An operational model for regional weather forecasting. *Comput. Math. Appl.*, **16**, 1–22.

Tanguay, M., A. Simard, and A. N. Staniforth, 1989: A three-dimensional semi-Lagrangian scheme for the Canadian Regional Finite-Element Forecast Model. *Mon. Wea. Rev.*, **117**, 1861–1871.

Weisman, M. L., 1992: The role of convectively generated rear-inflow jets in the evolution of long-lived mesoconvective systems. *J. Atmos. Sci.*, **49**, 1826–1847.

Zhang, D.-L., 1989: The effect of parameterized ice microphysics on the simulation of vortex circulation with a mesoscale hydrostatic model. *Tellus*, **41A**, 132–147.

——, 1992: The formation of a cooling-induced mesovortex in the trailing stratiform region of a midlatitude squall line. *Mon. Wea. Rev.*, **120**, 2763–2785.

——, and J. M. Fritsch, 1986a: A case study of the sensitivity of numerical simulation of mesoscale convective systems to varying initial conditions. *Mon. Wea. Rev.*, **114**, 2418–2431.

——, and ——, 1986b: Numerical simulation of the meso-β scale structure and evolution of the 1977 Johnstown flood. Part I: Model description and verification. *J. Atmos. Sci.*, **43**, 1913–1943.

——, and ——, 1988: Numerical sensitivity experiments of varying model physics on the structure, evolution and dynamics of two mesoscale convective systems. *J. Atmos. Sci.*, **45**, 261–293.

——, and K. Gao, 1989: Numerical simulation of an intense squall line during 10–11 June 1985 PRE-STORM. Part II: Rear inflow, surface pressure perturbations and stratiform precipitation. *Mon. Wea. Rev.*, **117**, 2067–2094.

——, and H.-R. Cho, 1992: The development of negative moist potential vorticity in the stratiform region of a simulated squall line. *Mon. Wea. Rev.*, **120**, 1322–1341.

——, E.-Y. Hsie, and M. W. Moncrieff, 1988: A comparison of explicit and implicit predictions of convective and stratiform precipitating weather systems with a meso-β scale numerical model. *Quart. J. Roy. Meteor. Soc.*, **114**, 31–60.

——, K. Gao, and D. B. Parsons, 1989: Numerical simulation of an intense squall line during 10–11 June 1985 PRE-STORM. Part I: Model verification. *Mon. Wea. Rev.*, **117**, 960–994.

Chapter 4

The 14 July 1987 intense convective system. Part I: Gravity waves and the squall line

4.1 Presentation of article 2

Following the results given in the preceding chapter, the model is now used as a tool to help understand the dynamical and physical processes leading to particular mesoscale structures within two intense squall line systems. The first of these two squall lines is examined in the next two chapters. This convective system occurred during July 1987 and was responsible for severe weather and intense precipitation over Montreal (see Bellon et al. 1993; Tremblay 1994).

In this chapter, the model prediction of the squall line is first carefully verified against all available observations (i.e., radar and satellite images, surface analyses, etc.). It is hypothesized that the propagation and intensification of the squall line are associated with gravity waves, through wave-CISK mechanisms (Xu and Clark 1984; Raymond 1984). This hypothesis is examined through a series of sensitivity experiments in which we determine if the model-produced oscillations would have the characteristics of gravity waves, and then we evaluate the respective roles of the waves and convection in the intensification of the system. After the relationship between the waves and deep convection is found, the sensitivity of the predicted waves-convection interactions to different convective parameterizations is investigated.

4.2 Article 2

Numerical prediction of an intense convective system associated with the July 1987 Montreal flood. Part I: Gravity waves and the squall line. By Stéphane Bélair, Da-Lin Zhang, and Jocelyn Mailhot.

Accepted for publication in *Atmos.-Ocean*, December 1994.

Abstract

In this study, a 24-h high-resolution numerical prediction of a prefrontal squall line associated with the 14 July 1987 Montreal flood is employed to investigate the origin and role of mesoscale gravity waves in the development of the squall system. The 24-h integration using an improved mesoscale version of the Canadian regional finite-element model is first validated against available observations, and then non-observable features are diagnosed to reveal the relationship between deep convection and gravity wave events.

It is shown that the model reproduces well many aspects of the squall line, such as the propagation and organization of the convective system, as well as its associated precipitation. It is found that gravity waves are first excited near Lake Erie, following the initiation of early convective activity. Then, these waves propagate eastward and northeastward at speeds of 20 and 35 m s^{-1}, respectively. As the waves propagate downstream, deep convection radiates rapidly behind the wave trough axis, forming a long line of squall convection. Because the squall line moves with the gravity waves in a "phase-locked" manner, deep convection has a significant influence on the structure and amplitude of the gravity waves. The sensitivity of the wave-squall prediction to various parameters in convective parameterization is also examined.

1. Introduction

Numerous observational studies have shown the importance of gravity waves in the initiation and maintenance of mesoscale convective systems (MCSs) (Uccellini, 1975; Balachandran, 1980; Miller and Sanders, 1980; Stobie et al., 1983; Bosart and Sanders, 1986; Einaudi et al., 1987; Koch et al., 1988). Several theories have been proposed to explain the generation of mesoscale gravity waves, which include convectively induced, shearing instability and geostrophic adjustment. For example, Wagner (1962), Ferguson (1967), and Bosart and Cussen (1973) showed the collocation of convective activity with solitary waves having wavelength on the order of 100 km. Lin and Goff (1988) documented the propagation of a convectively generated intense solitary wave. They used a simple analytical model to show that a midlevel latent heat perturbation can produce a single wave of depression in an inversion layer. In contrast, Uccellini and Koch (1987), in their review of 13 gravity wave cases, found no strong correlation between gravity waves and deep convection. They noted, however, the presence of an upper-level jet streak in each of these cases. Gravity waves appear to be preferably initiated to the south of the exit region of the jet streak, suggesting that shearing instability or geostrophic adjustment was operative.

Once the gravity waves are excited, they travel both horizontally and vertically in the stratified atmosphere. Pecnick and Young (1984) showed that these waves will decay rapidly if there is no mechanism to trap the low-level wave energy. Crook (1988) found that the decaying time scale is shorter than one oscillation when the low-level energy can not be trapped. Consequently, some type of ducting mechanisms must exist in the atmosphere to explain the persistent propagation of gravity waves if no other mechanisms are acting to sustain them. Lindzen and Tung (1976) suggested that a low-level statically stable layer underneath a conditionally unstable layer including a critical level and a large vertical wind shear would be sufficient conditions for an efficient ducting of low-level gravity waves. Uccellini and Koch (1987) noted that most of these conditions were met for the 13 cases they examined, thus supporting the ducting concept developed by Lindzen and Tung.

On the other hand, gravity waves can help trigger convective activity in an environment having positive convective available potential energy (CAPE). When the induced convection is organized into an MCS, the resulting convective forcing could modify characteristics of gravity waves (i.e., wavelength, phase speed, and amplitude). Koch et al. (1988) were able to isolate the effects of convection on the characteristics of observed gravity waves that remained in phase with convection for a few hours. They noted that the amplitude of the waves increases but their wavelength and phase speed decrease in the presence of deep convection. By comparison, Bosart and Sanders (1986) observed acceleration of a gravity wave associated with convective activity. Thus, one must be cautious in drawing general conclusions from only one case study.

Of particular interest are the studies reporting the "phase-locking" between gravity waves and convection (e.g., Miller and Sanders, 1980; Stobie et al., 1983; Einaudi et al., 1987; Zhang and Fritsch, 1988a; Ramamurthy et al., 1993). This phase-locking scenario suggests the operation of the positive feedback mechanism by which gravity waves provide the necessary low-level convergence to initiate new convection, whereas latent heating and cooling amplify the waves. Analytical models developed by Lindzen (1974) and Raymond (1975, 1976), known as wave-CISK, reproduced certain characteristics of such a wave-convection coupled system with some success. Based on the same idea, more realistic wave-CISK models have been developed by Xu and Clark (1984) and Raymond (1984). Note, however, that even the latest version of wave-CISK could hardly provide a full understanding of the interaction of gravity waves with MCSs.

Up to now, only few real-data studies have used numerical models to investigate gravity waves. Indeed, with the exception of Zhang and Fritsch (1988a), Cram et al. (1992a), Powers and Reed (1993) and Tremblay (1994), past advances in the understanding of different aspects of gravity waves and their interaction with MCSs are limited to either observational studies or analytical models. In this paper, we shall investigate the interaction of an MCS with gravity waves, using a 24-h high resolution prediction of a prefrontal squall line that occurred on 14 July 1987 over Quebec and the northeastern United States with an improved version of the Canadian regional finite-element (RFE) model. We are motivated to study the development of this squall system because of i) the importance of gravity waves interacting with convection in the generation of heavy rainfall over Montreal and ii) the development of some non-classical circulations in the trailing stratiform region of the MCS. The latter will be described in Part II of this series of papers (Bélair et al., 1995a). The objectives of the present study are to a) investigate the mesoscale predictability of the internal structure, precipitation and life cycle of the squall system, as verified against available observations; b) examine the roles of the gravity waves in the development of the squall line; and c) determine the sensitivity of the gravity waves-convection structures to different parameterizations of convective processes. As part of the understanding, we will also examine, through a series of numerical sensitivity experiments, the roles of different model physical processes in the generation of various mesoscale components of the squall system.

It should be mentioned that Tremblay (1994) has also studied the generation of gravity waves associated with the 14 July 1987 Montreal flood episodes. However, Tremblay's study focused more on the ability of a fully compressible model in simulating the development of the MCS. Furthermore, the model he used does not include diurnal variations and boundary-layer processes, and it contains the Manabe convective scheme coupled with a simple precipitation physics package. With the improved version of the RFE model, we felt that a more realistic simulation of the gravity waves and their roles in generating the heavy rainfall can be obtained.

The presentation of this study is organized as follows. The next section describes briefly the RFE model. Section 3 provides verification of the model prediction of the convective events against available observations. Section 4 shows evidence of gravity waves along with their structures. Section 5 discusses the interaction of the squall line with the gravity waves. Concluding remarks are given in the final section.

2. Model description

The numerical model used for the present study is a state-of-the-art mesoscale research version of the RFE model, which is currently operational for short-range forecast at the Canadian Meteorological Center (CMC). The main features of the model are summarized in Table 1. Since the model configuration is similar to that used in Bélair et al. (1994), only a brief discussion of model features particular to this study is given here.

In this study, the central domain of the variable-resolution grid includes Quebec and the Northeastern United States and has a uniform grid size of 25 km (Fig. 4.1). In the RFE model, the hydrostatic primitive equations are integrated using a semi-implicit technique for the temporal discretization. It should be mentioned that the use of this technique may degrade the prediction of gravity waves by slowing their phase speeds (Haltiner and Williams, 1980). However, it can be easily shown that for waves with characteristics similar to those studied here (i.e., wavelengths of 200 km and phase speeds of 20 m s^{-1}), the error in phase speed resulting from the semi-implicit technique is less than 3 %. Also, since the horizontal scale of the waves is much greater than the vertical scale, the hydrostatic approximation is appropriate for their numerical study. Another aspect of the RFE model that may affect the generation of gravity waves is the use of the upper boundary-condition, i.e., $\dot{\sigma} = d\sigma/dt = 0$, where σ is the pressure normalized by surface pressure. This type of upper boundary condition may produce spurious wave reflection at the top. To alleviate such problems, the waves are artificially damped near the model top by substantially increasing the vertical diffusion coefficient for the three highest model levels, which serve as a sponge layer.

The comprehensive set of parameterization schemes contained in the RFE model is described in detail by Benoit et al. (1989) and Mailhot et al. (1989). Some additions and improvements have been incorporated into the model in order to better address the prediction of summertime MCSs and severe weather events (Bélair et al., 1994). In particular, the Fritsch and Chappell (1980; hereafter referred to as FC) convective scheme, also described in Zhang and Fritsch (1986), has been implemented and coupled with a grid-scale condensation scheme described by Hsie et al. (1984), Zhang (1989) and Dudhia (1989).

The model is initialized at 0000 UTC 14 July 1987 (i.e., in the evening preceding the Montreal flood) using the CMC's archived hemispheric analysis. The model initial conditions are obtained using the implicit normal-mode initialization procedure described by Temperton and Roch (1991), in which all the physical processes are turned off.

3. Model verification

In this section, we provide an overview of the evolution of the squall line that was responsible for heavy rainfall events and validate the RFE model prediction against all available observations (e.g., surface analyses, rawinsondes, satellite and radar imagery). The radar imagery at Buffalo (not shown) indicates that this intense convective system was initiated in the vicinity of a surface cold front over Lakes Ontario and Erie around 0800 UTC 14 July and moved both northeastward (in the direction of an upper-level jet stream) and eastward. Besides the heavy precipitation that occurred over Montreal, vigorous convective activity was observed in the New England states and north of Quebec City.

The large-scale environment in which the squall line was embedded was characterized by a pronounced synoptic-scale trough (L ~ 4500 km) and a deep layer of a baroclinic zone with a temperature gradient of about 12 °C $(1000\ \mathrm{km})^{-1}$ at 500 hPa (Fig. 4.2a). At upper levels, there was a jet streak with a maximum wind speed of 50 m s^{-1} located ahead of the trough axis (Fig. 4.2b). As the large-scale pressure system advanced eastward, it caused a pressure drop of about 6 hPa during the next 12 h over the Montreal-Ottawa area.

TABLE 4.1: Summary of the mesoscale RFE model

Numerics

- 3-D hydrostatic primitive equations;
- semi-implicit time discretization;
- semi-Lagrangian scheme for 3D advection (time step: 300s);
- linear finite-elements in (x,y,σ);
- variable horizontal resolution grid overlaid on a polar stereographic projection (25 km in fine mesh grid);
- 23 σ levels with high resolution in the lowest 150 hPa;
- second order horizontal diffusion for temperature, vorticity, and divergence;
- 0.5° orography field.

Physics

- Planetary boundary layer (PBL) based on turbulent kinetic energy;
- diagnostic PBL height;
- implicit vertical diffusion;
- surface energy budget based on force-restore method;
- diurnal cycle with solar and infrared fluxes at the ground modulated by clouds;
- infrared and solar radiation fluxes calculated at all levels;
- diagnostic cloud cover;
- Fritsch-Chappell scheme for parameterized moist convection;
- explicit moisture scheme containing prognostic equations for cloud water/ice and rainwater/snow.

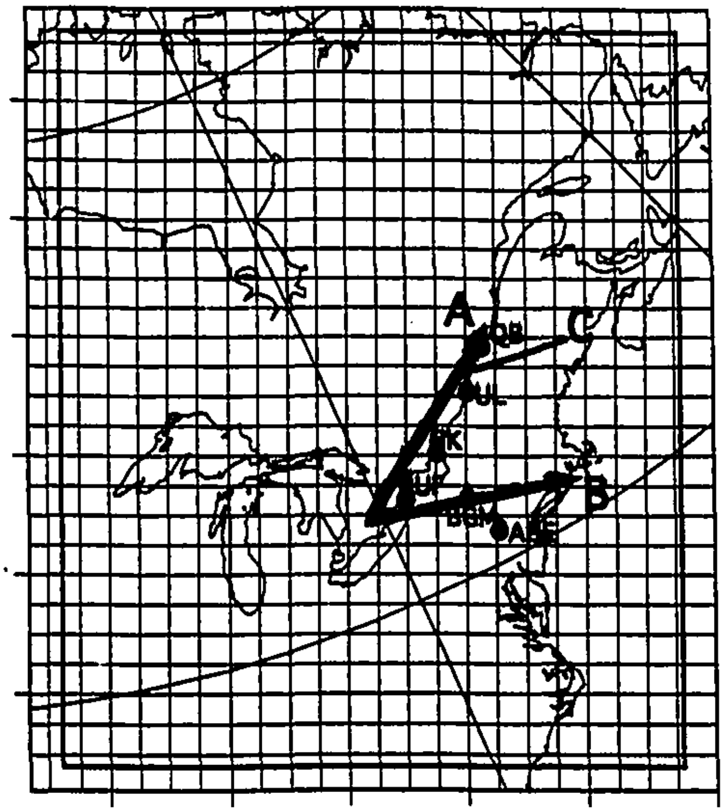

Fig. 4.1 Portion of the 165 x 185 hemispheric variable grid mesh projected on a polar stereographic plane. The heavy rectangle indicates the central window with a uniform grid size of 25 km. Horizontal and vertical lines are drawn every 5 model grid points. Propagation tracks A and B as well as all the stations referred to in the text are indicated.

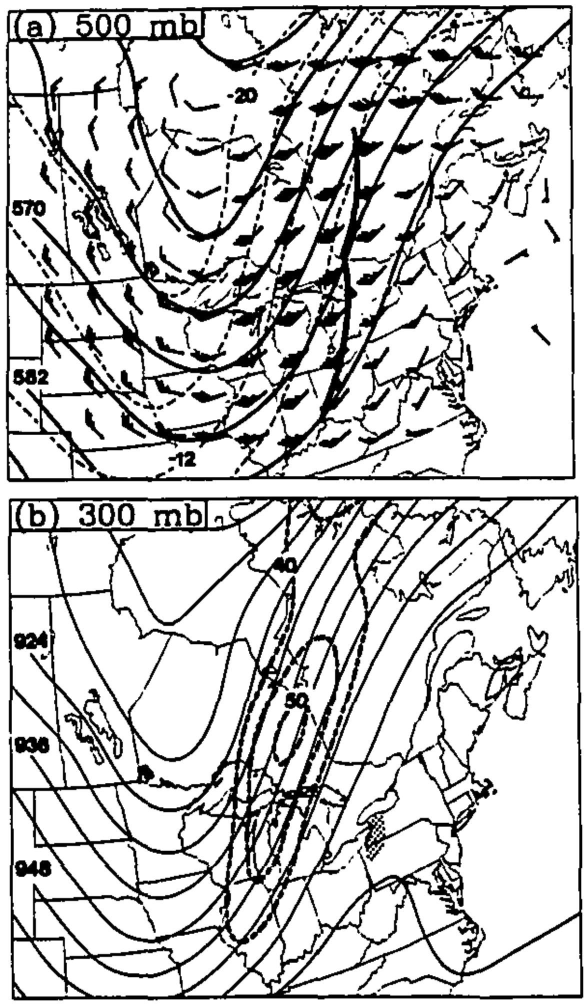

Fig. 4.2 The model initial conditions (i.e., 0000 UTC 14 July 1987): a) geopotential height (solid, every 6 dam) and temperature (dashed, every 4 °C) superposed with horizontal winds (a full barb is 5 m s^{-1}) at 500 hPa. The position of the surface front is indicated. b) geopotential height (solid, every 6 dam) and wind speeds (dashed, every 5 m s^{-1}) at 300 hPa. Shadings denote the area of the predicted convection valid at 1200 UTC 14 July.

Although the prestorm environment ahead of the surface front is potentially unstable, the model does not trigger any convection until early morning (i.e., 1000 UTC), roughly 2 hours later than the observed. This delay appears to be attributable to the initial spin-up problem of the model, namely, like other numerical models, it is unable to generate sufficient low-level forcing comparable to the observed in order to overcome the convective inhibition created by the nighttime boundary layer. The model convection is triggered along the surface cold front as it enters Pennsylvania and New York. Furthermore, the squall line develops in the entrance region of the upper-level jet streak, where the upward branch of the secondary circulation provides a favorable forcing for the development of intense storms (Uccellini and Johnson, 1979).

Figure 4.3 compares the predicted surface fields to the observed. At 1200 UTC 14 July, i.e., 12 h into the integration, the position of the predicted surface front corresponds very well to the analyzed (cf. Figs. 4.3a and c). Both the prediction and observations show a surface low over southern Quebec which partitions the surface front into an inactive (i.e., with no convective activity) portion to the north and an active portion to the south. It is of particular interest that as the boundary layer is heated up during the morning hours, deep convection expands rapidly northeastward along the leading line while propagating slowly eastward ahead of the baroclinic zone (Fig. 4.3d). Radar imagery at Binghamton shows intense reflectivities during this period, indicating that most of the precipitation is convective. In fact, both the prediction and observations display convectively unstable conditions ahead of the surface front at 1200 UTC (e.g., CAPE ~ 2000 J kg^{-1} at Albany).

The magnitude and structure of the predicted low-level equivalent potential temperature (θ_e) and column-integrated precipitable water also compare favorably to those observed at 1200 UTC (Fig. 4.4). There is a high-θ_e tongue along and ahead of the upper-level trough axis, which extends from the southeastern states to Labrador. Accompanying the high-θ_e tongue is a south to southwesterly flow with a low-level southerly jet at 900 hPa (not shown). Such a juxtaposition clearly provides some clue as to why the squall line tends to expand rapidly northeastward once it is initiated. High precipitable water contents (> 5 cm) are also distributed along the high-θ_e tongue. Evidently, this distribution is favorable for the development of the three intense convective cells that were responsible for the later occurrence of flooding rainfall over the Montreal region (Tremblay 1994).

After the predicted squall system becomes well organized, the parameterized downdrafts in the FC scheme produce strong cooling in the lowest layers, thus forming a gust front along the leading edge of the squall line (see double dot-dashed lines in Fig. 4.3d). The position of the gust front, although it is predicted too far to the north, corresponds reasonably well to the observed (cf. Figs. 4.3b and d). The cold downdrafts also cause a mesoridge behind the gust front. Thus, the squall system produces significant pressure perturbations superposed on the larger-scale surface trough. By 0000 UTC 15 July, the convective line has passed Montreal and dropped a significant amount of precipitation in the vicinity of the city.

Figure 4.5 compares the predicted convective precipitation and upper-level liquid water content to the infrared satellite imagery during the heavy rainfall episode over the Montreal region. The basic orientation and shape of the leading convective line followed by extensive stratiform clouds to the north are reasonably reproduced. Although the RFE model predicts extensive stratiform clouds at the upper levels, a large fraction of the grid-scale precipitation evaporates before reaching the ground. Of course, due to its relatively coarse resolution, it is not possible for the RFE model to predict the small-scale cellular convection along the squall line, and in particular the three intense convective cells responsible for the Montreal flood. Nevertheless, the distribution and amount of the 24-h accumulated total rainfall is reasonably well reproduced (Fig. 4.6). The model predicts three heavy rainfall centers, i.e., near Quebec City, Montreal and Philadelphia with the amounts similar to the observed, except for the rainfall maximum near Philadelphia that is

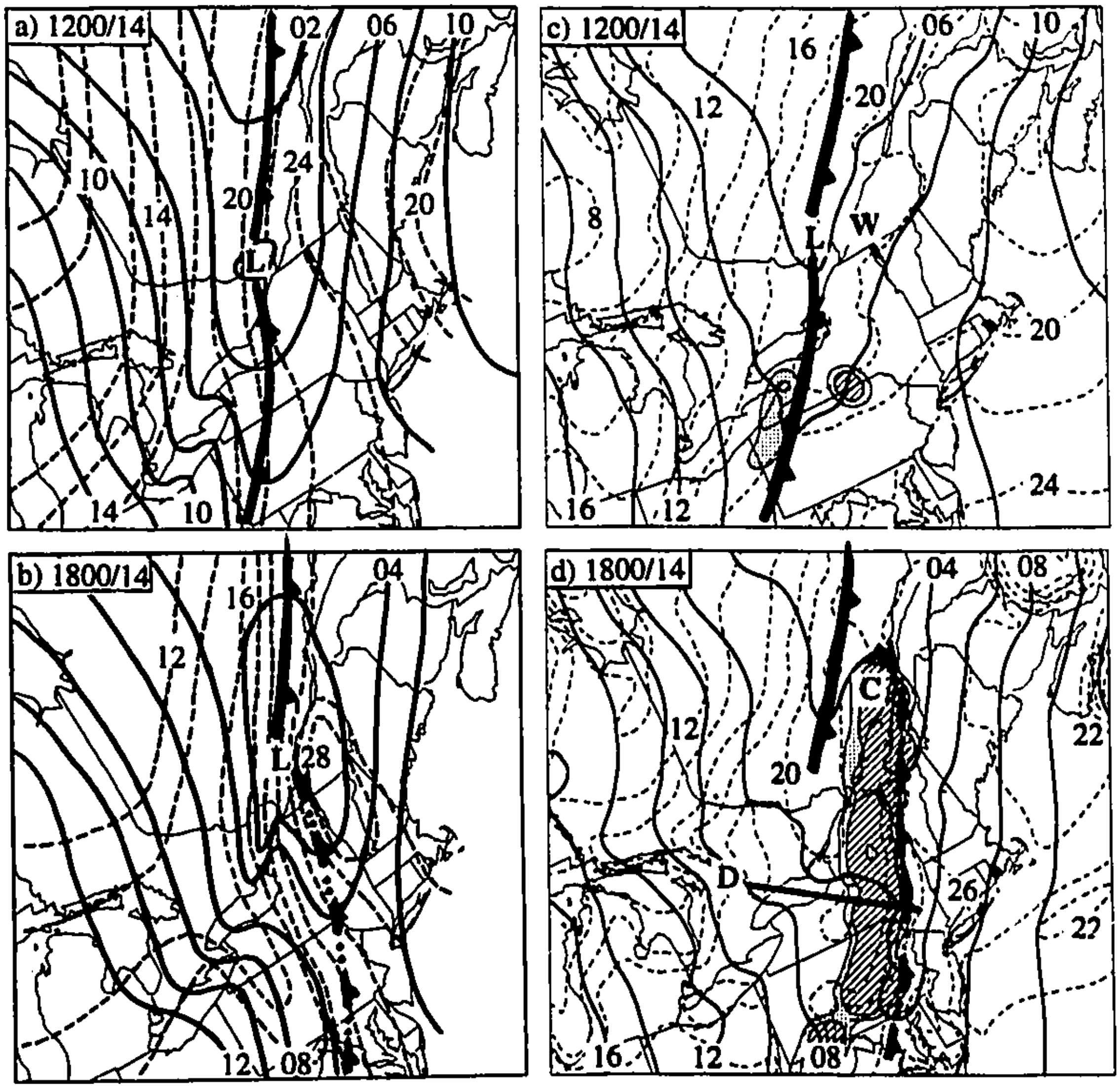

Fig. 4.3 Mesoanalysis of sea-level pressure (solid, every 2 hPa) and surface temperature (dashed, every 2 °C). The left panel shows the observations at a) 1200 UTC; and b) 1800 UTC 14 July 1987. The right panel shows the model predictions from c) 12-h; and d) 18-h integrations. Shadings represent regions of convective precipitation with rainfall rates of 1, 2 and 5 mm h^{-1}. Double dot-dashed lines denote surface cold outflow associated with the squall line. The letters, 'L', 'C' and 'W', indicate the centers of low pressure, cold and warm air, respectively.

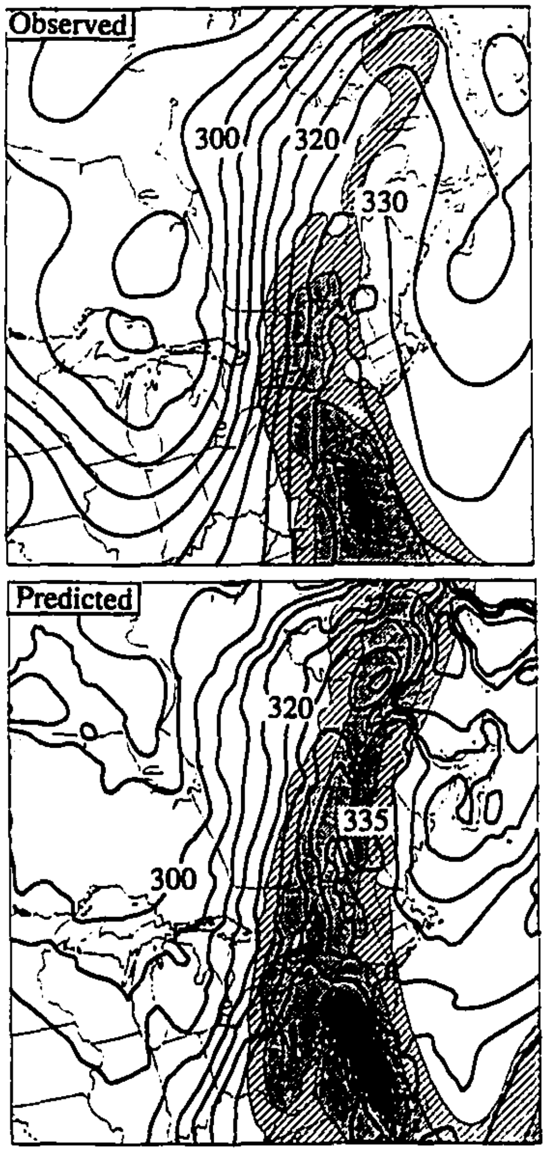

Fig. 4.4 Observed and predicted equivalent potc .tial temperature (solid, every 5 K) in the lowest model layer, superposed with tne column-integrated precipitable water content (shaded with contours of 4, 4.5, and 5 cm) valid at 1200 UTC 14 July 1987.

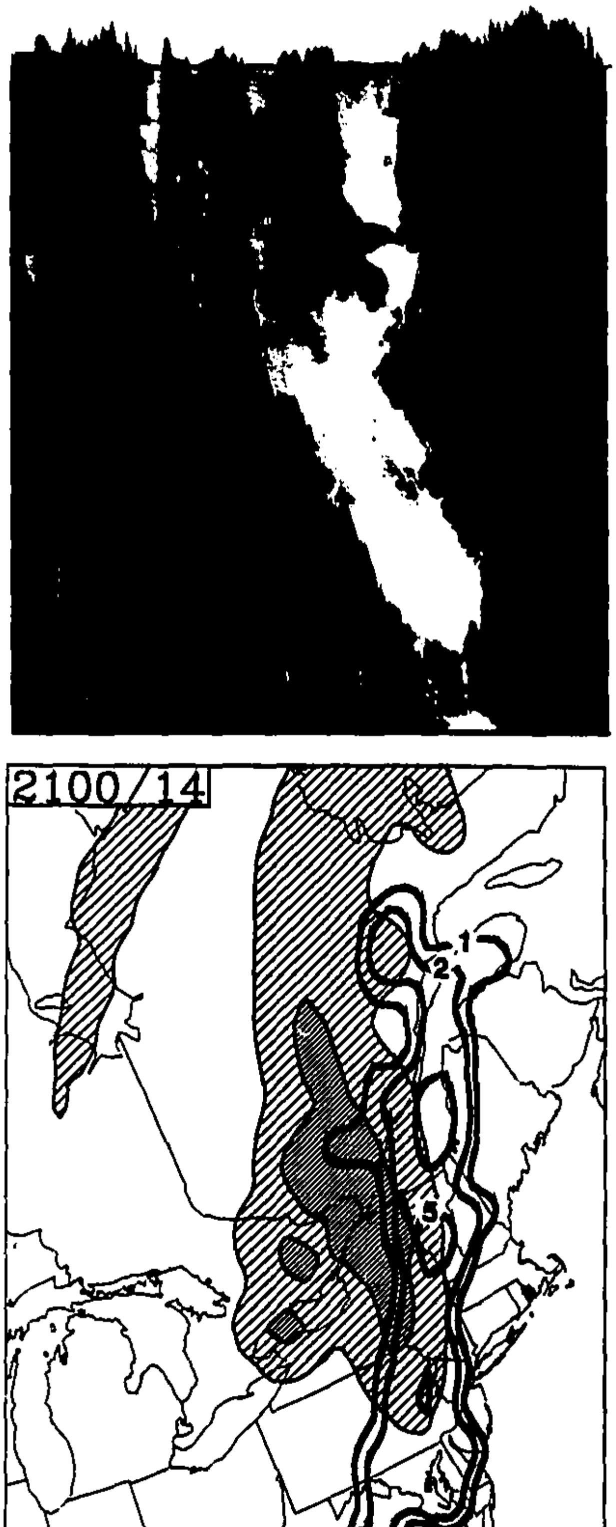

Fig. 4.5 a) The GOES infrared satellite imagery at 2100 UTC 14 July. b) The predicted convective rainfall rate (solid lines with contours of 1, 2, 5 mm h^{-1}) and 500-hPa total liquid water (shaded with contours of 0.01, 0.1 g kg^{-1}) from 21-h integration, valid at 2100 UTC 14 July.

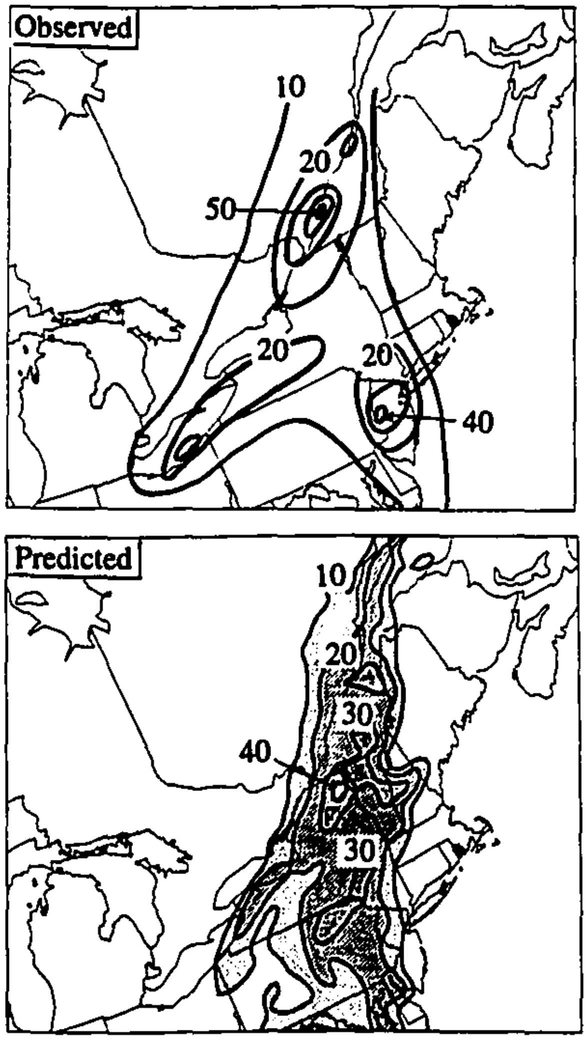

Fig. 4.6 Observed and predicted total accumulated rainfall amount (mm) between 0000 UTC 14 July and 0000 UTC 15 July 1987.

predicted too far to the west. Again, most of the precipitation at these centers is convective and is associated with the prefrontal squall line. This is consistent with observations, in which large amounts of precipitation at these locations fell in only few hours during the passage of the leading line. In this respect, the improved version of the RFE model seems to produce more realistic precipitation distributions than those in the then operational forecast and in Tremblay (1994), in which the bulk of precipitation is produced along the frontal zone behind the squall line (see his Figs. 7 and 8).

It is apparent from the results presented above that the RFE model predicts reasonably well the development and evolution of the squall line, as verified against the observations. Thus, this model prediction can be used to investigate some non-observable features, particularly the mechanisms important in the organization and evolution of the squall system.

4. Mesoscale gravity waves

Figure 4.7 shows the vertical cross section of the across-line circulation and temperature deviations from 18-h integration. There are two different types of vertical circulations associated with the squall system: one is the deep and upright motion along the leading convective line, and the other is the shallow and slantwise flow along the trailing stratiform region, denoted by 'C' and 'R', respectively. These two bands are produced, respectively, by the FC convective scheme and grid-scale condensation. As will be shown below, the convective line propagates in a gravity wave fashion at a speed much faster than the stratiform rainband.

Before discussing the role of gravity waves in the development of the prefrontal squall line, it is necessary to examine whether or not the model-produced signals agree with conceptual models of gravity waves, such as the sort given in Eom (1975). One important aspect of gravity-wave propagation is that surface pressure and wind perturbations are in phase i.e., with large positive correlations between them, but they are

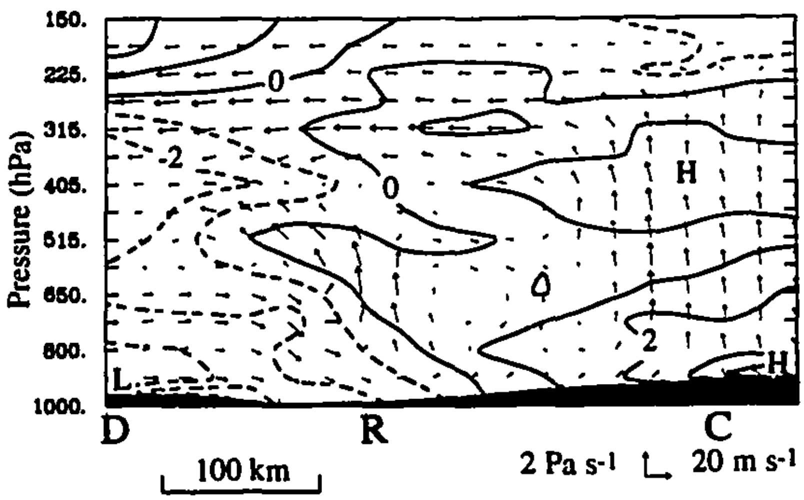

Fig. 4.7 Vertical cross section of temperature deviations (every 1 K) superposed with across-line circulation vectors, taken along line D in Fig. 4.3d, from 18-h integration. The letters, 'L' and 'H', indicate cold and warm centers, respectively; whereas 'C' and 'R' show the position of the convective and trailing stratiform precipitation bands.

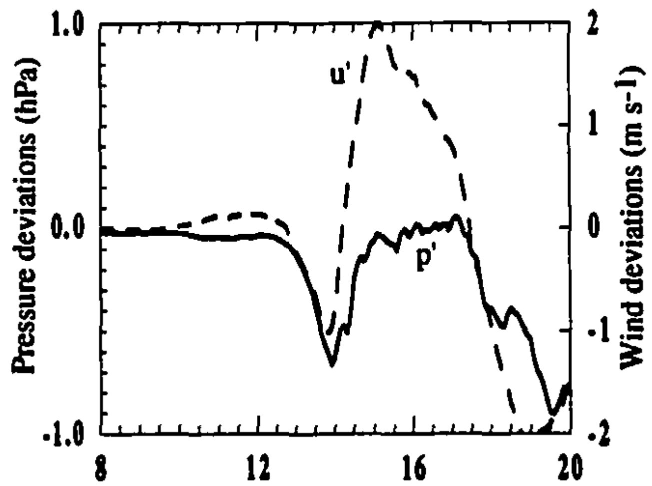

Fig. 4.8 Predicted time series of surface pressures (solid, hPa) and the horizontal wind component in the direction of wave propagation (dashed, m s^{-1}) from the control run. The surface winds and pressures from Exp. DRY have been deducted.

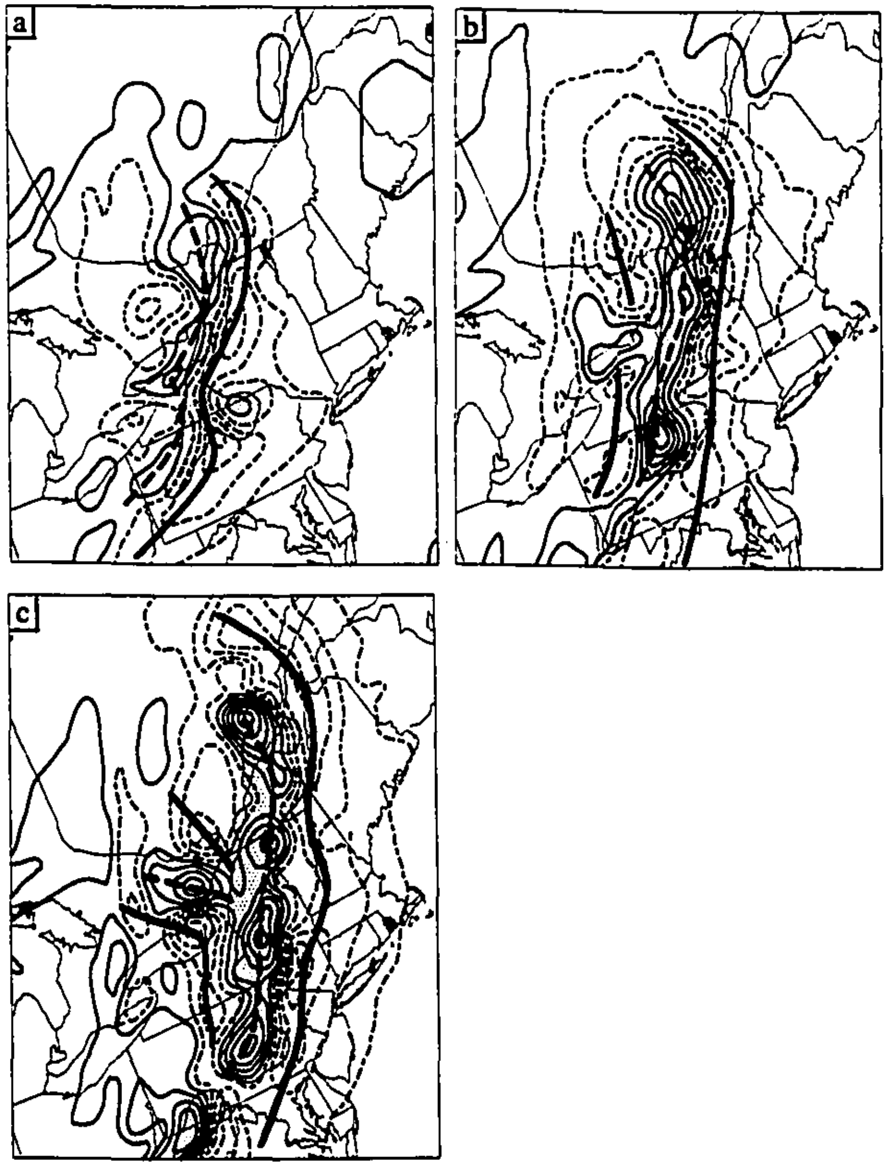

Fig. 4.9 Predicted surface pressure tendencies (solid/positives, dashed/negatives) at intervals of 0.25 hPa (2 h)$^{-1}$ between a) 12- and 14-h; b) 14- and 16-h; and c) 16- and 18-h integrations. Surface pressures from Exp. DRY have been deducted. Thick solid (dashed) lines indicate the axis of the tendency troughs (ridges). Shadings indicate regions with convective rainfall rates greater than 2 mm h^{-1} from a) 14-h; b) 16-h; and c) 18-h integrations.

90° out of phase with vertical motion. Thus, as with other studies (e.g., Bosart and Cussen, 1973; Bosart and Sanders, 1986; Koch and Golus, 1988), the correlation between the surface pressure and wind perturbations at Montreal is calculated and given in Fig. 4.8. In this figure, the large-scale influence on both the pressure and wind traces has been removed by subtracting their counterparts from a DRY run, in which all diabatic heating from implicit and explicit clouds is turned off. It can be noted that the model-produced oscillations of pressures and winds have amplitudes of 0.5 hPa and 2 m s^{-1}, respectively. Furthermore, the two signals are in phase, with a correlation coefficient of +0.76, which is comparable to that obtained by Koch and Golus (1988) in their observational study of gravity waves. Such a high correlation also can be found for all the stations given in Fig. 4.1.

To gain insight into the propagation of the gravity waves, Fig. 4.9 shows the distribution of the model-generated two-hourly surface pressure tendencies; again, the pressure variations from the DRY run have been subtracted. The propagation of the organized pressure tendency trough at the leading edge, followed by couplets of tendency ridges and troughs, is apparent. Surface pressure falls of around 1 hPa every two hours can be seen between 12 and 18 hours, with the amplitudes increasing as the waves propagate away from the initial convective region. It is evident that these waves propagate outward along two tracks: one toward the east and the other toward the northeast. The northeastwardly propagating wave is much faster than its eastward counterpart; their average speeds are 35 and 20 m s^{-1}, respectively. These propagation characteristics are similar to those in Tremblay (1994) (see his Fig. 10), except for the eastward phase speed which is much faster in his simulation.

Even though the above results are consistent with the conceptual model of gravity waves, one may argue that the pressure perturbations shown in Figs. 4.8 and 4.9 could be caused simply by the convective system. For example, it is well known that pressure falls often occur ahead of a squall line due to compensating subsidence (see Hoxit et al., 1976;

Johnson and Hamilton, 1988), whereas pressure rises are found along the convective line due to evaporative cooling, producing perturbations similar to those in Figs. 4.8 and 4.9. However, this argument could not explain the multiple pressure oscillations behind the leading convective line, e.g., at 18-h, since convection does not occur over this area (due to the absence of CAPE). Before demonstrating that these perturbations can be attributed to the propagation of gravity waves, we need to determine the source of the waves.

Geostrophic adjustment, shearing instability and deep convection are the three major mechanisms used in the previous studies to explain the generation of mesoscale gravity waves. According to geostrophic adjustment theory, for a disturbance smaller than the Rossby radius of deformation, the mass field tends to adjust to the wind field, thereby generating gravity-inertia waves propagating away from the disturbance. Van Tuyl and Young (1982) found that gravity-inertia waves are initiated in regions of strong divergence and large Rossby number near the jet-stream cores. Such conditions are typically found at the exit of a propagating jet streak approaching a downstream ridge. This finding has been confirmed by Uccellini and Koch (1987) in a review of 13 gravity-waves studies. However, in the present case, gravity waves are initiated in the entrance rather than the exit region of an upper-level jet streak.

On the other hand, the presence of the upper-level jet suggests that the gravity waves may owe their existence to shearing instability that extracts energy from the vertical wind shear in the presence of a critical level (Gossard and Hooke, 1975). From linear stability analysis, a critical level and a small Richardson number are the necessary conditions for the initiation of gravity waves (Lalas and Einaudi, 1976; Stobie et al., 1983). In their analysis, Uccellini and Koch (1987) speculated that shearing instability may have also played an important role in a majority of the gravity wave cases they reviewed. More recently, Koch and Dorian (1988) and Bosart and Seimon (1988) also suggested that this mechanism was responsible for the generation of the gravity waves in the cases they studied.

In order to examine if the above two mechanisms are operative in the present case, the results from Exp. DRY are analyzed. If geostrophic adjustment and/or shearing instability are operative, the model should produce gravity waves in the absence of convection. As compared to the control prediction, the barographs from this experiment display little sign of significant oscillations (not shown). Therefore, we may conclude that the predicted mesoscale oscillations are *not* due to either geostrophic adjustment or shearing instability. Furthermore, the results rule out the possibility that any imbalances between the wind and mass fields at the model initial time would be responsible for the generation of the gravity waves shown above.

Thus, deep convection may account for the generation of gravity waves in the present case. To support this argument, an additional experiment is conducted, in which the first 12-h integration is identical to the control run, but the tendencies of subsequent diabatic heating due to parameterized convection and grid-scale clouds are forced to diminish to zero between the 12- and 14-h integrations (Exp. NCON). The 2-h period is used here to avoid possible "shocks" induced by too abrupt changes in the convective forcing. As expected, a pulse is generated near Lake Erie by the parameterized convection, and propagates away from this source point. The pressure traces at different stations along two different tracks are given in Fig. 4.10, which shows that the gravity waves are initiated by convection near Buffalo (BUF) and then they "radiate" away from the source region. Obviously, these waves propagate over a long distance in the same manner as in the control run, including the phase speed and wave period. However, the wave amplitude decreases rapidly downstream. Such a decrease in wave amplitude is typical of free waves propagating in three dimensions.

To verify further that these signals are indeed gravity waves, a vertical cross section of divergence, vertical motion, and potential temperature along the northeastward track is shown in Fig. 4.11. A wavelike oscillation is evident from the θ=305 K surface, with a negative (positive) surface pressure perturbation below the trough (ridge), where the low-level air is warmer (colder). Such wave structures are not detectable from the θ=330 K surface, indicating that the wave activity is constrained to the low levels. The wave signal is characterized by convergence above divergence ahead of the axis of the surface pressure tendency trough, followed by an opposite circulation and convergence/divergence pattern behind this axis. Downward and upward motions are found, respectively, ahead and behind the leading wave trough. This relationship between the flow structure and surface pressure perturbations agrees well with the conceptual model of gravity waves by Eom (1975). Furthermore, these perturbations are not due to the propagation of convection, since it has been terminated a few hours earlier. Therefore, the results suggest that a) the convective forcing is responsible for the generation and later enhancement of gravity waves, and b) the waves can propagate over a long distance without further convective enhancement.

Although their amplitudes decrease along both tracks A and B (see Fig. 4.10), the gravity waves in the present case can propagate over a relatively long distance; thus, the environmental conditions must be, at least to a certain degree, favorable for their horizontal propagation. As reviewed in section 1, a wave duct must be present in order for gravity waves to propagate for several hours without being dissipated through vertical energy dispersion. It is evident from Fig. 4.12a that the wave environment, averaged along tacks A and B, is characterized by a low-level statically stable layer (i.e., with larger N) underneath a less stable layer, indicating that the first condition for wave duct is met (Lindzen and Tung, 1976). However, the stable layer is shallow (i.e., 100 hPa), and it weakens rapidly when a well-mixed boundary layer develops (after about 16 h into the integration). Moreover, it is evident that the waves move faster than the environmental winds at ail levels (see Fig. 4.12b), namely, a critical level does not exist for both propagation tracks. This absence of a critical level confirms the above conclusion that shearing instability mechanisms could not be responsible for the generation of the waves in the present case. This situation is similar to the cases studied by Uccellini (1975) and

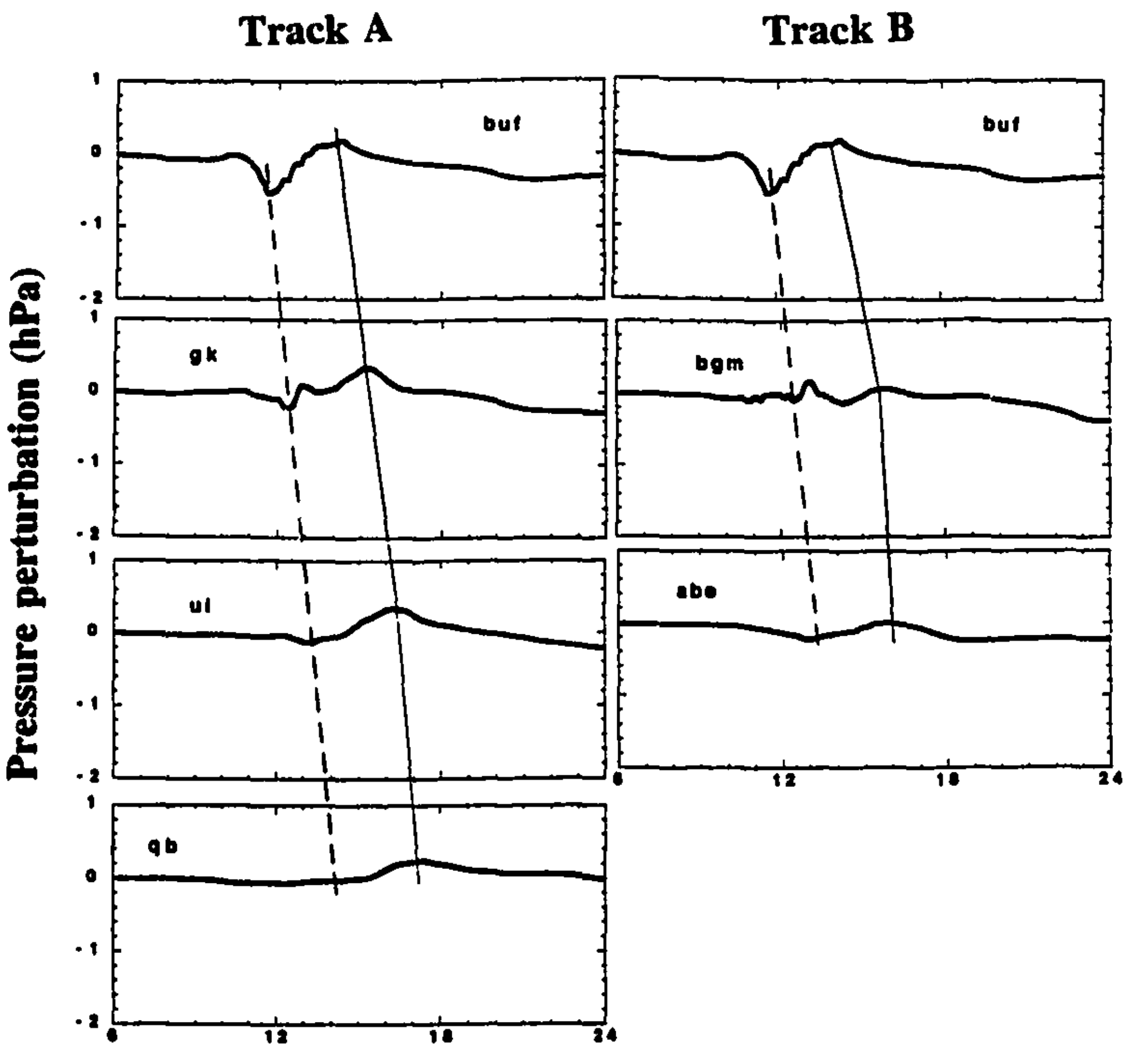

Fig. 4.10 Predicted barographs of surface pressures (hPa) from Exp. NCON (no convection after 14 h). Surface pressures from Exp. DRY have been deducted. Thin solid (dashed) lines indicate the position of the leading wave ridges (troughs). See Fig. 4.1 for the locations of the stations and the tracks.

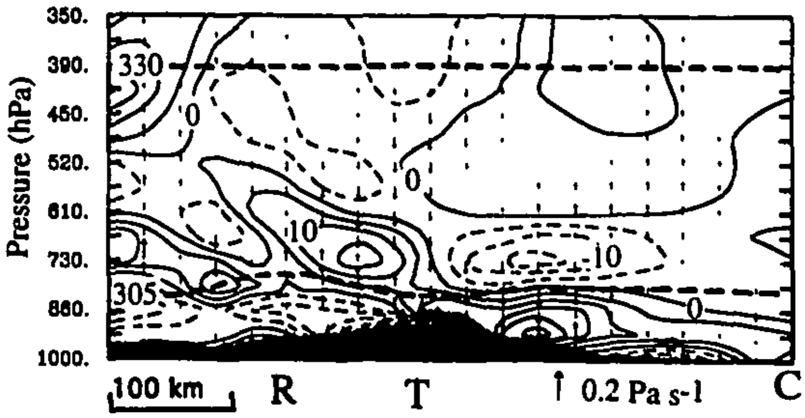

Fig. 4.11 Vertical cross section of divergence (solid/positive, dashed/negatives) at intervals of 5×10^{-6} s^{-1}, superposed with vertical motion perturbations, taken along line 'C' in Fig. 4.1, from 18-h integration of Exp. NCON. The predicted potential temperature surfaces θ = 305 and 330 K are represented by thick dashed lines. The letters, 'T' and 'R', indicate the location of the wave trough and ridge, respectively.

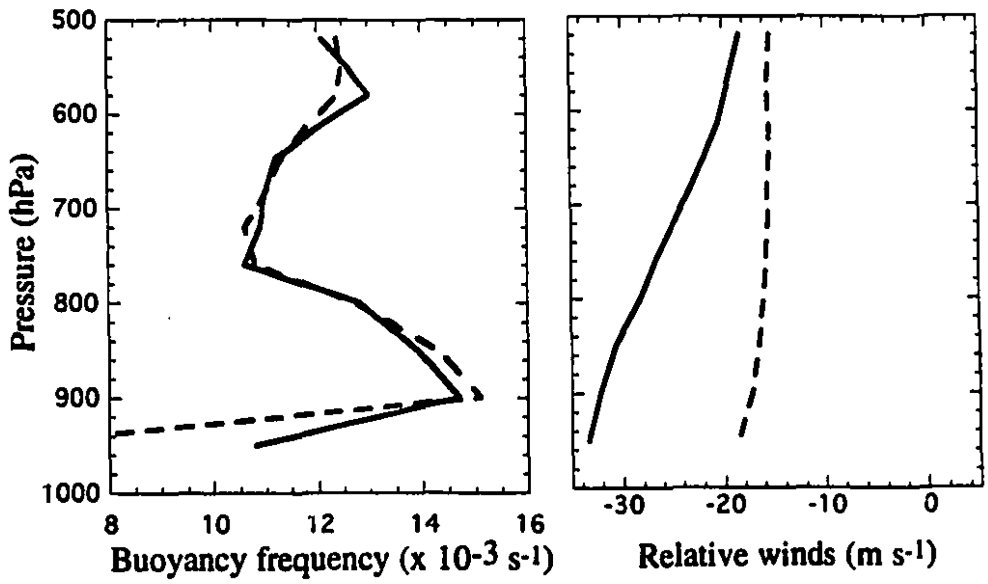

Fig. 4.12 Vertical profiles of a) the Brunt-Väisällä frequency ($N = [(g/\theta)(d\theta/dz)]^{1/2}$), and b) horizontal winds relative to the wave phase speed averaged along the tracks A (solid) and B (dashed) from 15-h integration of Exp. NCON. The relative flows are obtained by deducting the wave phase speeds of 35 m s^{-1} for track A and 20 m s^{-1} for track B.

Einaudi et al. (1987), in which the waves propagate over a long distance without critical levels. Thus, the wave environment exhibits a wave duct condition that, though not perfect, helps sustain the waves for a certain distance by preventing their total dissipation.

5. Wave-convection interaction

Numerous studies have shown that gravity waves and convection can interact constructively when they propagate together in a "phase locked" manner (Stobie et al., 1983; Koch et al., 1988; Zhang and Fritsch, 1988a; Cram et al., 1992a; Powers and Reed, 1993). Such an interactive process is the basis of the wave-CISK model. Since their early development (Raymond, 1975; 1976), wave-CISK models have been afflicted with a number of problems. The most important one was associated with the scale selection. Almost all of the earlier wave-CISK models predict that the gravity wave becomes more unstable as the wavenumber increases. This problem has been attributed to the use of the "quasi-equilibrium" assumption (Xu and Clark, 1984) in which the convective lifetime is negligible compared to the time scale governing changes in the larger-scale environment. This problem was later alleviated by introducing a time lag between the larger-scale forcing and the triggering of convection (Davies, 1979; Xu and Clark, 1984). However, comparisons with observations are not all satisfactory because even the latest versions of wave-CISK models are still not sufficiently realistic (see the related discussion in Koch et al., 1988). Thus, we can only evaluate qualitatively if the wave-CISK mechanism would be operative in the present case.

One way to determine if the wave-CISK mechanism is operating is to examine the phase relationship between the convective line and the leading wave oscillation. For this purpose, the pressure tendencies given in Fig. 4.9 are examined again. Note that the convective line at earlier stages is distributed midway between the leading pressure tendency trough and ridge (see Fig. 4.9a). At later stages, however, the leading convective line is mainly situated along the wave-ridge axis (see Figs. 4.9b,c). This evolution and phase relationship are in agreement with observations (e.g., Eom, 1975; Uccellini, 1975; Miller and Sanders, 1980) and the conceptual model of gravity waves. In particular, the wave-induced vertical motion structures are 90° out of phase from both the pressure and horizontal wind perturbations, with the strongest upward motion occurring between the trough and ridge of the wave. Since convection is triggered in regions where lifting lasts the longest, it should occur at or ahead of the wave ridge.

This phase-locking between convection and the gravity waves is also evident from Fig. 4.13, which shows the surface pressure traces superposed with convective precipitation rates from a few selected points along tracks A and B. In general, convective precipitation commences shortly after the passage of the first wave trough, with most precipitation occurring over the wave ridge (also see Fig. 4.9). Obviously, the wave-induced upward motion behind the trough axis assists the initiation of the parameterized convection. Once the FC convective scheme is activated, the parameterized moist downdrafts produce a cold pool superposed on the wave ridge. This tends to increase across-line pressure gradients and enhance low-level convergence such that more convection could develop behind the trough axis. Such a positive feedback process fits well the concept of wave-CISK models. Furthermore, these results are in good agreement with the previous observational studies of wave-convection interaction (e.g., Uccellini, 1975; Miller and Sanders, 1980; Stobie et al., 1983; Koch et al., 1988).

A comparison between the control and NCON runs reveals that deep convection can modify substantially the structure and other properties of gravity waves. For example, the continued convective forcing excites a train of oscillations with relatively larger amplitudes as the system propagates downstream, whereas there is only a single major gravity wave event in Exp. NCON (cf. Figs. 4.10 and 4.13). Because the convectively generated cold pool is a stable structure, continued low-level convergence could persist for a long period over the wave ridge. This leads to the widening of the wave ridge as the waves propagate (see Fig. 4.13). Moreover, the convergence/divergence couplet along the

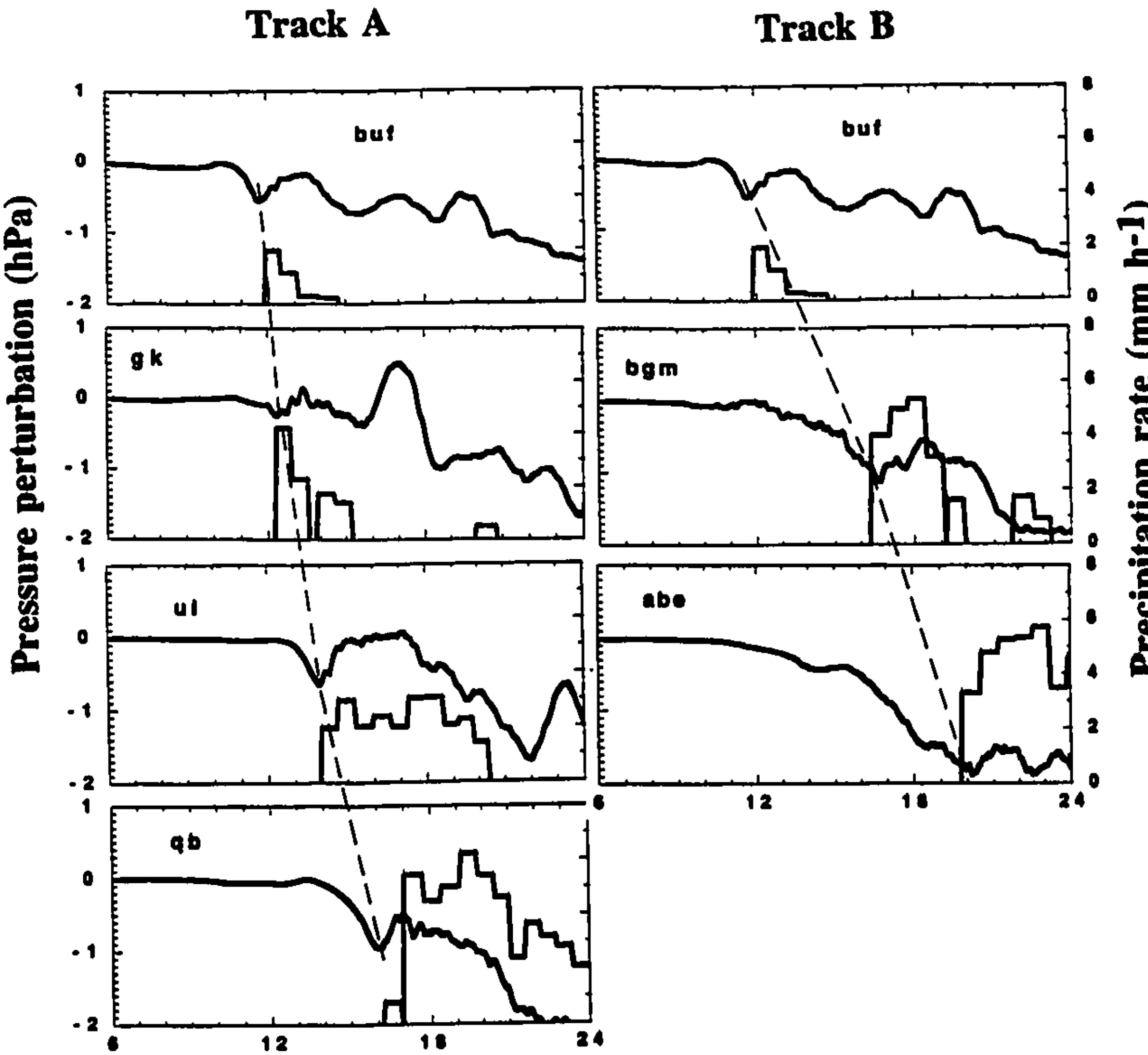

Fig. 4.13 As in Fig. 4.10 but from the control run. The time series of rainfall rates (mm h^{-1}) are superposed.

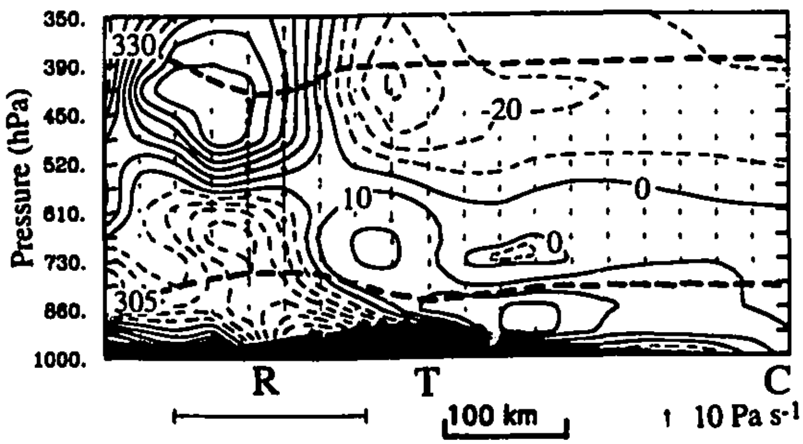

Fig. 4.14 As in Fig. 4.11 but from the control run, with contour intervals of 10 x 10^{-6} s^{-1}. The bracket horizontal line at the bottom indicates the position of convective activity.

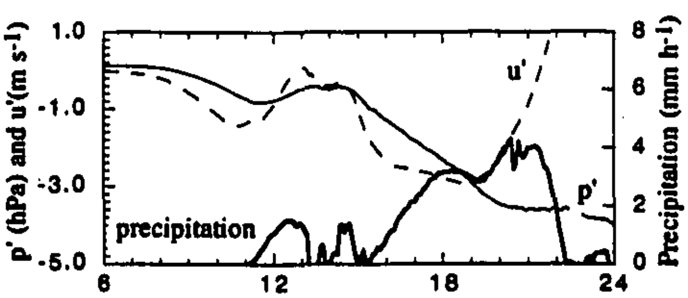

Fig. 4.15 As in Fig. 4.8 but for Exp. KUO. The temporal series of rainfall rates (heavy solid lines, mm h^{-1}) are superposed. The units for surface pressure and wind perturbations are given on the left ordinate, and the unit for the rainfall rates is shown on the right ordinate.

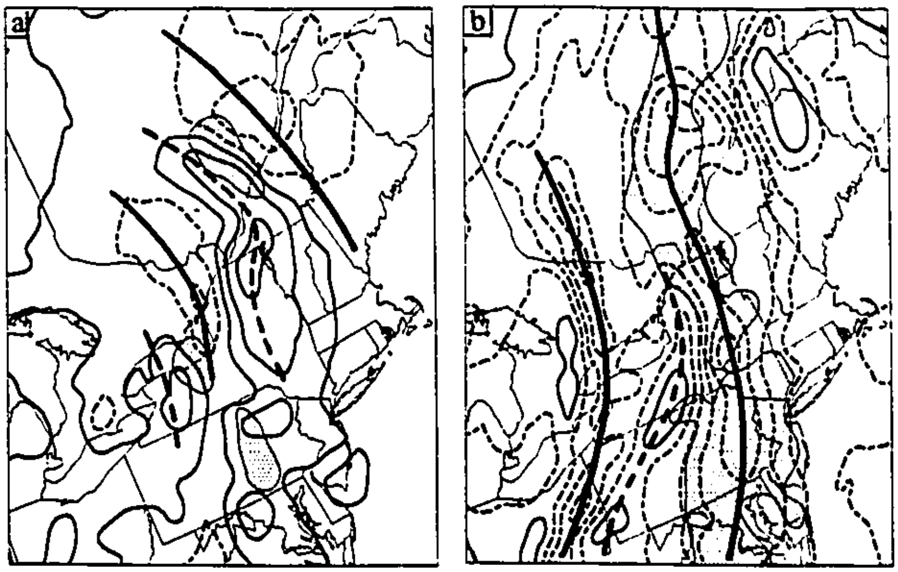

Fig. 4.16 As in Fig. 4.9 but from a) 12- to 14-h; and b) 16- and 18-h integrations of Exp. KUO.

Fig. 4.17 As in Fig. 4.9c but for Exp. NOPD (no parameterized moist downdrafts).

wave ridge is deeper than that in Exp. NCON, and wavelike oscillations of θ surfaces are found even at higher levels (see Fig. 4.14). The convectively forced upward motion near the ridge axis is as strong as 1 m s^{-1}. Thus, the results indicate that gravity waves could locally lose their structure in the presence of intense and organized convection, as also noted by Koch et al. (1988).

When examined together, the vertical cross sections in Figs. 4.11 and 4.14 are useful to describe the interaction between the parameterized convection and the gravity waves in the present case. As shown in Fig. 4.11, the vertical structure of a gravity wave is characterized by convergence below and divergence aloft, with the maximum rising motion occurring midway between the trough and advancing ridge (Eom, 1975; Uccellini, 1975; Cram et al., 1992a). This vertical circulation tends to produce a lower-θ_e dome (ridge) and higher-θ_e dip (trough). When deep convection is included, the intensification of the waves depends on the location of the convective heating and cooling. In the present case, the parameterized convection occurs mainly over the wave ridge (see Fig. 4.14), and it stabilizes the atmospheric column by warming the upper levels and cooling the low levels. Since this diabatic heating (cooling) coincides with wave-induced warm (cold) perturbations, the gravity wave intensifies as long as the convection could interact constructively with the wave.

It should be noted that the realistic simulation of the wave-CISK mechanism depends on the type of convective parameterization. For example, we have performed a sensitivity experiment, in which everything is kept the same as in the control run except that the FC scheme was replaced by the Kuo (1974; see Mailhot et al., 1989) scheme (Exp. KUO). This scheme has been used operationally in many meteorological centers, including CMC. It is evident from Fig. 4.15 that gravity waves can also be generated with the Kuo scheme. However, the correlation between the pressure and wind perturbations is much less than that in the control run (cf. Figs. 4.8 and 4.15). Furthermore, although the Kuo scheme begins to produce precipitation after the passage of the first wave-trough (i.e., at 12-h), this rainfall rate is weak and most of the precipitation occurs long after the passage of the wave (i.e., after 16-h integration), in conjunction with a slow and continuous pressure drop associated with the large-scale frontal trough (see Fig. 4.2). Thus, the bulk of the precipitation produced at Montreal by the Kuo scheme is not forced by gravity waves, but by large-scale convergence, as also occurred in the then operational forecast as well as in the simulation of Tremblay (1994).

The phase relationship between the waves and convective precipitation, as generated by the Kuo scheme, can be further seen from Fig. 4.16. In the early stages (Fig. 4.16a), convection only covers a small area and occurs midway between the wave troughs and ridges. However, the subsequent evolution of the wave-convection system departs significantly from that in the control run. Specifically, the Kuo scheme produces a wider convective band with heavier rainfall rates associated with the squall line (cf. Figs. 4.9c and 4.16b). Of particular significance is that the convective band coincides with the pressure tendency trough rather than the wave ridge. Moreover, the model produces surface pressure falls almost everywhere in the vicinity of the MCS, with fewer pressure oscillations after the passage of the system. Since the vertical motion (based on precipitation) and horizontal flow from this run are almost 180° out of phase with the pressure variations during the later stages, the generation of these perturbations could not be explained by wave-CISK models.

Clearly, the above-mentioned differences can be attributed to the different ways to handle subgrid-scale convection between the FC and Kuo schemes. In general, the heating profiles produced by the FC scheme are maximized at a level much higher than that produced by the Kuo scheme. Bélair et al. (1994) showed that the Kuo scheme mainly warms the midtroposphere, as compared to the FC scheme which tends to warm upper levels and cool lower levels (see their Fig. 10). The midlevel warming would enhance the lower-level mass and moisture convergence, and thus favors the development of a pressure trough or mesolow at the surface. In addition, the lack of moist downdrafts in the Kuo scheme could explain the failure in producing the multiple trough-ridge pressure perturbations, since the convectively generated mesohigh (or ridge) is caused the accumulation of cold air in the boundary layer.

To evaluate the effects of the parameterized moist downdrafts on the generation of gravity waves and to facilitate the comparison between the FC and Kuo schemes, an additional experiment is conducted in which the downdraft effects in the FC scheme are turned off (Exp. NOPD). Very interestingly, without the parameterized downdrafts, the model still produces numerous oscillations along track A, and the wave-squall system also propagates at a speed similar to that in the control run (cf. Figs. 4.9c and 4.17). Furthermore, convective precipitation occurs behind the pressure trough, as it does in the control run. However, the removal of the parameterized downdrafts results in much weaker wave ridges along the squall line. Therefore, the results suggest that the parameterized moist downdrafts are instrumental in determining the amplitude and structures of the gravity waves, but they have little impact on the displacement of the squall-wave system since it is more determined by propagating gravity waves. The results conform to the finding of Raymond (1987), who also emphasized the importance of low-level cooling in the wave-CISK mechanism. It is also consistent with the modeling study of Cram et al. (1992a), who noted that the phase speed of the wave-squall system is less sensitive to the incorporation of parameterized downdrafts.

6. Conclusions

In this study, an improved mesoscale version of the RFE model has been used to investigate the role of gravity waves in the development of a prefrontal squall line associated with the 14 July 1987 Montreal flood. Several numerical experiments have been conducted to gain insight into the influence of deep convection on the propagation and characteristics of the gravity waves. The most important results are summarized below.

a) It is shown that the improved version of the RFE model could reproduce reasonably well the development and structure of the 14 July 1987 squall line, as verified against available observations. In particular, the predicted squall line is initiated at nearly the right location and moves at the right speeds eastward ahead of a frontal zone. The distribution and magnitude of the associated precipitation also compare favorably with the observed.

b) It is found through various diagnostics and sensitivity experiments that deep convection interacts closely with gravity waves in the development of the squall line and heavy rainfall events. These waves are excited by early convection near Lake Erie and propagate for many hours in an environment characterized by a low-level thermal inversion.

c) The wave-CISK mechanism accounts for the maintenance and intensification of the wave-convection system. Specifically, deep convection and the leading gravity wave propagate in a "phase-locked" manner over a long distance. Hence, the continued convective heating/cooling tends to enhance the gravity waves, while the gravity waves assist the organization of deep convection into a line structure. As deep convection intensifies, the gravity waves tend to lose locally their structures such that the layer of convergence and divergence becomes deeper and their wave ridge becomes wider.

d) It is found that the realistic prediction of the wave-convection interaction depends on the use of an appropriate convective parameterization. In particular, the Kuo convective scheme tends to trigger moist convection over the mesotrough (or mesolow) region during the mature stage, owing partly to its heating maximum occurring in the midlevels and partly to the lack of parameterized moist downdrafts. Thus, the Kuo scheme fails to amplify a train of gravity waves interacting with deep convection.

e) As shown in the present and previous studies, parameterized downdrafts could play important roles in the generation of surface pressure perturbations and outflow boundaries, as well as in the propagation of gravity waves. Thus, the detailed structure and evolution of these surface variables could be available to local forecasters if parameterized downdrafts and explicit moisture effects can be incorporated into operational numerical weather prediction models.

Although the above conclusions are obtained from only a single case study, the results presented above show the potential significance of predicting reasonably the generation and propagation of gravity waves in order to forecast the development of mesoscale convective systems and their associated quantitative precipitation. In particular, this study points to one of the major difficulties in predicting realistically the interactions between gravity waves and deep convection, i.e., it depends on the type of convective parameterization. To avoid this problem, one has to use high-resolution nonhydrostatic models to examine the roles of gravity waves in the development of mesoscale convective systems.

Chapter 5

The 14 July 1987 intense convective system. Part II: A trailing stratiform rainband

5.1 Presentation of article 3

As shown in the preceding chapter, a second band of organized updrafts is found at the rear of the 14 July 1987 squall system (see Fig. 4.7), in association with a trailing stratiform rainband. Although such trailing rainbands are often observed (e.g., Smull and Houze 1985, 1987; Johnson and Hamilton 1988; Rutledge et al. 1988), the flow structures associated with this squall system differ significantly from those observed in classical squall lines (see Fig. 1.2). The processes leading to the development of such structures are the subject of the present chapter. In article 3, the different dynamical instabilities that could be responsible for the slantwise upward motion at the rear of the squall system are examined, as well as the respective roles of the implicit and explicit condensation processes in the generation of the leading and trailing updrafts bands. The evolution of the vorticity structures associated with these flow structures are also studied.

5.2 Article 3

Numerical prediction of an intense convective system associated with the July 1987 Montreal flood. Part II: A trailing stratiform rainband. By Stéphane Bélair, Da-Lin Zhang, and Jocelyn Mailhot.

Accepted for publication in *Atmos.-Ocean*, December 1994.

Abstract

In this study, the internal circulation structures of the 14 July 1987 intense mesoscale convective system (MCS) are investigated using an improved high-resolution version of the Canadian regional finite-element model. It is found that although the MCS is characterized by a leading convective line followed by a trailing stratiform rainband, the associated circulation structures differ substantially from those in the classical midlatitude squall system. These include the rapid propagation and separation of the leading convection from the trailing rainband, the development of a surface-based instead of an elevated rear-to-front descending flow and a shallow front-to-rear ascending flow associated with the stratiform precipitation, the generation of low- to mid-level rather than mid- to upper-level stratiform cloudiness and the development of a strong anticyclonic vorticity band at the back edge of the stratiform region.

It is shown that the trailing stratiform rainband is dynamically forced by frontogenetical processes, and aided by the release of conditional symmetric instability and local orographical lifting. The intense leading and trailing circulations result from latent heat released by the convective and explicit cloud schemes, respectively. Sensitivity experiments reveal that the proper coupling of these two cloud schemes is instrumental in obtaining a realistic prediction of the above-mentioned various mesoscale components. Vorticity budget calculations show that tilting of horizontal vorticity contributes the most to the amplification of the anticyclonic vorticity band, particularly during the squall's incipient stage. The sensitivity of the simulated squall system to other model physical parameters is also examined.

1. Introduction

There have been considerable observational studies of mesoscale banded cloudiness and precipitation associated with extratropical cyclones (e.g., Browning and Harrold, 1969; Hobbs, 1978; Houze and Hobbs, 1982; Sanders and Bosart, 1985; Reuter and Yau, 1990; Snook, 1992) and mesoscale convective systems (MCSs) or squall lines (Ogura and Liou, 1980; Smull and Houze, 1985; Leary and Rappaport, 1987; Johnson and Hamilton, 1988; Rutledge et al., 1988; Houze et al., 1989). In particular, much progress has been made during the past two decades on the understanding of frontal rainbands. Conditional symmetric instability (CSI) has been commonly suggested as one of the dynamical mechanisms by which these rainbands are generated (Bennetts and Hoskins, 1979; Emanuel, 1979; Sun, 1984; Xu, 1986; Thorpe and Rotunno, 1989).

In contrast, much less attention has been paid to the understanding of the banded stratiform precipitation that often occurs behind a line of deep convection (i.e., squall line). Like frontal rainbands, this type of banded precipitation develops in convectively stable conditions and typically has a width of a few tens to a couple of hundreds of kilometers. However, it has been found that in some cases, the trailing stratiform precipitation can account for as much as 40% of the total rainfall of some MCSs (Houze, 1977; Churchill and Houze, 1984), and produce upward motion as strong as 1 m s^{-1} (Ogura and Liou, 1980; Rutledge et al., 1988). Because of the generation of significant precipitation, latent heating in the trailing stratiform region tends to have more dominant effects on the structure and evolution of mesoscale circulations than those associated with frontal rainbands. In fact, it has been observed that intense trailing stratiform precipitation is well correlated to the development of midlevel cyclonic (Leary and Rappaport, 1987; Zhang and Fritsch, 1987; 1988b; Brandes, 1990; Biggerstaff and Houze, 1991b; Zhang, 1992) and anticyclonic mesovortices (Biggerstaff and Houze, 1991b; Zhang, 1992), strong sloping front-to-rear (FTR) and rear-to-front (RTF) flows (Smull and Houze, 1987; Houze et al., 1989; Zhang and Gao, 1989), surface wake lows (Johnson and Hamilton, 1988; Zhang et al., 1989), and heat bursts (Johnson et al., 1989).

Although squall-line systems have been extensively investigated for many years, only a few case studies focused on the processes leading to the formation of trailing stratiform precipitation. Smull and Houze (1985) examined the water budget of a midlatitude squall line and found that most of the trailing stratiform precipitation is produced by the fallout of the rearwardly advected ice particles from the leading convective line. Based on composite high-resolution dual-Doppler radar analyses of the 10-11 June 1985 squall system, Biggerstaff and Houze (1991a) noted that the region of heavier stratiform precipitation tends to be located immediately behind the more intense convective portions of the leading line, and that the width of the stratiform precipitation is determined by a combination of the FTR wind velocity and microphysical fallout scales. Using a numerical simulation of the same case, Zhang and Cho (1992) investigated the dynamical mechanisms whereby the banded stratiform precipitation develops. They found a deep layer of negative moist potential vorticity (MPV) in the upper portion of the FTR ascending flow, indicating that the stratiform region is unstable to slantwise convection. Zhang and Cho (1992) showed that the negative MPV in this region results from upward and rearward transport of low-level convectively unstable air along the sloping FTR ascending flow after the associated potential instability is relieved in the leading convective region.

In these previous studies, both the leading convective line and trailing stratiform precipitation are quite intense, so convective processes along the leading line appear to have played an important role in determining the intensity, structure and width of stratiform precipitation. However, there are significant case-to-case variabilities in the development of stratiform precipitation. In fact, for some squall systems, much less or little trailing stratiform precipitation has been observed (e.g., Carbone et al., 1990; Trier et al., 1991; Fankhauser et al., 1992). Therefore, several questions can be raised. For example, what dynamical processes could be responsible for such variabilities? What is the relative importance of the leading convection vs. the prestorm environments in the development of trailing stratiform precipitation?

The main purpose of the present study is to address the above issues, using a 20-h numerical prediction of an intense squall system that caused the flooding rainfall in the vicinity of Montreal on 14 July 1987 (see Bellon et al., 1993; Tremblay, 1994; Bélair et al., 1995b). In Part I of this series of papers (see Bélair et al., 1995b), we have shown that an improved mesoscale version of the regional finite-element (RFE) model reproduces reasonably well the development and evolution of the squall system associated with the Montreal flood events, as verified against available observations. The model also reproduces a line of squall convection, followed by a band of stratiform precipitation, as occurred in other squall systems (e.g., Ogura and Liou, 1980; Johnson and Hamilton, 1988). However, the flow structure and development mechanisms of the squall system appear to differ from those in the previous squall-line studies. In this paper, we will focus only on the development of the trailing stratiform rainband, since the generation of the leading squall line has been the subject of Part I of this series of papers. Another purpose of this study is to examine the processes leading to the development and maintenance of an intense anticyclonic vorticity band in the trailing stratiform region.

The next section shows evidence of the model-predicted precipitation band, as compared to satellite observations. Section 3 presents the development of midlevel cyclonic and anticyclonic vorticity structures associated with the stratiform rainband. Section 4 examines various dynamical forcing mechanisms that are responsible for the generation of the trailing stratiform rainband, whereas section 5 discusses the roles of different model physical processes in the development of the trailing stratiform precipitation. A summary and concluding remarks are given in the final section.

2. Precipitation band

The satellite infrared imagery at 1800 UTC 14 July, given in Fig. 5.1a, shows a convective line (denoted by the letter, 'C') followed by a transition zone of low-level clouds and a band of midlevel cloudiness (denoted by the letter, 'R') that extends from western Pennsylvania to western Quebec. The leading convective line, consisting of deep and intense convective cells, has a width of about 200 km, while the width of the trailing midlevel stratiform cloud band is about 150 km. The improved RFE model (see Part I for a detailed description) reproduces reasonably well the scale and orientation of the cloud bands (see Fig. 5.1b). Specifically, the leading convective and trailing stratiform rainfall bands, as seen from the satellite imagery, are well represented by two zones of (instantaneous) parameterized and grid-scale rainfall, respectively. This indicates that the leading line, 'C', is mainly convective in nature whereas the trailing stratiform band, 'R', develops in a convectively stable environment. This will be further discussed in section 5.

Now, let us first examine the sequence of evolution from the initiation of the squall convection to the formation of the trailing stratiform rainband using vertical cross-sections of across-band circulations associated with the squall system (Fig. 5.2). Because the trailing stratiform rainband extends gradually northward, different locations of cross sections are taken to better portray the evolution of the internal flow structures (see Fig. 5.1b). At 10 h (Fig. 5.2a), i.e., shortly before the initiation of the squall line, the prestorm environment near Lakes Erie and Ontario is nearly saturated up to 400 hPa as a result of sustained large-scale ascent that occurs ahead of a midlevel baroclinic trough (see Fig. 5.2 in Bélair et al., 1995b). Subsequently, parameterized convection is triggered in the vicinity of the surface cold front and strong upward motion is induced along the leading convective line, 'C' (Fig. 5.2b). In Part I, we have shown that this convective line moves rapidly eastward in a "phase-locked" manner with convectively-forced gravity waves. Of interest here is a zone of organized updrafts (i.e., the stratiform rainband 'R' in Fig. 5.2c) that begins to separate from the eastward-propagating squall line shortly after 12 h, with a transition zone between. This transition zone could be generated by the descending portion of propagating gravity waves and/or the rapid separation of the convective line from the trailing rainband. Then, the trailing updrafts tilt gradually rearward (actually northward in

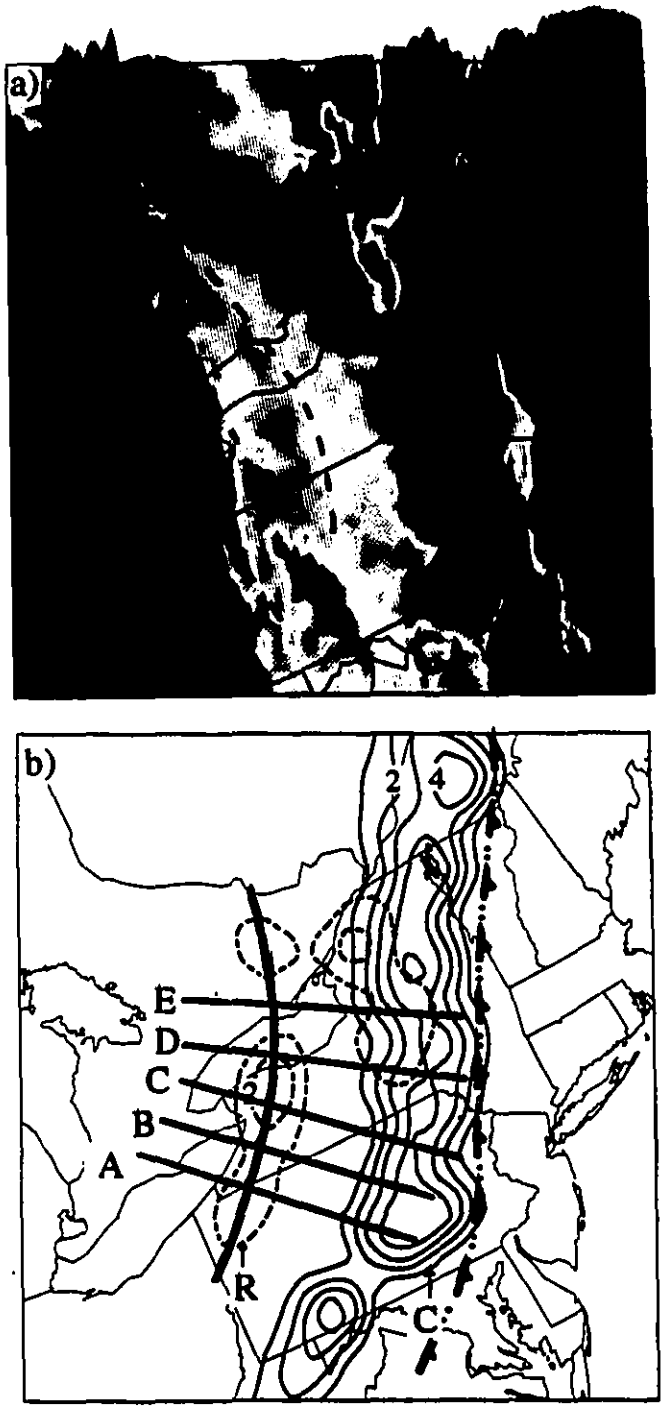

Fig. 5.1 a) GOES satellite infrared imagery at 1800 UTC 14 July 1987; and b) predicted hourly rainfall rates (every 1 mm h^{-1}) by implicit (solid) and explicit (dashed) cloud schemes from 18-h integration. The dashed lines in a) and the thick solid line in b) indicate the position of the trailing rainband. The letters, 'R' and 'C', show the stratiform and convective bands, respectively; similarly for the rest of figures. Lines, 'A' to 'E', indicate the locations of cross sections used in subsequent figures. The double dot-dashed lines denote the position of the predicted gust front.

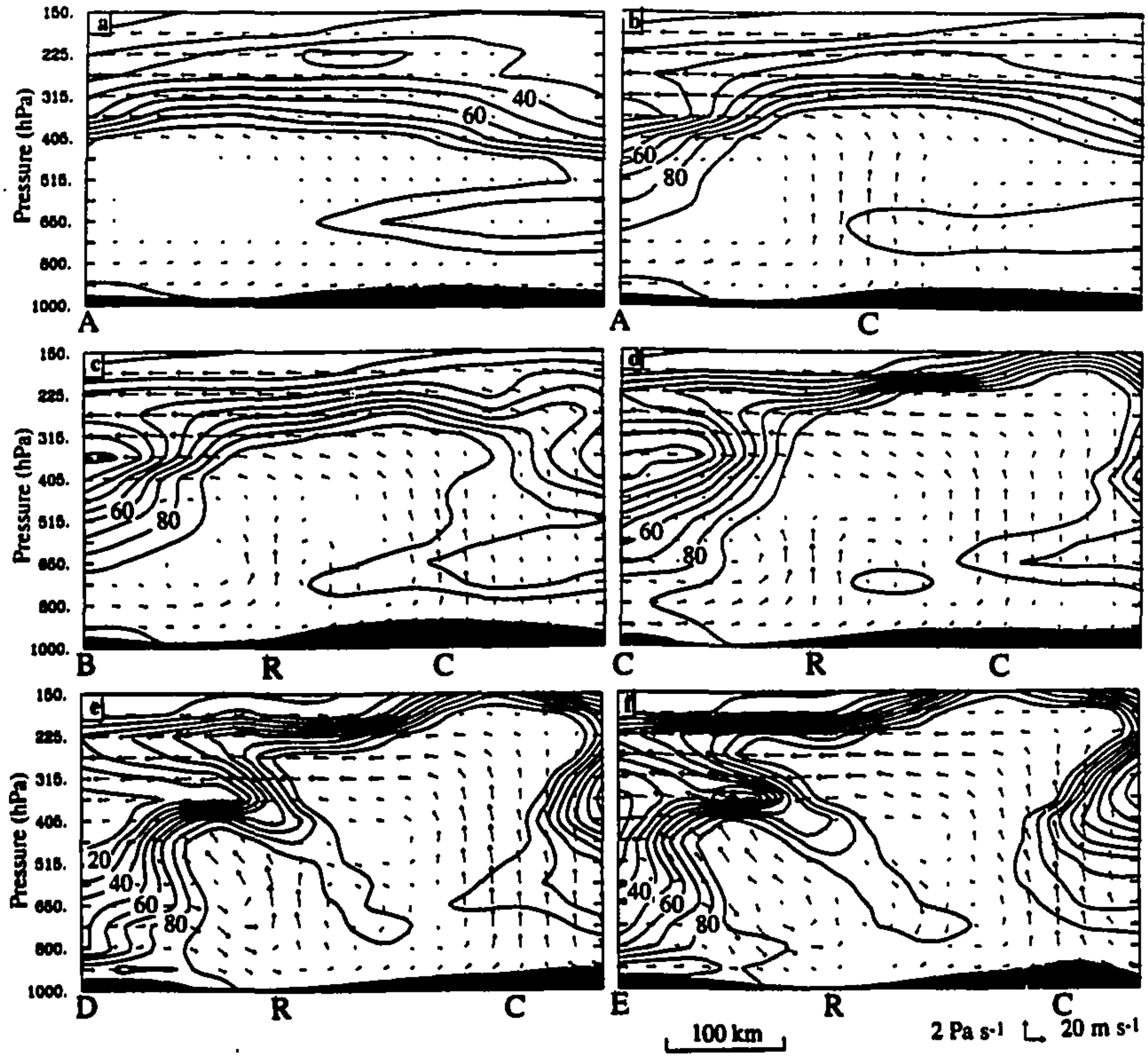

Fig. 5.2 Vertical cross sections of relative humidity (every 10%), superposed with across-band flow vectors, from a) 10-h; b) 12-h; c) 14-h; d) 16-h; e) 18-h; and f) 20-h integrations. The letter at the lower-left corner refers to the location of the cross-section given in Fig. 5.1b.

three dimensions) to become a shallow FTR ascending flow, with a value reaching 40 cm s^{-1} between 18 and 20-h integrations (see Figs. 5.2e-f). Note a surface-based RTF descending flow that emerges beneath the FTR flow around 18 h into the integration. Unlike the 10-11 June case, this RTF flow appears to be associated with the frontal circulation that is enhanced by melting and evaporative cooling from the rainband. Note also that this FTR/RTF circulation moves eastward at a speed much slower than the leading squall line, thus lagging more and more behind with time (see Figs. 5.2c-f). Clearly, the evolution of these two updraft bands is governed by different dynamical mechanisms and physical processes; and the stratiform rainband could not be related to the propagation of gravity waves. As the leading convection advances much further ahead, midlevel drier air is advected from the south into the transition zone. The squall-induced compensating subsidence also tends to dry the air in this area. As a result, a midlevel dry pocket is generated in the transition zone (see Figs. 5.2e-f). Moreover, the stratiform rainband can only penetrate to about 400 hPa, which is consistent with the midlevel cloud top visible from the satellite imagery (cf. Figs. 5.1 and 5.2e-f).

Here, it is necessary to compare the internal flow structures presented above to the conceptual model of squall lines by Houze et al. (1989). Midlatitude squall systems, like those studied by Ogura and Liou (1980), Smull and Houze (1985), Johnson and Hamilton (1988), are typically marked by an overturning updraft along the leading line, an intense FTR ascending flow transporting higher-θ_e air from the boundary layer ahead into the stratiform region, and an *elevated* RTF descending flow bringing midlevel lower-θ_e air down to the boundary layer. These circulations tend to produce characteristic surface pressure perturbations, such as presquall mesolows, mesohighs and wake lows (see Johnson and Hamilton, 1988; Zhang and Gao, 1989). It is evident from Fig. 5.2 that the circulation structure of the 14 July 1987 squall system differs substantially from the above conceptual model. For example, the RTF descending flow associated with the cold front is surface-based and relatively weak so that wake lows did not form at the rear of the system (see Bélair et al., 1995b). More importantly, the FTR ascending flow associated with the trailing rainband does not originate from the boundary layer ahead of the leading convective line. Thus, its energy source can only come partly from the south associated with the low-level jet ahead of the surface front (see Bélair et al., 1995b) and partly from what is left behind by the rapidly propagating convective line. Other circulation features that differ from the Houze et al. conceptual model include: a) the rapid separation of the leading convective line from the trailing rainband due to their different propagation speeds; and b) the nearly upright ascending flow associated with the leading squall convection due to the lack of enough accumulated cold air mass (Rotunno et al., 1988). Therefore, the dynamical forcing mechanisms and physical processes that can account for the development of the trailing stratiform rainband in the present case must be different from those discussed by Smull and Houze (1985) and Zhang and Cho (1992). These subjects will be investigated in detail in sections 4 and 5, respectively.

3. Vorticity structure

After showing the different circulations compared to the classic squall systems, it is of interest to investigate the relative vorticity structures associated with the 14 July 1987 squall system. In particular, Biggerstaff and Houze (1991b) and Zhang (1992) have shown the formation of a deep cyclonic vorticity zone along the leading line, followed by a weak anticyclonic vorticity zone and an intense midlevel mesovortex in the trailing stratiform region of the 10-11 June 1985 squall line (see their conceptual models). For this purpose, a horizontal map of relative vorticity at 600 hPa is given in Fig. 5.3, which shows the development of an elongated cyclonic/anticyclonic couplet of relative vorticity along the trailing stratiform rainband, 'R'. It is evident that the cyclonic vorticity zone is similar to that in the stratiform region of the 10-11 June 1985 squall system, except that it contains little curvature vorticity. However, there are two vortical elements that depart from the conceptual models: one is the development of an anticyclonic vorticity zone at the backedge

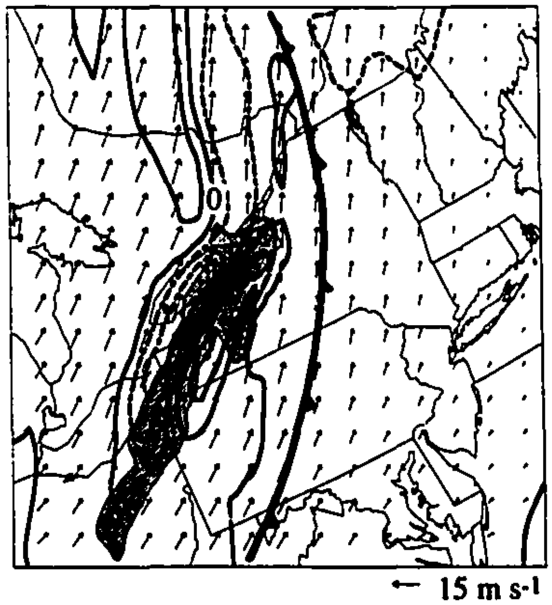

Fig. 5.3 Horizontal map of relative vorticity (every 4 x 10^{-5} s^{-1}) and wind vectors at 600 hPa, from 14-h integration. Solid (dashed) lines are for positive (negative) values. Shadings indicate regions with vertically-integrated cloud water/ice and rainwater/snow greater than 1 mm. The position of the surface cold front is also shown.

of the trailing stratiform rainband and the other is the absence of deep cyclonic flow along the leading squall line.

Vertical cross sections of relative vorticity and vertical circulations, as given in Fig. 5.4, show the development of two cyclonic/anticyclonic vorticity couplets which are correlated, respectively, to the leading convective line and the trailing stratiform rainband. Unlike the mesovortices documented in the previous squall-line studies, these two vorticity couplets move closely with the two updraft zones; there is little interaction between them due to the absence of deep FTR and RTF flows in the low to mid-troposphere. The convectively generated vorticity couplet is relatively weak and only confined below 650 hPa. This couplet intensifies and dissipates in pace with the leading convective line; it diminishes more rapidly after 18-h integration (see Figs. 5.4c,d). In contrast, the vorticity couplet associated with the trailing stratiform rainband is deeper, stronger and more persistent. Of importance is that the cyclonic vorticity band is always embedded in the trailing updraft zone during the life cycle of the system, rather than in a descending flow like that which occurred in the June 10-11 squall system. This vorticity band dissipates as the system weakens, in contrary to the June 10-11 mesovortex which intensifies even during the squall's dissipation stage. Again, these differences are attributable to the absence of the classic flow structures usually found in squall systems.

Of particular interest is the robustness of the anticyclonic vorticity band that is located at the back edge of the stratiform rainband. This vorticity band intensifies first in an upright ascending flow (Figs. 5.4a,b), and then in a slantwise circulation with its center located at the interface between the FTR ascending and RTF descending flows (Figs. 5.4c,d). More interestingly, its intensity even increases during the decaying stage of the system (see Figs. 5.4c-d), and reaches $-2.5 \times 10^{-4}\ s^{-1}$ at 20 h; this value is more than twice the local Coriolis parameter. Thus, this anticyclonic vorticity band becomes the most significant element after 20 h into the integration. This vorticity band lasts for more than 10 hours. It has an across-band scale of 100 km, and its along-band scale is comparable to the length of the stratiform rainband. Such an anticyclonic vorticity band differs from that in the classical squall system, in which the midlevel anticyclonic vortex is relatively shorter-lived due to its interactions with the leading and wake vortices (see Zhang, 1992). So far, considerable work has been done on the understanding of the generation and maintenance of midlevel cyclonic mesovortices within MCSs. However, much less attention has been paid to the development of midlevel anticyclonic vortices. This is because convectively generated anticyclonic vortices occur at smaller scales and tend to be transient, as compared to longer-lived cyclonic vortices. In the present case, the anticyclonic vorticity band clearly outlives its cyclonic counterpart.

To examine how the midlevel vorticity couplets are generated and maintained, the Lagrangian vorticity budget is computed using the following equation:

$$\frac{D(\zeta+f)}{Dt} = -(\zeta+f)\left(\frac{\partial u}{\partial n} + \frac{\partial v}{\partial s}\right) - \left(\frac{\partial \omega}{\partial n}\frac{\partial v}{\partial p} - \frac{\partial \omega}{\partial s}\frac{\partial u}{\partial p}\right) \quad (5.1)$$

where $D(\zeta+f)/Dt$ is the Lagrangian absolute vorticity tendency, ζ is the relative vorticity and all the other variables assume their standard meteorological meaning. The first term on the RHS of (5.1) represents the stretching of the existing absolute vorticity by divergent flow, and the second term is the tilting of horizontal vorticity by nonuniform vertical motion.

It is found from the vorticity budget calculation that vortex stretching is one order of magnitude smaller than tilting of horizontal vorticity in the early stages of the squall system. Thus, Fig. 5.5 only shows a vertical cross section of vortical contribution due to tilting of horizontal vorticity from 14-h integration. Given that the winds along the bands increase with height (see Fig. 5.7), updrafts always tend to produce vorticity tendency couplets (cyclonic on the right and anticyclonic on the left) due to the tilting, whereas downdrafts produce an opposite vorticity couplet. The small cyclonic tendency along the leading line is evidently due to the presence of weak vertical shear (see Fig. 5.7). This result is consistent with that in Biggerstaff and Houze (1991b) and Zhang (1992), who showed that tilting of

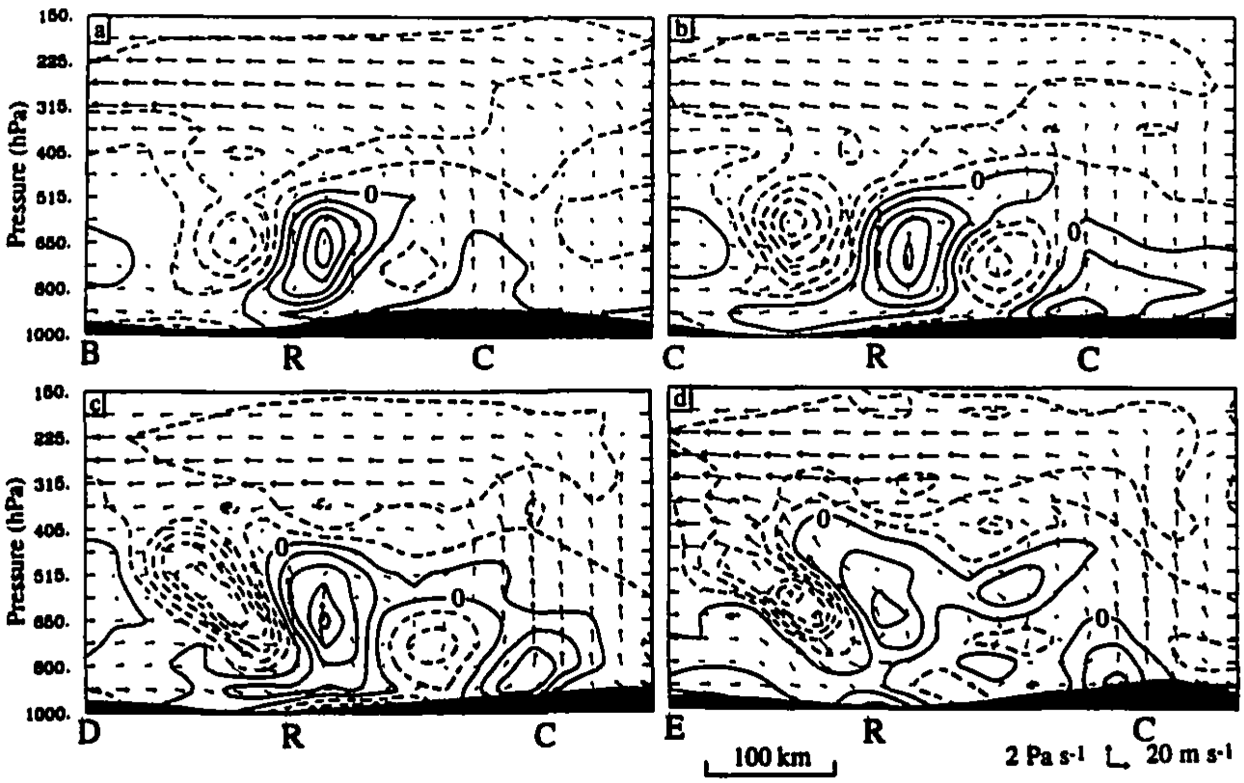

Fig. 5.4 Vertical cross sections of relative vorticity at intervals of 4 x 10^{-5} s^{-1} (solid/positives, dashed/negatives), superposed with across-band flow vectors, from a) 14-h; b) 16-h; c) 18-h; and d) 20-h integrations.

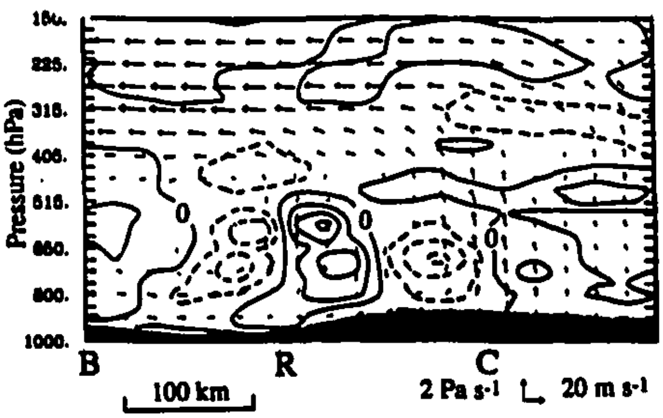

Fig. 5.5 Vertical cross section of tilting of horizontal vorticity at intervals of $2x10^{-5}$ s^{-1} h^{-1}, superposed with across-band flow vectors, from 14-h integration. Solid (dashed) lines are for positive (negative) values.

horizontal vorticity was mainly responsible for the initial production of a vorticity couplet in the 10-11 June 1985 squall system.

During the system's mature stage, i.e., at 18 h, the vortex tilting is still the main vorticity production term at the leading line, 'C' (see Figs. 5.6a,b). However, its contribution to the Lagrangian vorticity tendencies decreases with time as the leading line moves gradually into the weaker baroclinic region ahead (see Fig. 5.7). By comparison, the Lagrangian vorticity tendencies in the trailing stratiform rainband increase during the period (cf. Figs. 5.5 and 5.6a), particularly for the anticyclonic component. It is evident from Figs. 5.6a,b that tilting of horizontal vorticity still plays a dominant role in determining the intensity of the trailing vorticity couplet, but now with additional anticyclonic contribution from the RTF descending flow behind. The vorticity generation also extends to higher levels and becomes rearwardly tilted, in coincidence with the development of the slantwise circulation and vortical couplet in the trailing stratiform rainband (see Figs. 5.2e-f). Because of the development of significant divergent flow during this mature stage, the vortex stretching also makes important contributions to the vorticity production (see Fig. 5.6c). Its effects are to enhance the anticyclonic vorticity in the (divergent) descending flow and the cyclonic vorticity in the lower (convergent) portion of the slantwise ascent. Furthermore, it destroys the upper (divergent) portion of cyclonic vorticity in the slantwise ascent. The net result is that the trailing anticyclonic vorticity gains an anticyclonic spin-up of 6 - 8 x 10^{-5} s^{-1} h^{-1} in a Lagrangian sense. On the other hand, the cyclonic vorticity at its core region tends to weaken due to the offset between the tilting and stretching effects. These results are consistent with the continued growth of anticyclonic vorticity and the decay of cyclonic vorticity in the trailing stratiform rainband (see Figs. 5.4c-d).

The above budget calculations are, to a certain degree, in agreement with the findings of Zhang (1992) that the tilting of horizontal vorticity plays a dominant role during the incipient stage and the vortex stretching produces more important contributions during later

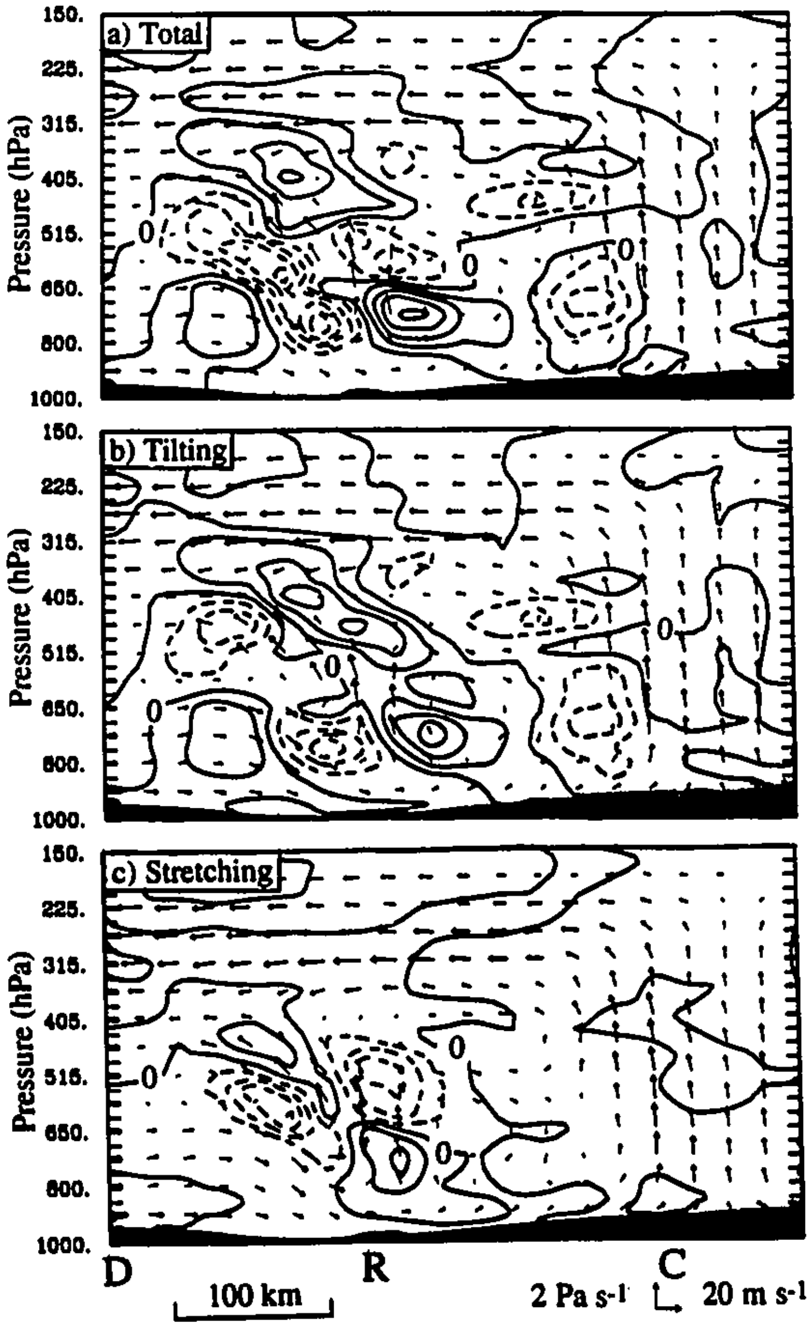

Fig. 5.6 As in Fig. 5.5 but for a) Lagrangian absolute vorticity tendency; b) tilting of horizontal vorticity; and c) vortex stretching at intervals of 2×10^{-5} s^{-1} h^{-1} from 18-h integration.

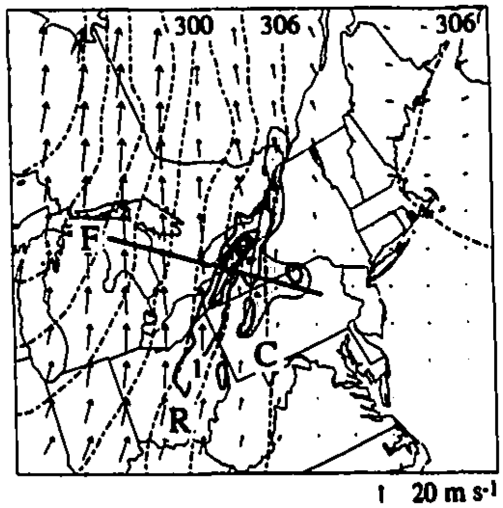

Fig. 5.7 Horizontal map of vertically-integrated cloud water/ice and rainwater/snow (solid, every 2 mm) and potential temperature at 800 hPa (dashed, every 2 K), superposed with vertical wind shear vectors between 400 and 800 hPa, from 14-h integration. The shadings indicate regions with convective precipitation rate greater than 2 mm h^{-1}. Thick solid line, 'F', indicates the location of vertical cross sections used in Figs. 5.8 and 5.9.

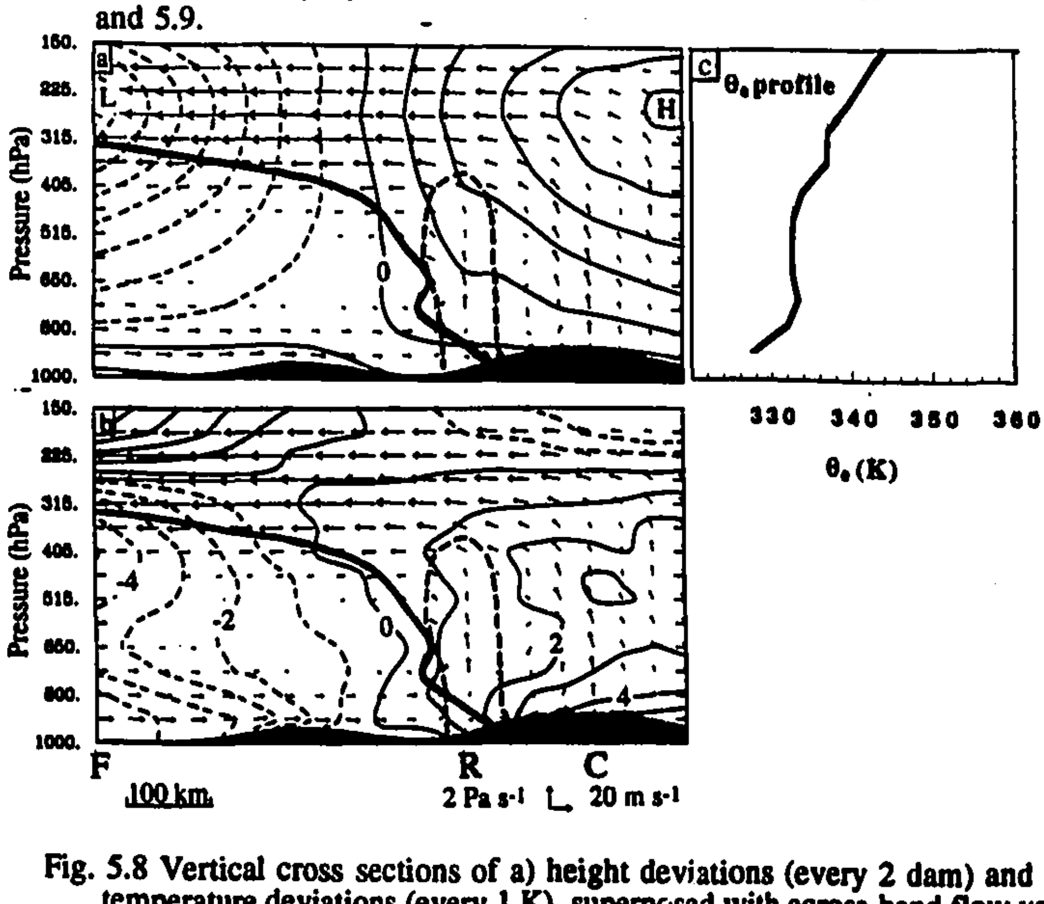

Fig. 5.8 Vertical cross sections of a) height deviations (every 2 dam) and b) potential temperature deviations (every 1 K), superposed with across-band flow vectors, taken along a line given in Fig. 5.7, from 14-h integration. Thick dashed lines represent total cloud water (ice) and rainwater (snow) content greater than 0.1 g kg^{-1}, and the thick solid line is the θ_e = 330 K surface. c) Vertical profile of θ_e taken at point, 'R'.

stages in the development of the 10-11 June 1985 mesovortices. However, in the present case, the trailing vorticity couplet develops along a baroclinic zone, rather than in convectively generated FTR ascending and RTF descending circulations. Thus, the tilting effects are more persistent in the development of the trailing vorticity couplet, particularly for the anticyclonic vorticity band.

4. Dynamical forcing mechanisms

As mentioned in the Introduction, few studies have focused on the dynamical development mechanisms of trailing stratiform precipitation. Zhang and Cho (1992) relates the generation of trailing stratiform precipitation in the June 10-11 squall case to the transport of the boundary-layer high-θ_e air in the prestorm environment. In the present case, the leading convective line almost 'shuts off' the energy supply from the boundary layer ahead, as previously discussed. Thus, we must look for other dynamical mechanisms to explain the development of the present trailing stratiform rainband. In the following, we examine the possible effects of large-scale baroclinicity, the leading convection, orography and CSI.

The effects of large-scale baroclinic forcing can be clearly seen from the distribution of potential temperature and vertical wind shears given in Fig. 5.7. The convective line is initiated along the leading edge of the low-level baroclinic zone and then propagates rapidly into the warm sector having weaker vertical shears. In contrast, the trailing stratiform rainband develops in a strong baroclinic zone. Figure 5.8 shows the vertical structure of the squall system in relation to the baroclinic environment during the early stages of the system's development. A moist isentrope of 330 K is used to delineate approximately the frontal zone. The tilted frontal surface and the baroclinic wave trough are evident in the vicinity of the squall system (see Fig. 5.8a). Strong and deep cold advection occurs behind the trough axis (see Fig. 5.8b), which provides a favorable forcing in lifting the boundary-layer air to saturation. A sounding of equivalent potential temperature, θ_e, taken near the center of the trailing rainband, reveals close to potentially neutral conditions up to 400 hPa (see Fig. 5.8c), which is in significant contrast to the potentially unstable stratification along the leading line (e.g., see Fig. 4.4). This sounding is too stable to activate the Fritsch and Chappell (1980) (hereafter referred to as FC) convective scheme; so only the generation of grid-scale precipitation is possible. Note that such a neutral sounding favors the development of upright ascent due to the existence of little resistance in the vertical. Once latent heating occurs, the baroclinically-forced upward motion will be enhanced. Above 400 hPa, however, the presence of an inversion tends to suppress the upward penetration of the stratiform rainband. Thus, it can only develop in the low to mid-troposphere, as compared to the upper-level development of stratiform precipitation in the classical squall-line conceptual model.

To further ensure that the aforementioned updraft band is generated by the large-scale baroclinicity, another numerical experiment was conducted, in which both the FC and explicit moisture schemes were omitted (Exp. DRY) from the control run (Exp. CTL). Without diabatic heating, the circulations so generated should be dictated by large-scale advective processes. A comparison between Exps. CTL and DRY, as given in Figs. 5.8b and 5.9, shows that the circulations and thermal structures in these two runs are similar, except that the upward motion in Exp. DRY is much weaker and more widespread than in Exp. CTL. Furthermore, there is no transition zone nor separation of updraft bands due to the absence of rapidly propagating gravity waves. Therefore, the large-scale baroclinic forcing at least provides a favorable environment for the development of the leading squall convection and the trailing stratiform rainband.

One may note from Fig. 5.8a that the grid-scale precipitation during the incipient stage occurs on the windward side of a mountain range (i.e., the Appalachians), suggesting that orographically-induced circulations may have assisted the production of the stratiform rainband, 'R'. Normally, orography would tend to provide a favorable lifting on its windward side. To evaluate if the orographical effect is significant in the present case, another experiment was conducted in which the mountains were removed. Results show

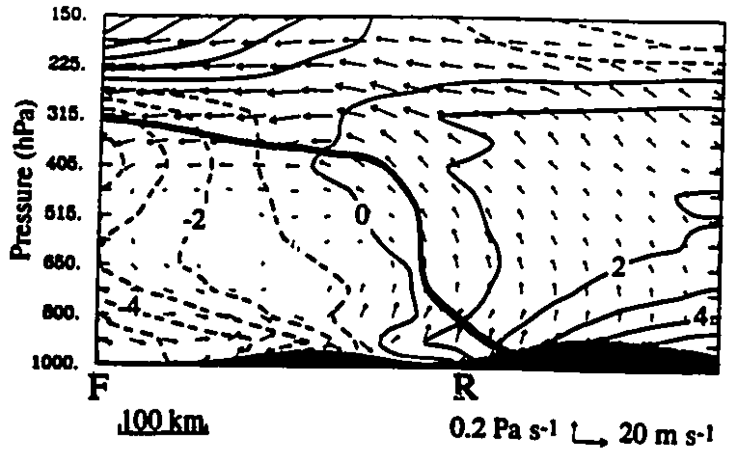

Fig. 5.9 As in Fig. 5.8b but for Exp. DRY (i.e., no latent heat release). Note the use of a different scale for vertical motion.

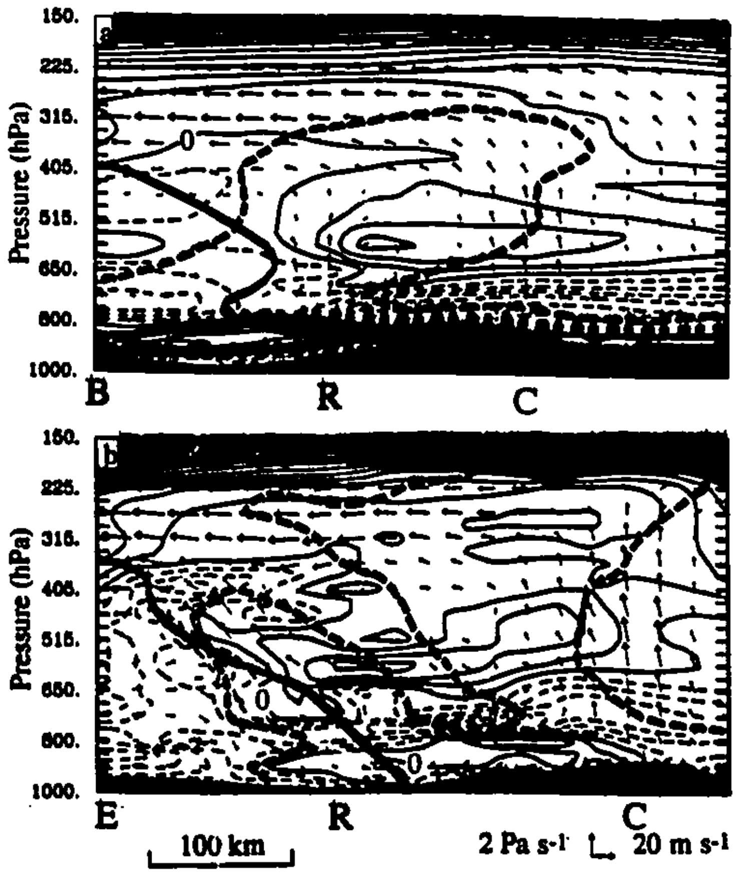

Fig. 5.10 Vertical cross sections of three-dimensional MPV at intervals of 2.5×10^{-7} m^2 K s^{-1} kg^{-1}, superposed with across-band flow vectors, from a) 14-h, and b) 20-h integrations. Solid (dashed) lines are for positives (negatives) values. The thick-dashed lines indicate regions with relative humidity greater than 90%. The thick solid line is the $\theta_e = 330$ K surface.

that the upward motion band at 'R' still develops, but it is delayed for a couple of hours (not shown). Thus, the orography in the present case assists the early generation of grid-box saturation; but it does not control the longitudinal extent of the trailing stratiform rainband since the trailing rainband extends much further to the north of the mountainous region where the cross section was taken.

The slantwise character of the circulation along the rainband, 'R', during the later stages (see Figs. 5.2e,f) suggests that CSI may be operative. To verify this, the dynamical variable, MPV, is computed in three dimensions:

$$MPV = [\frac{\partial \theta_e}{\partial n}(\frac{\partial w}{\partial s} - \frac{\partial v}{\partial z}) + \frac{\partial \theta_e}{\partial s}(\frac{\partial u}{\partial z} - \frac{\partial w}{\partial n}) + \frac{\partial \theta_e}{\partial z}(\frac{\partial v}{\partial n} - \frac{\partial u}{\partial s} + f)]/\rho \qquad (5.2)$$

where *n* and *s* represent the directions perpendicular and parallel to the cross sectional plane, respectively. According to the two-dimensional CSI theory, a saturated region characterized by negative MPV will be subject to moist symmetric instability (Bennetts and Hoskins, 1979; Moore and Lambert, 1993); this instability is conditional when the atmosphere is subsaturated. Thus, small or negative MPV in a saturated environment will exhibit a stronger response to frontogenetic forcing, which could lead to the formation of intense mesoscale rainbands along the frontal zone (see Emanuel, 1985; Thorpe and Emanuel, 1985; Emanuel et al., 1987; Knight and Hobbs, 1988; Zhang and Cho, 1995).

Figure 5.10 shows vertical cross sections of MPV during the incipient (i.e., 14-h) and dissipating (i.e., 20-h) stages. One can see that the convective region is characterized by positive MPV aloft and negative values below due to the presence of potential instability in the boundary layer [i.e., in Eq. (5.2), $\partial \theta_e / \partial z < 0$]. However, the degree of potential instability decreases toward the frontal zone even though the depth of negative MPV increases. At 'R', the vertical stratification is close to neutral during the incipient stage (see Figs. 5.10a and 5.8c), and convectively stable at the later stages, as indicated by the westward tilt of moist isentropes (Figs. 5.10a,b). Such an evolution corresponds well to the change of updraft types from nearly upright to slantwise motion near the stratiform rainband (see Figs. 5.2b-f). A deep layer of negative MPV at 'R' indicates that the circulation associated with the stratiform rainband, though convectively neutral or stable, is unstable to slantwise convection. Note that the area and magnitude of negative MPV at the top portion of the rainband (i.e., near 400 hPa) increase with time. This is due to the northward and upward transport of negative MPV within the rainband, a mechanism similar to that discussed in Zhang and Cho (1992).

Therefore, we may state that the trailing stratiform rainband in the present case develops as a consequence of the frontogenic forcing which is aided by CSI and orographical forcing.

5. Importance of different model physical processes

While the dynamical forcings discussed above are crucial in providing the necessary lifting and favorable environment for the development of the stratiform precipitation, much weaker vertical motion and different circulations occur when cloud condensational processes were omitted (e.g., like that in Exp. DRY). This indicates that cloud physical processes must also play an important role in determining the development of various mesoscale components of the squall system.

We have shown in Fig. 5.1b that the leading convective and trailing stratiform rainbands are produced, respectively, by the parameterized and explicit condensation schemes. Their vertical heating/cooling structures and relationships to the squall circulations can be seen from Fig. 5.11, namely, the parameterized and explicit schemes are well correlated with deep updrafts along the leading line and shallow and slantwise ascent in the stratiform region, respectively. Although the parameterized scheme is capable of generating the grid-box saturation at the upper levels through cloud detrainment and convectively forced ascent (see Fig. 5.11b), it contributes little to the development of the trailing stratiform precipitation. This is in significant contrast to the June 10-11 squall system in which a large portion of the trailing stratiform precipitable water was transported

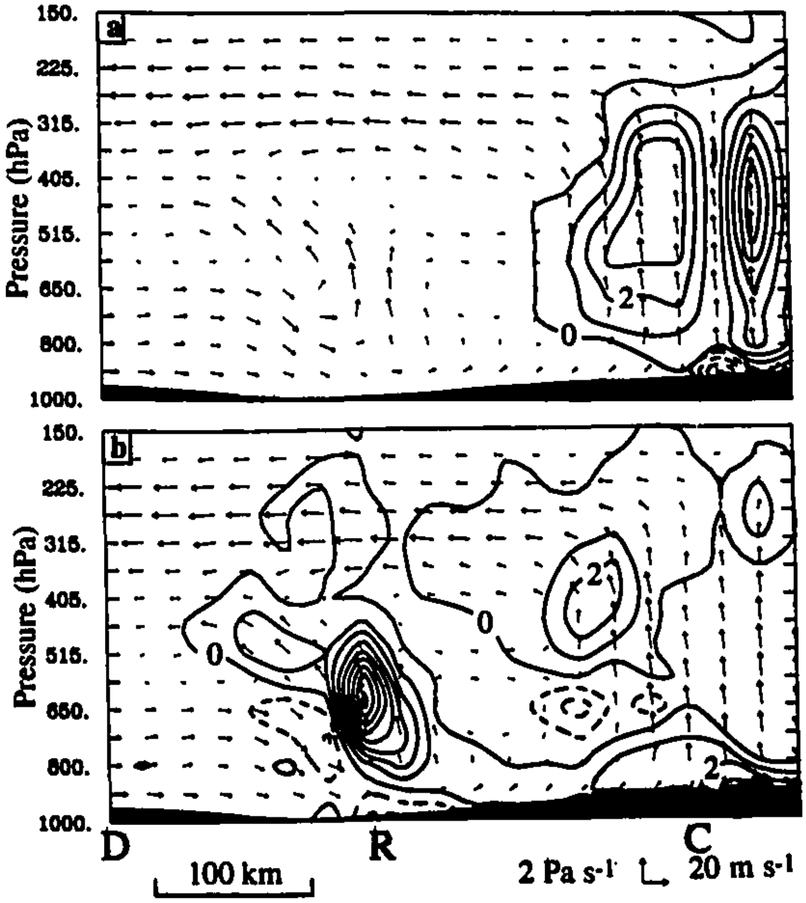

Fig. 5.11 Vertical cross sections of temperature tendencies generated by a) the FC convective parameterization and b) the explicit moisture scheme at intervals of 1 ^{0}C h^{-1}, superposed with across-band flow vectors, from 18-h integration. Solid (dashed) lines are for positive (negative) values.

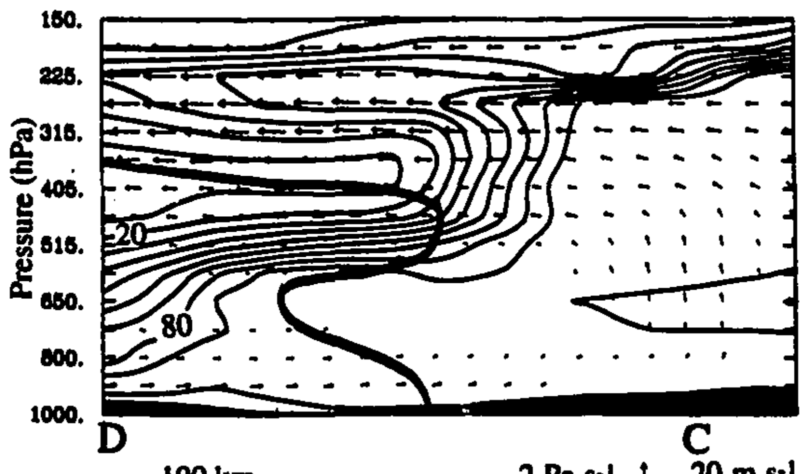

Fig. 5.12 As in Fig. 5.2e but for Exp. NOEX (no grid-scale latent heating). The thick solid line is the $\theta_e = 330$ K surface.

from the leading convection through the FTR ascending flow (Gallus and Johnson, 1991; Biggerstaff and Houze, 1991a; Zhang and Gao, 1989; Zhang et al., 1994). Furthermore, most of the stratiform precipitation in the present case occurs in the low- to mid-troposphere, whereas for typical squall systems it often occurs in the mid to upper- levels. There are several factors that could be responsible for the different behaviors of precipitation production in the present stratiform region. These include: i) a weak convective forcing including the parameterized heating and moistening along the leading line, e.g., a heating rate of 5 °C h^{-1} in the present case (see Fig. 5.11a) as compared to about 10 °C h^{-1} in the June 10-11 case (see Fig. 3b in Zhang et al., 1994); ii) the rapid separation of the leading line from the trailing rainband so that coherent vertical circulations forced by these two heating regimes could not develop; and iii) the absence of an elevated strong RTF flow descending to the ground, or the absence of a deep cold pool such that the leading squall's circulation could never tilt upshear during its life cycle. Because of the latter two factors, little convective available potential energy (CAPE) from the boundary layer ahead of the system could be transported into the stratiform region, as mentioned previously.

To isolate the individual roles of convective parameterization and grid-scale microphysics in the development of the trailing stratiform rainband, two additional numerical experiments were conducted, in which either the grid-scale latent heating was neglected (Exp. NOEX) or the FC scheme was turned off (Exp. NOFC), while keeping all the other parameters identical to the control run. It is evident from Fig. 5.12 that in Exp. NOEX, the model fails to reproduce the slantwise circulation or trailing rainband near 'R', even with the favorable frontogenetical and orographical forcing. This further indicates the different roles of dynamical forcing and physical processes in the formation of the trailing rainband. The neglect of grid-scale heating does not affect significantly the structure and evolution of the leading convective line, as expected, except for the magnitude of upward motion. On the other hand, when the FC scheme was turned off (i.e., Exp. NOFC), the

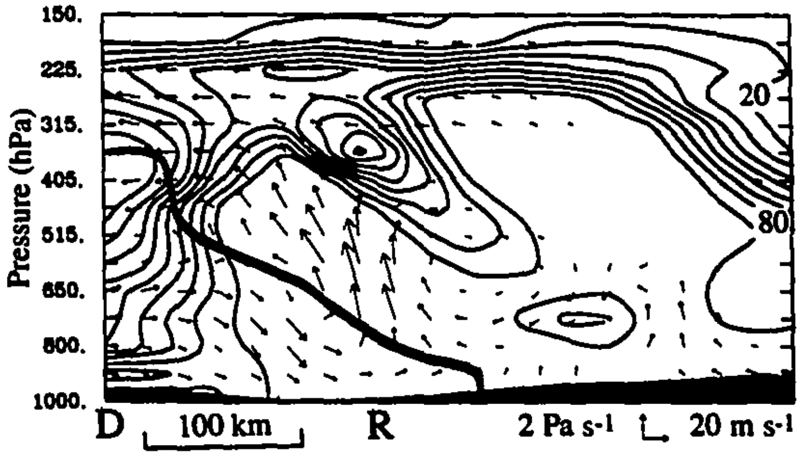

Fig. 5.13 As in Fig. 5.2e but for Exp. NOFC (no FC scheme). The thick solid line is the $\theta_e = 330$ K surface.

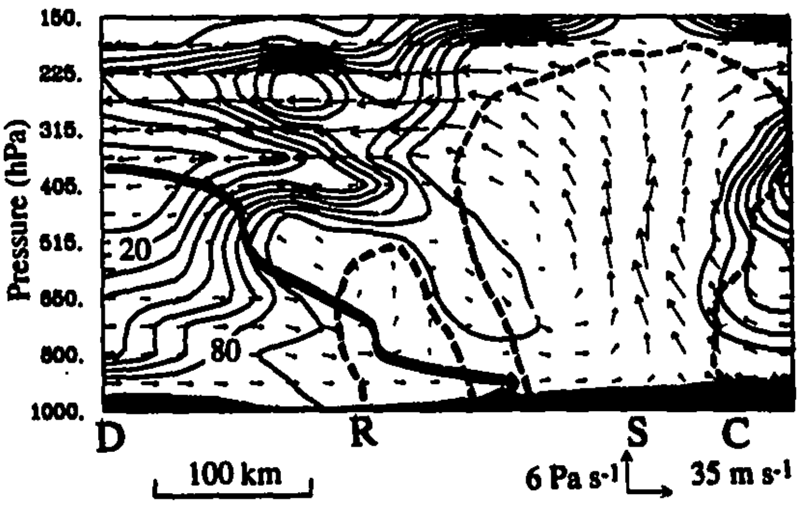

Fig. 5.14 As in Fig. 5.2e but for Exp. 2XFC (double heating and moistening tendencies in the FC scheme). Thick dashed lines represent total cloud water (ice) and rainwater (snow) content greater than 0.1 g kg^{-1}, and the thick solid line is the $\theta_e = 330$ K surface.

model reproduces well the timing and location of the stratiform rainband (Fig. 5.13); but it misses entirely the deep updrafts associated with the leading convective line. This also could be expected since the grid-box saturation at some distance ahead of the front could not be achieved. Of importance is that both the FTR ascending and RTF descending currents at the rainband, 'R', are much stronger than those in the control run (cf. Figs. 5.2e and 5.13). This is because the higher-θ_e air in the boundary layer ahead can now be transported directly into the baroclinic zone and then released in the FTR ascending flow. Thus, the role of the leading convective line is to remove most of CAPE, thereby limiting the rapid development of the trailing stratiform precipitation in the baroclinic zone. The results also show the importance of the proper coupling between implicit and explicit cloud schemes in mesoscale models (see Molinari and Dudek, 1992; Zhang et al., 1988; 1994). Because of the absence of energy competition between the implicit and explicit precipitation in Exp. NOFC, the rainband circulation has been overamplified. It should be mentioned that when a simple supersaturation removal scheme was used instead of the more sophisticated explicit moisture scheme, a weaker RTF descending flow resulted, indicating that its intensity is sensitive to the melting and evaporative cooling.

To test the hypothesis that the weak convective forcing accounts partly for the absence of classical squall-line circulations in the present case, the moistening and heating tendencies in the FC convective scheme are artificially doubled (Exp. 2XFC) after 14-h integration when the leading and trailing rainbands are separated (see Fig. 5.2c). This is equivalent to a hypothetical situation in which more CAPE, like that in the June 10-11 case, were present in the prestorm environment. It is apparent from Fig. 5.14 that the circulations so generated are markedly different from those in Exp. CTL. For example, much stronger updrafts (>5 Pa s^{-1}) develop at the leading line, as expected. Meanwhile, a wider and deeper layer of grid-box saturation occurs right behind the leading line, as can also be expected. However, the ascending flow tends to tilt more rearward to form a deep FTR flow, which allows the transport of high-θ_e air from the boundary layer ahead into the

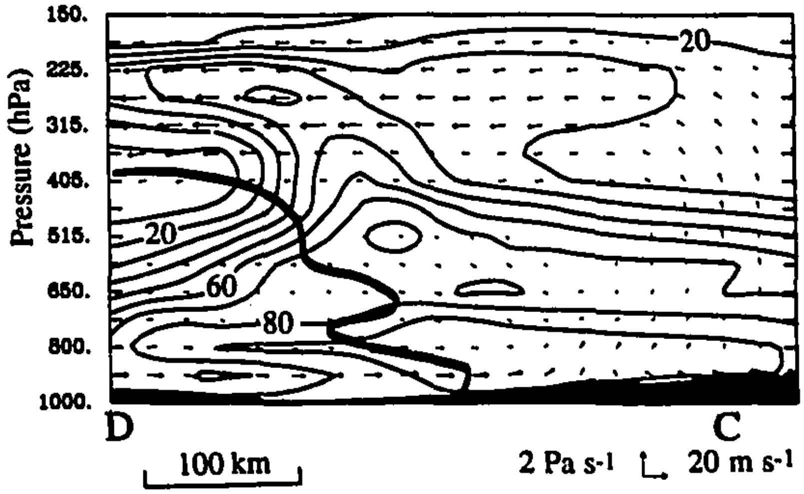

Fig. 5.15 As in Fig. 5.2e but for Exp. KUO. The thick solid line is the $\theta_e = 330$ K surface.

upper-level stratiform region. As the stratiform precipitation occurs, an elevated RTF flow begins to emerge as a result of the development of a strong midlevel mesolow (Smull and Houze 1987), and melting and evaporative cooling (Zhang, 1992). Now, these flow structures look similar to those in the classical squall-line model (i.e., Houze et al., 1989), except that the RTF descending flow only takes place locally due to the lack of large-scale support (see Zhang and Gao, 1989). On the other hand, this enhanced convective forcing affects only slightly the intensity of the circulations near the frontal zone (note the different scales used in Figs. 5.2 and 5.14), as compared to that in Exp. CTL.

Finally, it is of interest to evaluate the model's sensitivity to the use of the Kuo (1974) convective scheme (Exp. KUO), since this scheme is currently used at the Canadian Meteorological Center (CMC) for operational forecasts. As shown in Part I, the model is still able to produce a line of convection propagating eastward, as can also be seen from Fig. 5.15, but in a manner different from that produced by the FC scheme. Moreover, this upward motion and the convective feedback from the Kuo scheme are unable to generate a deep saturated layer along both the leading line and frontal zone (cf. Figs. 5.2e and 5.15). Thus, the model fails to reproduce the slantwise circulation or stratiform cloudiness observed near the baroclinic zone. These differences can be attributed to the ways to achieve convective stabilization between the FC and Kuo schemes. For example, the Kuo scheme neglects the effect of moist downdrafts and has a heating maximum typically located at a level lower than that by the FC scheme. This heating profile tends to favor the lower-level mass/moisture convergence and the development of a pressure trough or mesolow at the surface, as discussed in Bélair et al. (1994, 1995b). Furthermore, the "b" parameter in the Kuo scheme may be too large for an intense MCS like the present one. Hence, the mass perturbation or upward motion generated in Exp. KUO is much weaker than that in Exp. CTL. This in turn reduces the upward transport of moisture to moisten the midtroposphere. Anthes (1985) commented that the Kuo type of convective parameterization may be only appropriate in predicting the initiation of MCSs.

6. Summary and conclusions

In this study, the mesoscale structures of a trailing stratiform rainband associated with the intense squall system that was responsible for the 14 July 1987 Montreal flood are investigated using 20-h predictions of the case with an improved version of the RFE model. The dynamical and physical processes that are responsible for various components of the squall system, as well as its vortical structures, are examined. The most important findings are summarized as follows.

a) We found that although the squall system is characterized by a leading convective line followed by a trailing stratiform rainband, the associated circulation structures differ substantially from those in the classical midlatitude squall system. These include the rapid propagation and separation of the leading convection from the trailing rainband, the development of a surface-based instead of an elevated RTF descending flow and a shallow FTR ascending flow associated with the stratiform precipitation, the generation of low- to midlevel rather than mid- to upper-level stratiform cloudiness and the development of a strong anticyclonic vorticity band at the back edge of the stratiform region.

b) Because of the above circulation structures, the trailing stratiform rainband is not fed directly by the boundary-layer high-θ_e air ahead. It is dynamically forced by frontogenetical processes, and aided by the release of conditional symmetric instability and local orographical lifting. The intensity of the rainband is determined by latent heat released in the frontal circulations. This finding seems to be particularly relevant to other midlatitude squall lines that develop in close proximity to cold fronts in moderate CAPE environments.

c) A number of sensitivity experiments have been conducted to gain insight into the development of various mesoscale components of the squall system. It is shown that the parameterized and explicit cloud schemes are responsible for the generation of the leading convective line and trailing stratiform rainband, respectively. The results further reveal the importance of an appropriate coupling of a convective parameterization and an explicit moisture scheme in obtaining the realistic prediction of an MCS. It is found that one of the roles of the leading convection is to remove most of the potentially unstable conditions, mainly through parameterized moist downdrafts, and to limit the development of the trailing stratiform precipitation. When Kuo's convective parameterization is used instead of the FC scheme, the model fails to reproduce the trailing rainband due to the lack of parameterized downdrafts and the generation of too weak mass perturbations.

d) We found that the internal flow structure of a squall system is very sensitive to the intensity of convective forcing along the leading line. When the convective heating and moistening tendencies in the FC scheme are doubled to simulate the presence of larger CAPE in the prestorm environment, the internal circulations of the squall system are much closer to those in the classical midlatitude squall-line model, even though the larger-scale environments differ.

e) Vorticity budgets have been examined to understand the development of an intense vorticity couplet in the trailing stratiform region. We found that tilting of horizontal vorticity contributes the most to the amplification of the vorticity couplet, particularly during the squall's incipient stage. Because of favorable contributions from the tilting and stretching, the anticyclonic vorticity band can still intensify during the squall's decaying stage and it becomes a dominant mesoscale circulation of the squall system.

Finally, it is necessary to point out that some of the above conclusions are obtained only from one numerical case study. More case studies, especially using high-resolution observations, are needed to generalize some of the above conclusions. In particular, more attention needs to be paid in the future to the importance of CAPE in the prestorm environment, low-level wind shear, convectively-generated cold downdrafts, elevated rear inflow jets and orography, in the generation of various internal circulation structures of midlatitude squall systems.

Chapter 6

Along-line variability of a PRE-STORM squall line

6.1 Presentation of article 4

After examining the various internal structures associated with the 10-11 June 1985 and 14 July 1987 squall lines in the preceding chapters, the along-line variability of these structures is investigated in this chapter using a numerical prediction of a third midlatitude squall line that occurred during 26-27 June 1985 over the PRE-STORM network. This case has been analysed by Trier et al. (1991) and Lin and Johnson (1994). The purpose of this chapter is to demonstrate further the mesoscale predictability of the internal flow structures of this squall system, as verified against high-resolution network observations, and examine these structures due to large-scale and mesoscale circulations.

6.2 Article 4

A numerical study of the along-line variability of a frontal squall line during PRE-STORM. By Stéphane Bélair and Da-Lin Zhang.

Submitted to *Mon. Wea. Rev.*, October 1994.

Abstract

Despite the considerable research in the understanding of two-dimensional structures of squall lines, little attention has been paid to the along-line variability of these convective systems. In this study, the roles of large-scale and mesoscale circulations in the generation of along-line variability of squall lines are investigated, using an 18-h prediction of a frontal squall line, that occurred during 26-27 June 1985 PRE-STORM, with the Canadian regional finite-element (RFE) mode It is shown that the model reproduces reasonably well a number of surface and vertical circulation structures of the squall system, as verified against available network observations. These include the initiation, propagation and disintegration of the squall system, surface pressure perturbations and cold outflow boundaries, a midlevel mesolow and an upper-level mesohigh, a front-to-rear (FTR) ascending flow overlying an intense rear-to-front (RTF) flow, and a leading convective line followed by stratiform precipitation regions.

It is found that the vertical circulations at the northern segment of the squall line differ significantly from those at its southern segment, including the absence of the RTF flow and midlevel mesolow, the early dissipation of deep convection and different types of stratiform precipitation. It is shown that the along-line variability of the squall's internal circulations results primarily from the interaction of convectively generated pressure perturbations with a midlevel baroclinic trough. The large-scale trough provides an extensive RTF flow component in the southern portion of the squall system and an FTR flow component in the north, whereas the midlevel mesolow tends to enhance the RTF flow to the south and the FTR flow to the north of the mesolow during the mature stage. The along-line variability of the squall's circulations appears to be partly responsible for the generation of different weather conditions along the line. The mechanisms that account for the development of an upper-level stratiform region in the southern segment and a lower-level stratiform region in the northern portion of the squall line are also examined.

1. Introduction

In the recent years, considerable progress has been made on the understanding of two-dimensional structure and evolution of midlatitude squall lines. These mesoscale convective systems (MCSs) often exhibit a line of deep convection, followed by a region of stratiform precipitation (e.g., Ogura and Liou 1980; Smull and Houze 1985, 1987; Johnson and Hamilton 1988; Biggerstaff and Houze 1991a). Their internal flow structures are characterized by a front-to-rear (FTR) ascending current of high-θ_e air overlying an elevated rear-to-front (RTF) or descending rear inflow jet of low-θ_e air (e.g., Moncrieff 1981; Smull and Houze 1985, 1987; Rutledge et al. 1988; Zhang and Gao 1989). Midlevel mesovortices or intense cyclonic vorticity concentrations (Stirling and Wakimoto 1989; Brandes 1990; Bartels and Maddox 1991; Biggerstaff and Houze 1991b; Zhang 1992), as well as midlevel mesolows (Zhang and Gao 1989; Lin and Johnson 1994) and upper-level mesohighs (Zhang and Gao 1989; Gallus and Johnson 1992) have been found to exist in trailing stratiform regions. Most of these features have been summarized in the conceptual model of squall lines by Houze et al. (1989).

In contrast, much less attention has been paid to the along-line variability of squall's internal structures due partly to the limited area of high-resolution observations, and partly to the limited capability of numerical models to resolve multiple scales of circulations. Recently, the variability of rear inflow jets has been the subject of a few studies. For instance, Klimowski (1994) noted from dual-Doppler analyses that the rear inflow jet is stronger in regions of high reflectivity cores, indicating the importance of convective-scale forcing. Numerical studies showed that the variation of rear inflow jets could be related to convectively-induced midlevel mesovortices. Zhang and Gao (1989) and Zhang (1992) noted from the simulation of the 10-11 June 1985 PRE-STORM (Preliminary Regional Experiment for STORM-Central, see Cunning 1986) squall system that the elevated rear inflow jet is stronger to the south of a midlevel mesovortex. Thus, they suggested to visualize the formation of a rear inflow jet as part of the mesovortex circulation. Davis and

Weisman (1994) and Skamarock et al. (1994) simulated squall lines that exhibit asymmetric circulations in the vicinity of mesovortices when the effect of earth rotation is included. Such three-dimensional flow structures even arise at the convective scale, as demonstrated by Weisman (1993), in which rear inflow jets are enhanced in the middle of a convective bow-echo line due to the development of meso-γ-scale vortices at the ends of the line (i.e., bookend vortices).

Similarly, little attention has been paid to the role of large-scale flows, which normally govern the development and organization of deep convection along squall lines. In particular, squall lines often occur in the vicinity of midlevel short-wave troughs or upper-level jet streams (e.g., Ogura and Liou 1980; Srivastava et al. 1986; Leary and Rappaport 1987; Johnson and Hamilton 1988; Carbone et al. 1990). Thus, we should expect that the internal circulation structure of squall lines may vary, depending on their location with respect to the large-scale disturbances. For example, the circulation of a squall line that develops at the base of a baroclinic trough, where the RTF ambient flow is stronger, could differ from that of a squall line which occurs to the north of the base or ahead of the trough. In this regard, Zhang and Gao (1989) showed the importance of a large-scale RTF flow component associated with an upper-level jet stream prior to the development of the 10-11 June 1985 PRE-STORM squall line. In other cases, such a large-scale support may be less obvious, particularly for MCSs in which rear inflows are weak and less extensive (e.g., see Smull and Houze 1987). Nevertheless, even within a single linear squall system with a length scale of several hundreds kilometers, the vertical circulation at one location would differ from that at other locations when it is embedded in a large-scale curved flow.

The purpose of the present study is to address the roles of large-scale and mesoscale circulations in the generation of variable internal structures within midlatitude squall lines, using an 18-h simulation of a frontal squall system that occurred during 26-27 June 1985 PRE-STORM. It should be mentioned that this squall system has been documented by

Trier et al. (1991) and Lin and Johnson (1994). They showed that the squall line, having a length scale of 1500 - 1800 km, developed ahead of a surface cold front with a pronounced baroclinic trough aloft. Their analyses also revealed the development of an upper-level stratiform region at the rear of the squall system, with classical two-dimensional flow structures as described before. Moreover, Lin and Johnson (1994) noted two different types of RTF flows: an elevated one that intensified in response to the development of a midlevel mesolow (Smull and Houze 1987), and a surface-based one that was related to the cold frontal circulation. These two observational analyses provide useful information on the understanding and model verification of the June 26-27 squall system for the present study. However, these two analyses are limited only to the southern segment of the squall system that was covered by the PRE-STORM network. It remains uncertain whether or not similar vertical circulations would develop at the northern segment of the squall line. If not, what are the roles of the large-scale and mesoscale circulations in determining the different internal structures of the squall system? Thus, the primary objectives of this study are to a) examine the mesoscale predictability of the variable internal circulations of the 26-27 June 1985 squall line using a high-resolution research version of the Canadian regional finite-element (RFE) model; b) investigate the along-line variability of the squall's internal structures; and c) clarify the multiple-scale interactions involved in the development of a rear inflow jet in the present squall line.

The presentation of the results is organized as follows. The next section describes briefly the main features of the RFE model and the initial conditions. Section 3 provides verification of the 18-h model prediction against available observations, and examines the two-dimensional vertical structure of the squall line. Sections 4 and 5 discuss the along-line variability of the internal structures and weather conditions of the squall system due to large- and meso-scale circulations, respectively. A summary and concluding remarks are given in the final section.

2. Model description and initial conditions

An improved version of the RFE model is used for this study, with a high-resolution uniform grid interval of 25 km over the central domain covering most of the United States and southern Canada (see Fig. 6.1). Table 6.1 summarizes the basic model features, which are the same as those used in Bélair et al. (1994, 1995b). Briefly, the RFE model uses a modified version of the Fritsch and Chappell (1980) (hereafter referred to as FC) convective parameterization scheme (Zhang and Fritsch 1986) that is coupled with an explicit moisture scheme predicting cloud water (ice) and rainwater (snow) (Hsie et al. 1984; Dudhia 1989; Zhang 1989). This version of the model is similar to that used operationally at the Canadian Meteorological Center (CMC), except for the use of the above physics package and a high-resolution grid length. The model is initialized at 1200 UTC 26 June 1985 with conventional meteorological observations using the same procedures as those described in Bélair et al. (1994). No supplementary data were used for the model initialization, since the PRE-STORM network did not collect detailed observations until 1800 UTC 26 June when the squall line under study was initiated.

At the model initial time, there is a large-scale surface cold front that extends from western Texas to western Ontario, with a low-pressure zone located over western central Kansas (see Fig. 6.2). The surface circulation shows an anticyclonic northerly cold current associated with the high-pressure center over Wyoming, and a warm (moist) southerly flow ahead of the cold front. It is evident that the two air currents converge along the front, suggesting the important role of the frontal lifting in the initiation of deep convection about 6 h later. Furthermore, it is found that the prefrontal environment is conditionally unstable; it has convective available potential energy (CAPE) of ~ 2000 J kg^{-1} (not shown). At the midlevel, a large-amplitude baroclinic trough corresponding to the surface front is present (see Fig. 6.3), with the base of the trough located just upstream of the PRE-STORM network (i.e., over Kansas and Oklahoma). Note that the midlevel flow associated with the trough is nearly equivalent barotropic, whereas the flow ahead of the trough is nearly barotropic (i.e., having little gradient). This indicates that further destabilization of the prefrontal environment due to cold advection, as discussed in Hobbs et al. (1990), is not likely to occur in the present case. For additional details on the environmental conditions, the reader is referred to Trier et al. (1991).

3. Model verification

Before examining the variable internal structures of the 26-27 June PRE-STORM squall line, it is important to ensure that the RFE model could reproduce reasonably well the basic structure and evolution of the system as verified against all available observations. In this section, radar summaries, rawinsonde observations, Doppler data, satellite imagery and surface analyses are used to help validate the model prediction and describe the general evolution of the squall system. In the next, we will verify first the prediction of surface features, including precipitation, area of convection, sea-level pressure and temperature fields, and then investigate the predicted tropospheric structures of the squall system.

a. Surface features

It is found that the squall line was initiated ahead of the surface cold front over Nebraska and Kansas at about 1800 UTC 26 June (not shown). Then, as the daytime boundary layer developed, the convective activity expanded rapidly north- and southward along the front, leading to the generation of a long and intense line of deep convection that extends from Texas to Lake Superior by 0000 UTC 27 June (see Figs. 6.4a and 6.5a). Precipitation also occurred behind the convective line over South Dakota, which was associated with the lower-level stratiform cloudiness visible in satellite imagery (cf. Figs. 6.4a and 6.5a). At 0600 UTC 27 June, the convective activity in the southern portion of the squall line, i.e., that was located over the PRE-STORM network, began to dissipate but still remained well organized (see Figs. 6.4b and 6.5b). In contrast, the northern portion of the convective system became disintegrated. There was also a large area of stratiform

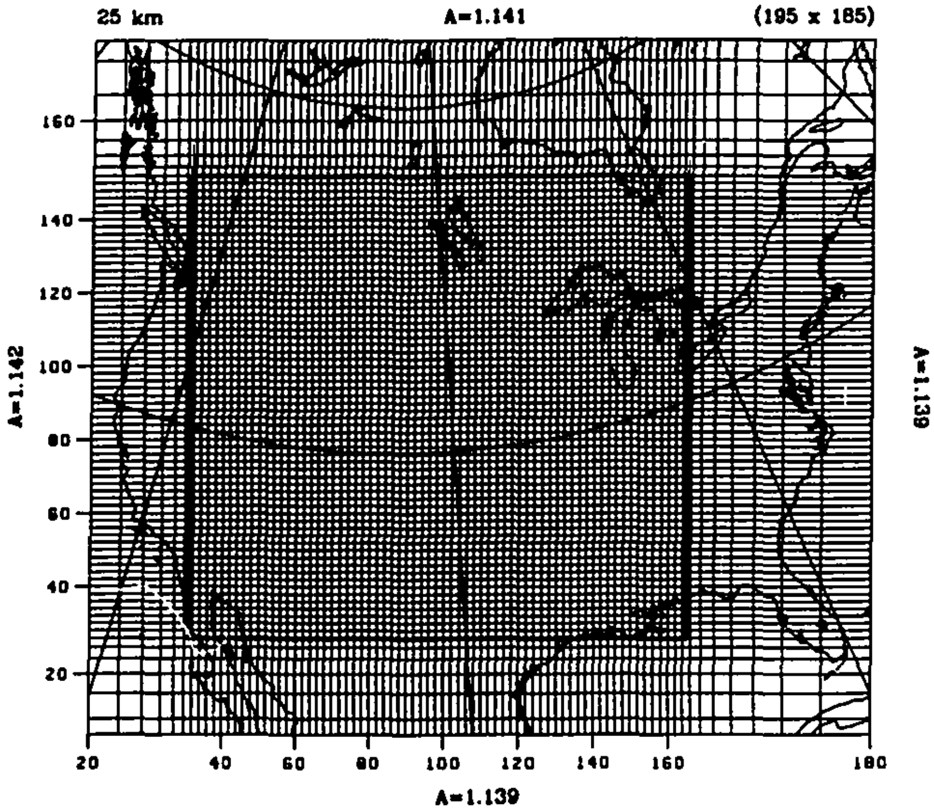

Fig. 6.1 Portion of the 195 x 185 hemispheric variable grid mesh projected on a polar stereographic plane. The heavy rectangle indicates the central uniform high-resolution domain of 25 km with the grid size increasing by a constant outward.

TABLE 6.1. Summary of the mesoscale RFE model

Numerics

- 3-D, hydrostatic, primitive equations;
- semi-implicit time discretization;
- semi-Lagrangian scheme for three-dimensional advection (time step: 300s);
- linear finite-elements in (x,y,σ);
- variable horizontal resolution grid overlaid on a polar stereographic projection (25 km in fine grid);
- 19 σ levels with high resolution in the lowest 150 hPa;
- second order horizontal diffusion for temperature, vorticity, and divergence;
- 0.5° orography field.

Physics

- Planetary boundary layer (PBL) based on turbulent kinetic energy;
- diagnostic PBL height;
- implicit vertical diffusion;
- surface energy budget based on force-restore method;
- diurnal cycle with solar and infrared fluxes at the ground modulated by clouds;
- infrared and solar radiation fluxes calculated at all levels;
- diagnostic cloud cover;
- Fritsch-Chappell scheme for parameterized moist convection;
- explicit moisture scheme containing prognostic equations for cloud water/ice and rainwater/snow.

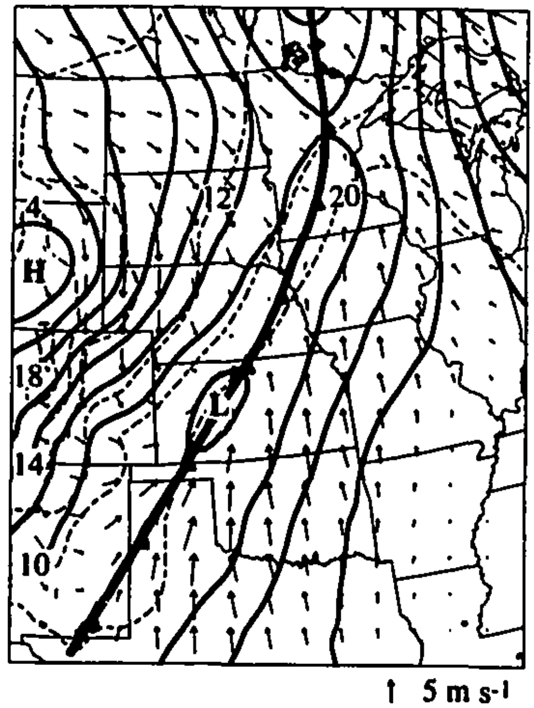

Fig. 6.2 Model initial conditions: sea-level pressure (solid, every 2 hPa) superposed with the surface wind vectors and temperature (dashed, every 4 °C) at 1200 UTC 26 June 1985.

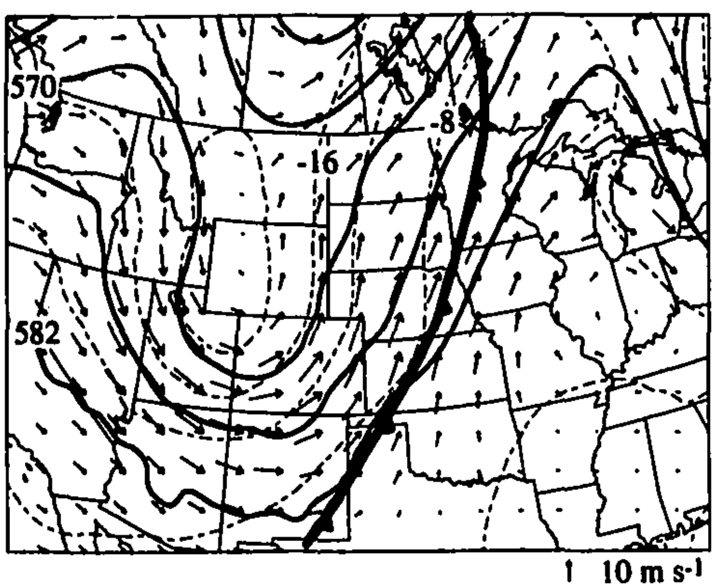

Fig. 6.3 As in Fig. 6.2 but for geopotential height (solid, every 6 dam) and temperature (dashed, every 4 °C), superposed with horizontal wind vectors, at 500 hPa.

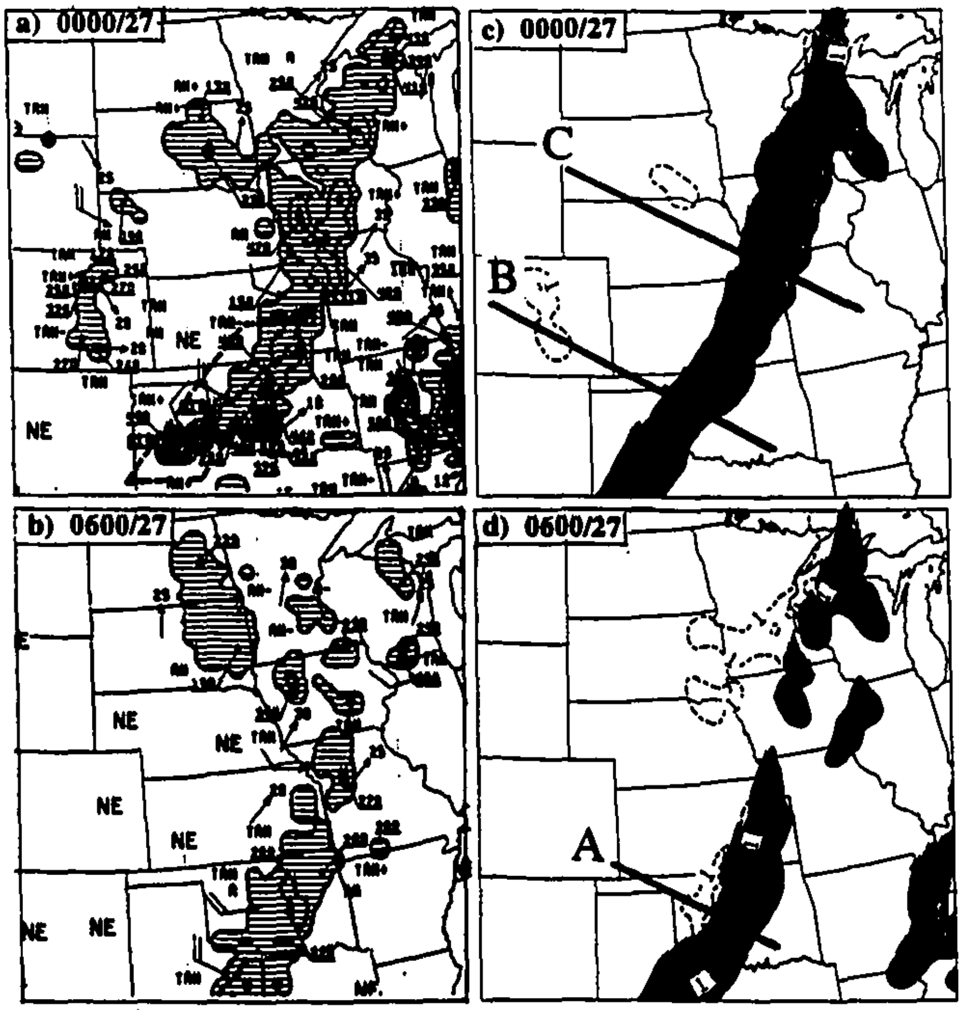

Fig. 6.4 Left panel shows radar summary charts at a) 0000 UTC; and b) 0600 UTC 27 June 1985. Right panel shows the predicted grid-scale (dashed) and convective (shaded) rainfall rates with contours of 1, 5 and 10 mm h^{-1} from c) 12-h and d) 18-h integrations.

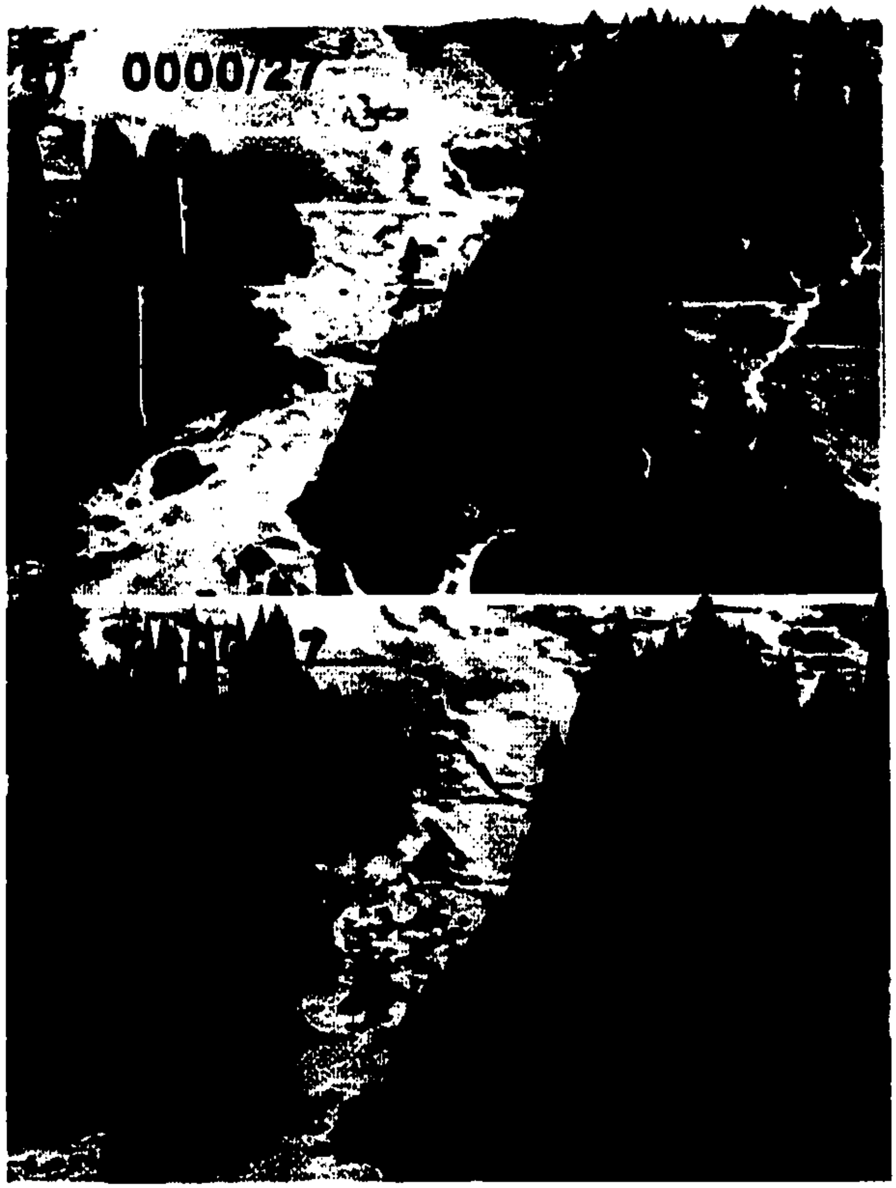

Fig. 6.5 Satellite imagery at a) 0000 UTC; and b) 0600 UTC 27 June 1985.

precipitation to the rear of the disintegrated portion of the squall system over North and South Dakotas (Figs. 6.4b and 6.5b).

As compared to the observations, the model predicts well the initiation of the squall line at nearly the right time and location (not shown). The predicted distribution and orientation of convective activity along the squall line compare favorably to the radar-echo summaries and satellite imagery during both the formative and mature stages (cf. Figs. 6.4a-d and 6.5). In particular, the model also predicts well the disintegration and maintenance of the squall system at its respective northern and southern segments at 0600 UTC 27 June. Most of the precipitation is convective in both the prediction and observations (Figs. 6.4c,d). Only at later stages the model produces two trailing stratiform regions: one over Minnesota and the other over Oklahoma, which conform reasonably well to the observed (cf. Figs. 6.4b, 6.4d and 6.5b).

Marked changes have also taken place at the surface during the past 18 h, except for the high pressure zone over Wyoming which was nearly quasi-stationary. First, a pressure ridge, extending from the high-pressure zone to southeastern Oklahoma, was generated as a consequence of the formation of the squall system. This ridge split the frontal trough into two parts: one as the original mesolow being pushed northeastward and the other formed as a presquall mesotrough to the southern end of the squall system. As will be shown, this ridge coincided with a stronger RTF descending flow in the midtroposphere. Second, the squall line left behind an intense cold outflow superposed on the cold front, which was more obvious during the daytime to the south of the surface mesolow. Evidently, this evaporatively driven cold outflow helped accelerate the movement of the squall line, particularly for the southern convective segment which propagated at a speed (i.e., 9 m s^{-1}) much faster than its northern counterpart (i.e., 4 m s^{-1}). By 0600 UTC 27 June, the southern squall line had traversed the PRE-STORM network.

A comparison between Figs. 6.6a-b and 6.6c-d indicates that the RFE model reproduces reasonably well the main surface features during the early and mature stages

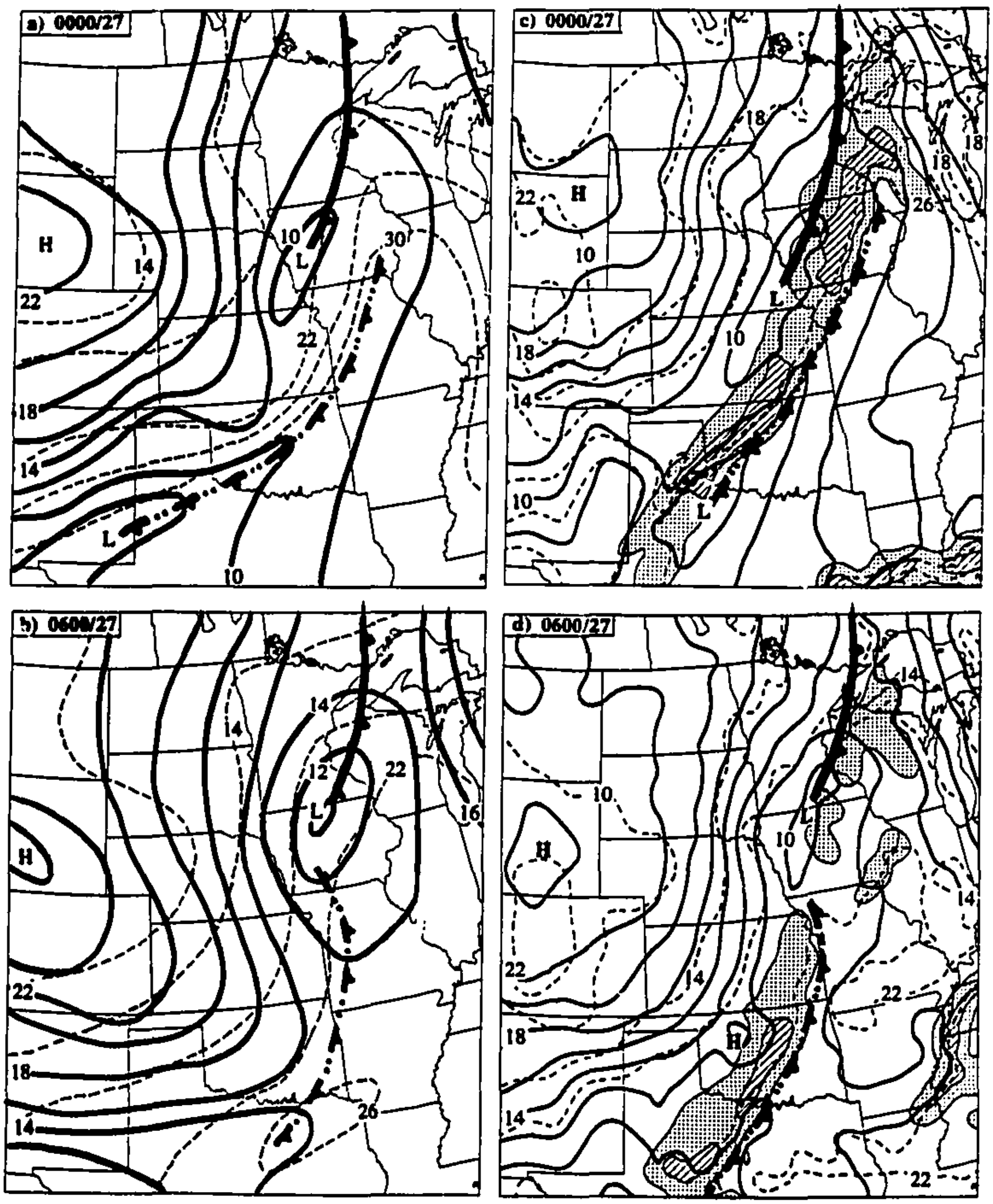

Fig. 6.6 Left panel shows sea-level pressure (solid, every 2 hPa) and surface temperature (dashed, every 4 °C) at a) 0000 UTC; and b) 0600 UTC 27 June 1985. Right panel shows the corresponding fields from c) 12-h; and d) 18-h integrations. Shadings show the predicted convective rainfall rates with contours of 1, 5 and 10 mm h^{-1}. Cold frontal symbols with double dots indicate outflow boundaries.

(i.e., at 12- and 18-h integrations), such as the low- and high-pressure centers over Iowa and Wyoming, the presquall mesotrough and cold outflow boundary. The orientation and propagation of the squall front, produced by parameterized moist downdrafts in the FC scheme, are reasonably captured by the model (see Fig. 6.6c). However, the predicted squall front exhibits a little weaker intensity than the observed at the formative stage. This has caused slightly slower movement of the squall system, especially for the southern segment of the squall system. This weaker intensity occurs because the RFE model underpredicts the development of the daytime boundary layer ahead of the front, namely, the surface temperature is 3 - 4 °C colder than the observed.

It should be mentioned that there are several notable deficiencies with the 18-h model prediction. For example, the model appears to have delayed the precipitation production over Arkansas by 6 h; similarly for the precipitation over North and South Dakotas (see Fig. 6.4). The model is also unable to reproduce some too small-scale features, such as the multiple convective lines and their associated pressure perturbations ahead of the surface front (see Trier et al. 1991), due to the use of relatively coarse grid resolution and imperfect initial conditions. Nevertheless, the above results show that the model prediction captures reasonably well the main features of the squall line, and could therefore be used to investigate non-observable structures of the system and the mechanisms that are responsible for the along-line variability of the squall's internal circulations.

b. Tropospheric structures

Both observational analyses of Trier et al. (1991) and Lin and Johnson (1994) indicated the development of some typical mesoscale structures of squall lines during the mature-to-dissipating stages, such as a stratiform region, a rear inflow jet and a midlevel mesolow. The Doppler radar analysis by Trier et al. (1991) showed that a well-developed couplet of the FTR and RTF currents occurred as early as 0000 UTC 27 June (see their Fig. 21). Similar flow structures were also detected by the PRE-STORM upper-air sounding network, but at later times (see Figs. 4 and 9 in Lin and Johnson 1994). A vertical cross section taken along a line similar to that given in Trier et al. (1991) and Lin and Johnson (1994) shows that, although the scales of the observed and predicted circulations are different, the basic two-dimensional circulation structures of the squall system are well captured by the RFE model (see Fig. 6.7). A strong FTR ascending flow occurs within a deep, nearly saturated layer from the leading convective line to the trailing stratiform region; its trailing segment at upper levels extends rearward a few hundreds of kilometers. It is found that this nearly saturated region is distributed with negative moist potential vorticity (MPV) (not shown). This implies the presence of moist symmetric instability, which develops as a result of transporting potentially unstable air from the presquall boundary layer, after being relieved by upright convection at the leading line, into the FTR sloping ascent region, a process as described by Zhang and Cho (1992). Beneath the stratiform cloudiness, a system-relative RTF current with a maximum speed of 12 m s^{-1} transports extremely dry air (with minimum relative humidity < 10%) in the midlevels into the system, thereby causing intense sublimative/evaporative cooling and descending near the leading edge of the current. This cold downdraft air penetrates into the boundary layer at the leading edge of the squall line, forming the surface squall front at which strong convergence occurs between the FTR and RTF currents. In some cases, like in the June 10-11 squall system, mesolows may form at the back edge of the stratiform region, when adiabatic warming associated with the RTF descending flow exceeds diabatic cooling (see Johnson and Hamilton 1988; Zhang and Gao 1989). In the present case, however, both the prediction and observations show a mesoridge or a weak mesohigh behind the system (see Figs. 6.6c,d), indicating that diabatic cooling within the RTF descending current dominates. The development of the wake lows appears to depend on the intensity of RTF descending flow, temperature lapse rate and moisture content in the lower troposphere, the propagation of the squall system, as well as the intensity of large-scale baroclinicity.

Figure 6.8 compares the predicted geopotential heights and horizontal winds at 700 hPa to the observed during the system's mature stage. It is evident that the RFE model

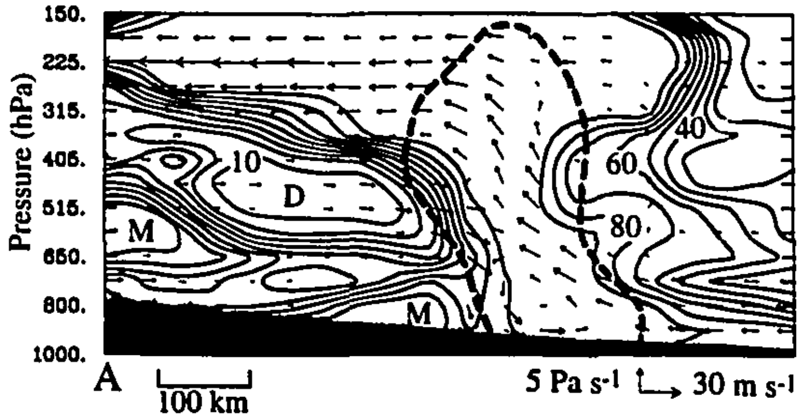

Fig. 6.7 Vertical cross section of relative humidity (solid lines, every 10 %) and precipitable water boundaries (> 0.1 g kg^{-1}), superposed with line-normal relative flow vectors, taken along line 'A' given in Fig. 6.4d, from 18-h integration. Letters, 'D' and 'M', indicate dry and moist centers, respectively.

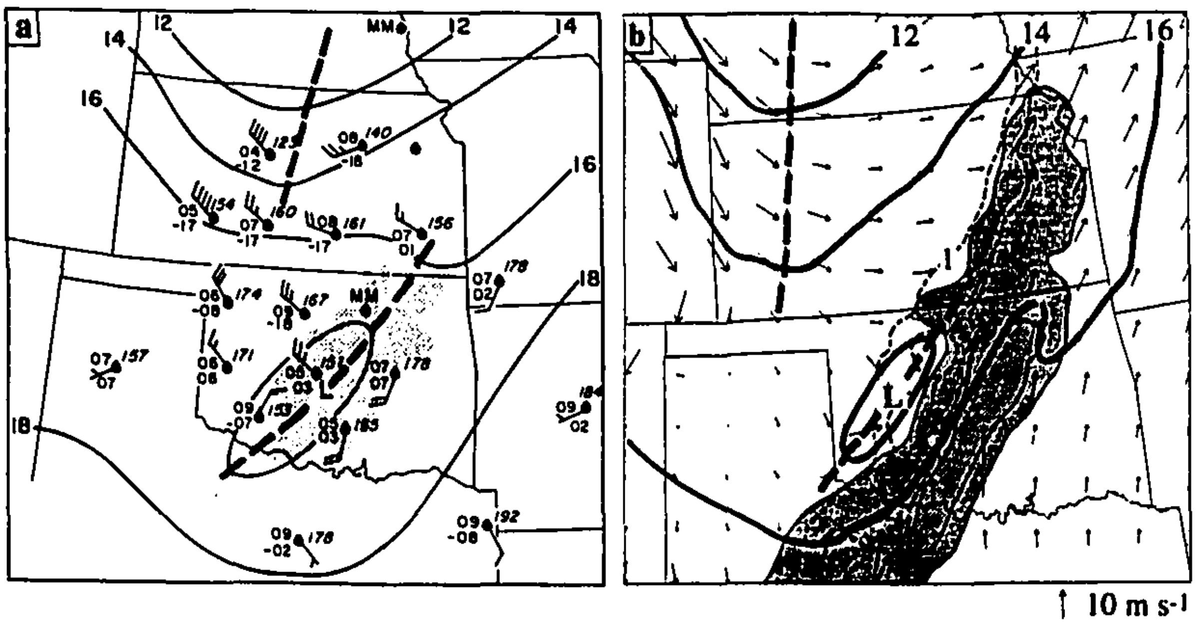

Fig. 6.8 Horizontal maps of 700-hPa geopotential height (solid, every 2 dam) from a) the observations, superposed with horizontal winds (a full barb is 5 m s^{-1}) and radar echo at 0600 UTC 27 June (Courtesy of S. Trier); and b) 18-h integration, superposed with wind vectors and grid-scale (dashed) and convective (shadings) rainfall rates with contours of 1 and 5 mm h^{-1}. The dashed lines denote height trough axis. Note that the height values are excess over 300 dam (i.e., 12 = 312 dam).

captures well two scales of circulations, i.e., a large-scale trough, in which the squall system is embedded, and a mesolow in the trailing stratiform region of the system. Their orientations and relative locations are reasonably reproduced. Lin and Johnson (1994) also noted the development of such a midlevel low-pressure zone during the mature stage. As will be discussed in the next two sections, these two scales of circulations have significant implications with respect to the along-line variability of internal flow structures and weather conditions along the squall line.

For the sake of later discussion, it is necessary to separate the mesoscale from the large-scale signals and determine the relationship between the squall development and the mesoscale pressure disturbances. These can be achieved by applying a simple scale-separation technique similar to that utilized by Maddox (1980b) to the height and temperature fields. First, the two fields are spatially filtered on two horizontal grid meshes with different resolutions (i.e., see filters 1 and 2 in Fig. 6.9). The low-resolution grid mesh (filter 2) only represents disturbances with wavelengths longer than 500 km (i.e., large-scale), whereas all the wavelengths greater than 150 km (i.e., mesoscale and large-scale) are included on the high-resolution grid mesh (filter 1). Then, a band-pass filter is obtained by subtracting the results of filter 2 from filter 1, thus yielding the characteristics of convectively generated perturbations on the scale of 150-500 km. It is clear from Figs 6.10a,b that this scheme isolates well the vertical structure of mesoscale perturbations in the vicinity of the squall system from the large-scale circulations. There are a midlevel mesolow and an upper-level mesohigh associated with the squall system; they are centered at locations where convergence and divergence are maximized, respectively. Apparently, the midlevel mesolow is hydrostatically produced by net warming in the FTR ascending flow and evaporative/sublimative cooling in the RTF descending flow, with its center situated at the interface between the warming above and cooling below, as has also been found by Zhang and Gao (1989). In contrast, the upper-level mesohigh is produced by the net adiabatic and parameterized detrainment cooling above the intense updrafts and the net

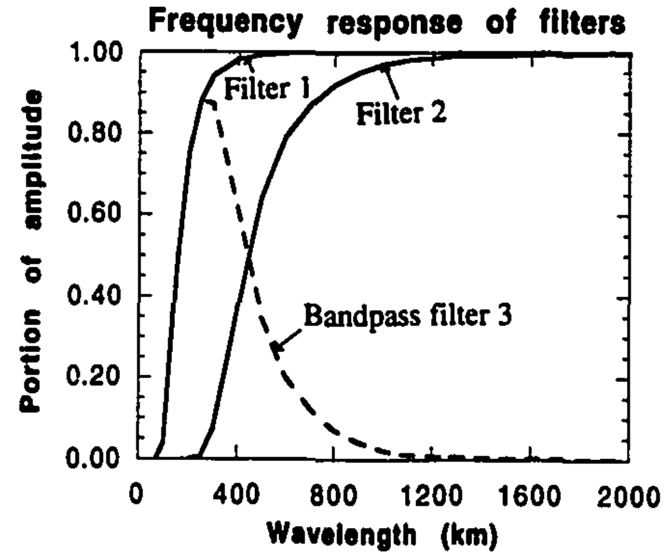

Fig. 6.9 Portion of returned amplitude versus wavelength (km) by the low-pass filters 1 and 2 and the bandpass filter 3.

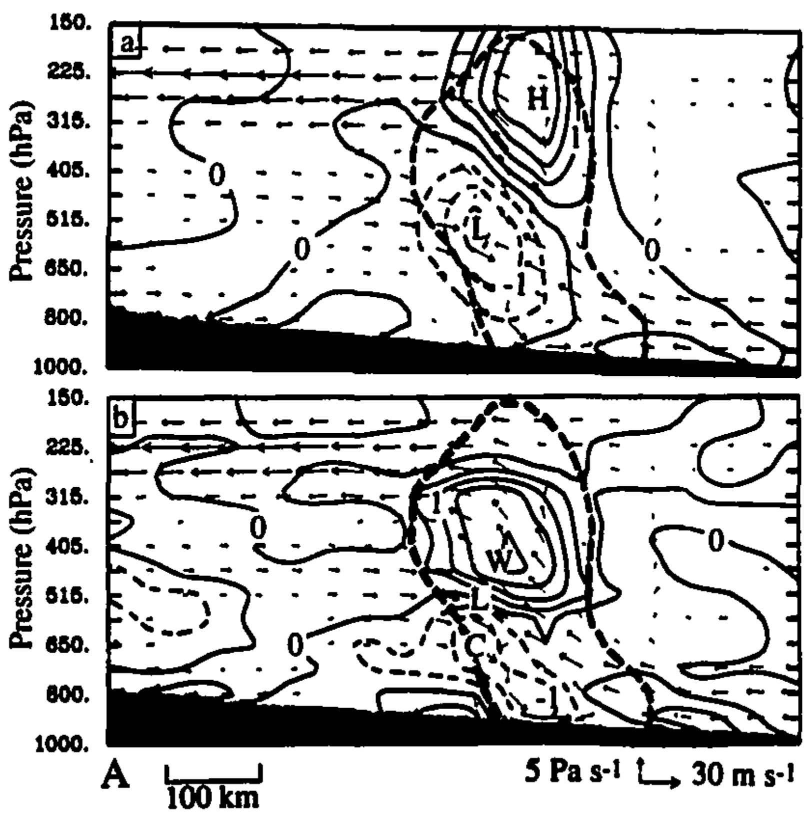

Fig. 6.10 As in Fig. 6.7 but for a) mesoscale height perturbations (every 5 m); and b) temperature perturbations (every 0.5 °C). Solid (dashed) lines are positive (negative) values. Letters, 'L' and 'H', 'W' and 'C', denote the center of the mesolow and mesohigh, warming and cooling, respectively.

warming below. Such an upper-level mesohigh has been frequently observed (e.g., Fritsch and Maddox 1981a; Fritsch and Brown 1982; Maddox et al. 1981; Gallus and Johnson 1992), and simulated by other numerical models (e.g., Fritsch and Maddox 1981b; Gao et al. 1990). This feature can also be seen from the analysis of Lin and Johnson (1994).

Finally, the vortical structure of the squall line is presented in Fig. 6.11, which depicts the development of a deep rearwardly tilted cyclonic vorticity zone along the interface between the FTR and RTF flows. This vortical zone coincides with the vertically tilted pressure trough that extends from the surface to 350 hPa (cf. Figs. 6.10a and 6.11). This vorticity concentration, mostly related to horizontal shear, is generated initially through vortex stretching in the frontal zone where both cyclonic vorticity and convergence are strong. As the squall system intensifies, the FTR-RTF flow convergence increases, particularly at midlevels, causing the rapid spin-up of cyclonic vorticity near 500 hPa. This development mechanism appears to differ from that which occurred in other squall-line cases, such as the June 10-11 squall system, in which midlevel mesovortices are initiated by tilting of horizontal vorticity at the back edge of a stratiform region (e.g., Biggerstaff and Houze 1991b; Zhang 1992). This difference appears to be attributable to the important role of the frontal forcing in determining the internal vorticity structure of the squall system. Nevertheless, the tilting of horizontal vorticity contributes to the intensification of a lower-level anticyclonic/cyclonic vorticity couplet in the stratiform region (see Fig. 6.11), a process similar to that discussed in Biggerstaff and Houze (1991b) and Zhang (1992).

4. Along-line variability due to large-scale circulation

We have shown that the southern segment of the squall system, i.e., over the PRE-STORM network, contains many meso-β-scale structures that are similar to those in the conceptual model of midlatitude squall lines (Houze et al. 1989). In this section, we investigate whether or not these classical structures would appear at other portions of the squall line, and then clarify the role of large-scale circulation in determining the along-line

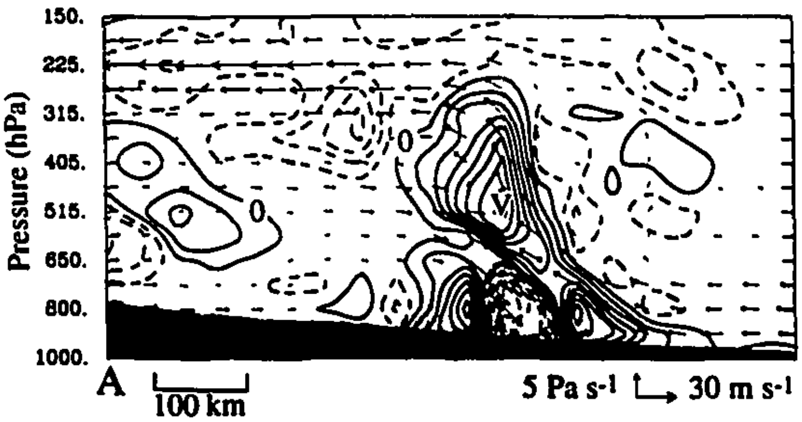

Fig. 6.11 As in Fig. 6.7 but for relative vorticity (every 5×10^{-5} s^{-1}). Letter, 'V', denotes the center of midlevel cyclonic vorticity.

variability of the squall's internal structures. The effect of convectively generated disturbances will be discussed in the next section.

To examine the relationship between the large-scale circulation and the generation of along-line variability, Fig. 6.12 compares the two-dimensional circulations at the southern segment of the squall system to those at the northern segment during the early stages of the system (i.e., from 12-h integration). One can see that the prestorm environment is potentially unstable everywhere ahead of the cold front with higher-θ_e air in the lowest 100 hPa. This is consistent with the rapid expansion of deep convection along the line during the stage. However, the two-dimensional circulations in the northern segment differ significantly from those in the southern one. Specifically, the southern squall system exhibits an RTF descending current that transports midlevel lower-θ_e air downward into the boundary layer, whereas in the north there is little evidence of the RTF flow. Instead, there are two FTR ascending flows that transport boundary-layer high-θ_e air upward: one along the frontal zone into the middle troposphere and the other through deep convection into the upper levels. These flow structures conform more or less to the development of more extensive, mixed middle and upper-level stratiform clouds in the north (see the satellite images in Figs. 6.5a,b). In contrast, the stratiform clouds developed in the south only appear in the upper troposphere, like those described in the Houze et al. (1989) conceptual model. Furthermore, the upward motion at the southern convective line is more intense than that in the north, likely due to the presence of stronger low- to midlevel convergence associated with the elevated RTF flow. In the next, we discuss separately the mechanisms that are responsible for the generation of these different two-dimensional circulation structures.

a. The RTF descending flow in the southern segment

Rear inflow jets have been the focus of considerable research in recent years (e.g., Smull and Houze 1985,1987; Rutledge et al. 1988; Zhang and Gao 1989; Schmidt and Cotton 1990; Zhang 1992; Weisman 1992). Much, however, remains to be understood

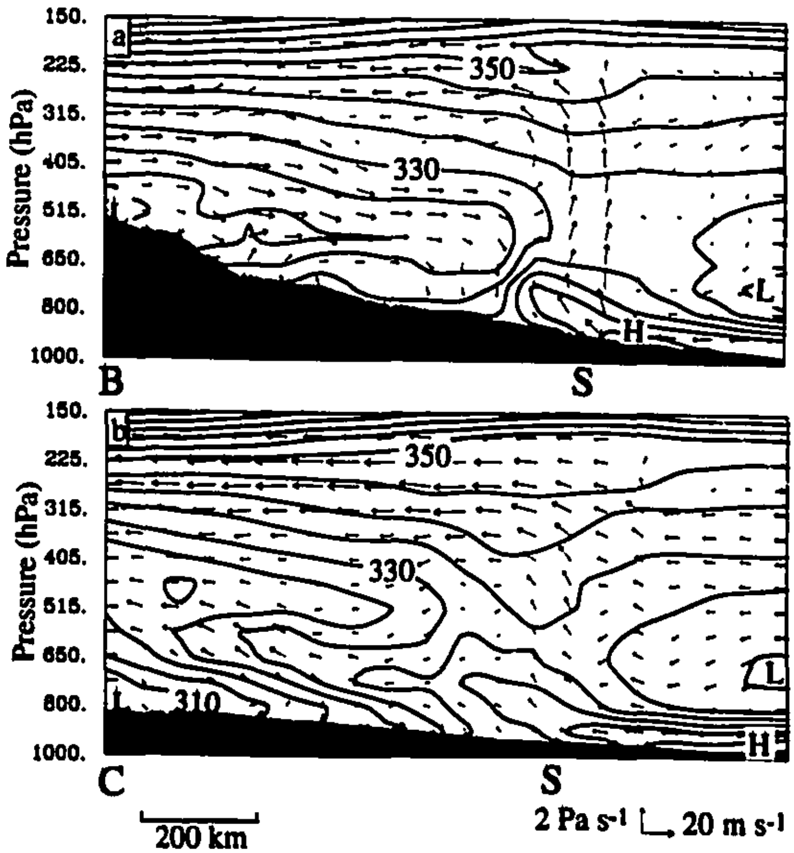

Fig. 6.12 Vertical cross sections of equivalent potential temperature (θe , every 5 K) with line-normal relative flow vectors from 12-h integration, which were taken along a) line B; and b) line C given in Fig. 6.4c. Letters, 'L' and 'H', show the respective minima and maxima of θ_e, and letter, 'S', indicates the position of the squall line.

about the mechanisms by which they are generated. Smull and Houze (1987) hypothesized that the rear inflow jet could be generated by the forward acceleration associated with a convectively-induced midlevel mesolow (on the meso-β-scale) in the stratiform region, and then by a hydrostatic pressure fall underneath warm convective updrafts (on the meso-γ-scale) in the leading convective region. Lafore and Moncrieff (1989) argued that the rear inflow jet may result from an RTF acceleration associated with a forward pressure-gradient force at the rear of the stratiform region (see also Weisman 1992). Schmidt and Cotton (1990) proposed that the rear inflow jet could be a result of the downward deflection and channeling of an ambient RTF flow by convectively generated divergent outflow at upper levels. It is possible that several of the above mechanisms may operate together. Zhang and Gao (1989) showed that an upper-level jet stream could provide a favorable RTF component to initiate the rear inflow, which is then accelerated forward by a midlevel mesolow and downward by cold downdrafts.

Now let us examine if any of the aforementioned mechanisms could account for the production of the rear inflow jet in the present case. First, the midlevel mesolow mechanism does not appear to be significant during the early stage, since it does not become evident until the mature stage. However, the strong RTF flow at upper levels suggests that the "blocking" mechanism may act at this stage, since the upper-level RTF flow could be slowed down and deflected downward by the divergent outflow as approaching the squall system (see Fig. 6.12a). To isolate the convective "blocking" effect from the large-scale circulations, a sensitivity experiment is conducted, in which neither convective nor grid-scale condensation were included (Exp. DRY), while keeping all other physical parameters identical to the control integration (Exp. CTL). Without the forcing from the diabatic heating, the model atmospheric circulations are only dominated by advective processes. Figure 6.13 compares the vertical circulations and relative flow normal to the line between Exps. DRY and CTL. Clearly, an RTF current with the scale and depth similar to those in Exp. CTL is also present in Exp. DRY. Of particular importance is that the basic flow structures between the two runs only differ at the upper and lower levels in association with the respective convectively-induced divergent outflow and cold descending flow. This indicates that the present rear inflow jet during the early stage does not result from any mesoscale processes, such as the "blocking" of an upper-level RTF ambient flow, or acceleration by a midlevel mesolow. Rather, a significant portion of the elevated rear inflow jet is a manifestation of the large-scale RTF flow component (see Fig. 6.13b).

Thus, it is evident that examination of the large-scale flow should help reveal why an RTF current occurs in the southern segment of the squall line but not in its northern part. Figure 6.14 shows that the squall line is actually embedded in a large-scale flow with a pronounced cyclonic circulation associated with the midlevel baroclinic trough and an anticyclonic circulation ahead (also see Fig. 6.3). It is apparent from this flow configuration that the presence of midlevel RTF flow depends on the location and orientation of a squall line with respect to the large-scale curved flow. In the present case, the RTF flow tends to be stronger in the southern portion of the squall system (i.e., near the base of the trough), whereas an intense FTR flow should be expected in the northern segment (i.e., near the interface between the cyclonic/anticyclonic circulations). It should be mentioned that because of the length scale and relative position of the squall line with respect to the large-scale cyclonic vorticity center, a midlevel mesovortex is not generated near the northern end of the squall line, which is presumably a preferred location for the development of mesovortices, according to Zhang (1992) and Skamarock et al. (1994).

b. The FTR ascending flows in the northern segment

As can be seen from Figs. 6.12b and 6.14, the shallow FTR ascending flow in the northern segment of the squall system results from the overrunning of the large-scale south-to-southeasterly flow along the cold frontal zone. Despite the presence of a deeper and stronger frontal forcing in this region, as indicated by strong gradients in moist isentropes, the grid-scale upward motion is very weak compared to that in the south (cf.

Figs. 6.12a,b). This appears to be mainly due to the lack of appreciable convergence associated with a rear inflow jet, since the prefrontal environment does not seem to differ considerably from that in the south (see Figs. 6.6 and 6.12). As a result, the upper-level warming and lower-level cooling, as shown for the southern segment in Fig. 6.10b, are weak, so is the convectively induced midlevel low-pressure zone (see Fig. 6.8). More significantly, these different circulation characteristics seem to account for the development of different weather conditions, namely, the well-organized, long-lived deep convection, and upper-level stratiform cloudiness in the south versus the shorter-lived deep convective activity and two possible layers (i.e., at middle and upper levels) of stratiform cloudiness in the north of the squall system. In particular, the northern stratiform precipitation appears to develop in a process different from the upper-level stratiform region that occurred in the southern squall system, although they both take place in FTR ascending flows.

According to Zhang and Cho (1992), the slantwise nature of the FTR ascending flow suggests that moist symmetric instability (MSI) may be operative in the development of the stratiform precipitation in the north. Thus, MPV could be used as a dynamical variable to diagnose the presence of MSI. It is defined as

$$MPV = \frac{1}{\rho}\left\{\frac{\partial \theta_e}{\partial n}\left(\frac{\partial w}{\partial s} - \frac{\partial v}{\partial z}\right) + \frac{\partial \theta_e}{\partial s}\left(\frac{\partial u}{\partial z} - \frac{\partial w}{\partial n}\right) + \frac{\partial \theta_e}{\partial z}\left(\frac{\partial v}{\partial n} - \frac{\partial u}{\partial s} + f\right)\right\} \tag{6.1}$$

where *n* and *s*, respectively, indicate the directions normal and parallel to the squall line. Two-dimensional theoretical studies show that MSI occurs in saturated regions with small or negative MPV (e.g., Bennetts and Hoskins 1979; Moore and Lambert 1993); this instability is conditional when the atmosphere is subsaturated. It is evident from Fig. 6.15 that both FTR ascending flows occur in nearly saturated layers with small or negative MPV: one in the upper troposphere, like that which occurred in the south, and the other above the frontal zone (cf. Fig. 6.12b and 6.15). This indicates the presence of moist symmetric instability in the two FTR flows, which occurs as a result of transporting the potentially unstable air from the prefrontal boundary layer into the sloping flow, where lifting to saturation occurs and the potential instability is released at the leading line (through parameterized convection). The transport of negative MPV in the deep FTR ascending flow is similar to that in the June 10-11 squall system (see Zhang and Cho 1992), whereas the negative MPV transport along the frontal zone resembles that described by Knight and Hobbs (1988) and Zhang and Cho (1995), except that there is a continuous supply of negative MPV in the present prefrontal boundary layer. Note that this transport process has caused the generation of weak potential instability above the frontal zone, mostly due to the increased moisture content. Although it is not possible to verify this phenomenon owing to the limited resolution of observations, it has been noticed in other midlatitude frontal precipitation cases (e.g., Herzegh and Hobbs 1981; Parsons and Hobbs 1983). These two layered cloudiness suggest that the precipitation in the lower-level clouds may involve "seeding" from above by ice particles (Cunningham 1951; Herzegh and Hobbs 1981).

c. Discussion

The above results clearly show that the large-scale circulations could play an important role in governing the squall's internal structures at different portions of the system, especially in the formation of low- to midlevel rear inflow and FTR flow. For a similar reason, the extent of upper-level FTR outflows would also depend on the orientation of a squall line with respect to a large-scale flow aloft and the intensity of the large-scale flow. The present finding of the large-scale control is significant, since previous studies have shown the important roles of elevated rear inflow jets and FTR ascending flow in determining the development and distribution of precipitation and surface phenomena within a squall system (see Thorpe et al. 1982; Rotunno et al. 1988; Weisman 1992; Davis and Weisman 1994). Specifically, the presence of an elevated and descending rear inflow jet appears to help increase mesoscale convergence or vertical motion (i.e., both updrafts and downdrafts), frequently leading to the concentration of cyclonic vorticity and to the development of surface wake lows and "gust" winds (Smull and Houze 1985, 1987;

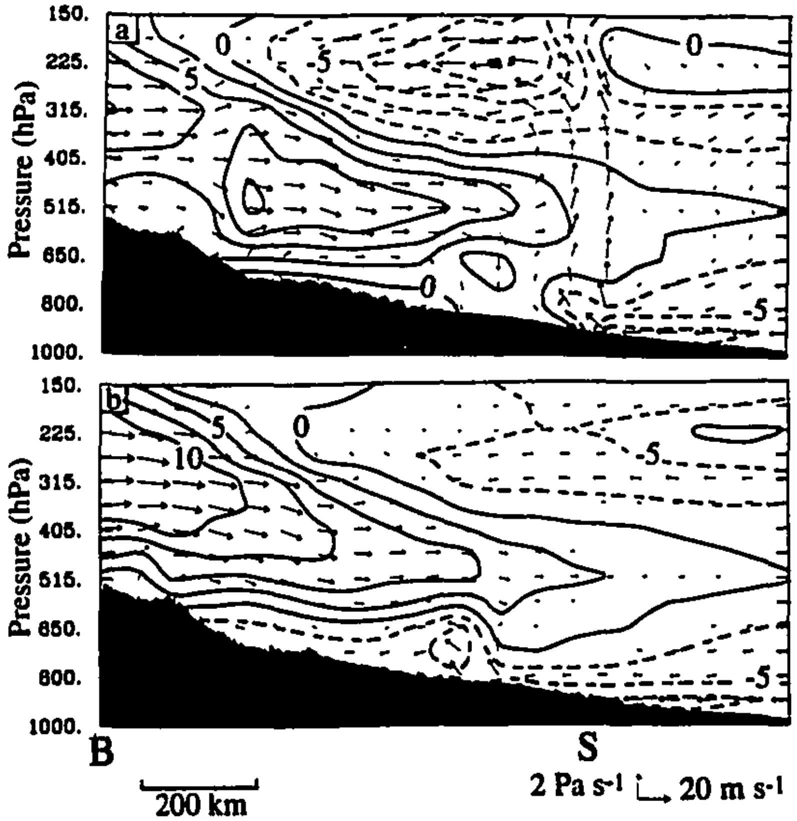

Fig. 6.13 Vertical cross sections of line-normal relative flow (every 2.5 m s^{-1}), superposed with the flow vectors, from 12-h integration of a) Exp. CTL; and b) Exp. DRY.

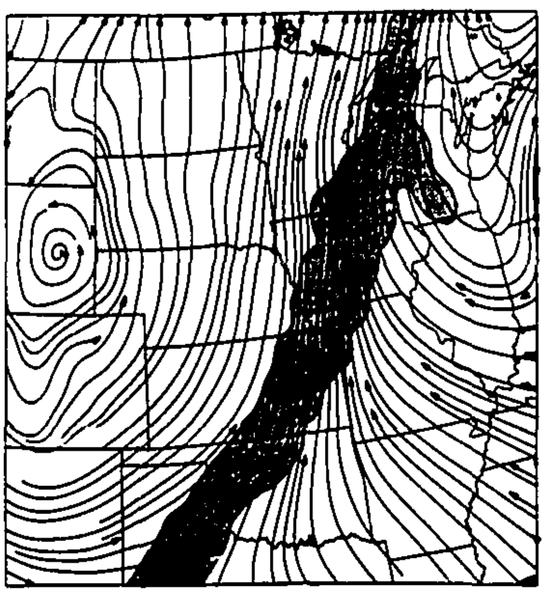

Fig. 6.14 Horizontal map of 500-hPa streamlines of relative flow, superposed with convective rainfall rates (shadings) with contours of 1 and 5 mm h^{-1} from 12-h integration.

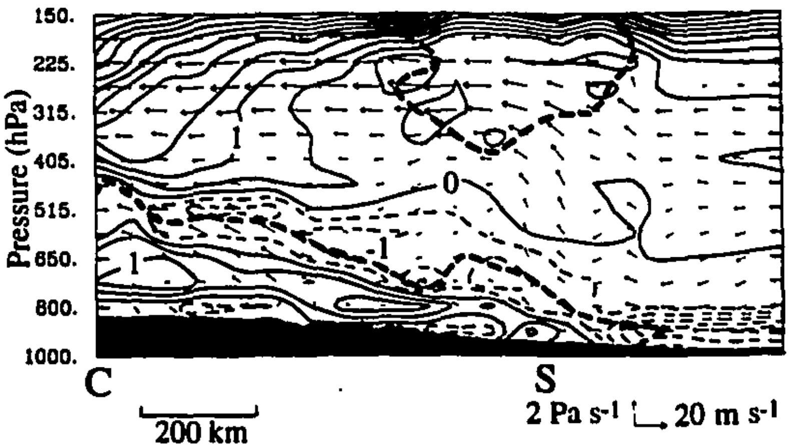

Fig. 6.15 As in Fig. 6.12b but for moist potential vorticity (every 0.5×10^{-6} m^2 K s^{-1} kg^{-1}). The thick dashed lines denote regions with relative humidity greater than 90 %.

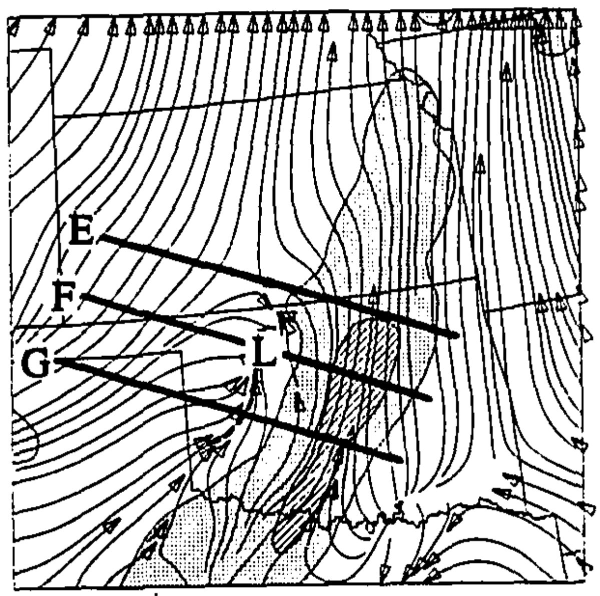

Fig. 6.16 Horizontal map of 500-hPa streamlines of relative flow from 18-h integration. Letter, 'L', indicates the position of the mesolow.

Johnson and Hamilton 1988; Rutledge et al. 1988), whereas the FTR ascending flow is often correlated with the formation of trailing stratiform precipitation (Zhang and Gao 1989; Biggerstaff and Houze 1991a). Therefore, if high-resolution operational models could predict reasonably well the development of squall lines with respect to tropospheric large-scale or short-wave disturbances, a significant improvement in quantitative precipitation forecasts and severe weather warnings could be achieved. In fact, a literature survey of observational studies reveals that an intense rear inflow jet occurs frequently in squall lines in coincidence with a favorable larger-scale circulation. For example, rear inflow jets have been observed near the base of deep mid- to upper-level troughs (e.g., Ogura and Liou 1980; Chang et al. 1981; Kessinger et al. 1987), midlevel short-wave troughs (e.g., Leary and Rappaport 1987; Johnson and Hamilton 1988), in easterly wave troughs (e.g., Zipser 1969; Houze 1977), and in regions of midlevel westerly flow (e.g., Fankhauser et al. 1992). It is interesting to note, however, that Rasmussen and Rutledge (1993) analyzed the development of a rear-inflow jet in a squall line without any larger-scale support. Although numerous modeling studies have shown the generation of rear inflow jets without explicit large-scale support (e.g., Lafore and Moncrieff 1989; Weisman 1992), the Rasmussen and Rutledge result appears to be attributable to their (Doppler) observational coverage that is too small to show the role of the larger-scale flow in the development of the rear inflow jet.

5. Along-line variability due to mesoscale circulation

As previously shown, there are two scales of circulations affecting the along-line variability of the present squall system: the baroclinically driven large-scale and the convectively generated mesoscale disturbances, particularly during the mature stage (see Fig. 6.8). [Note that the influence of convective (meso-γ)-scale processes could not be addressed herein due to the use of relatively coarse grid resolution and hydrostatic assumption.] Thus, in this section we focus only on the along-line variability of the squall's circulation due to the convectively-induced midlevel mesolow and upper-level mesohigh, although the large-scale flow always exerts an important influence on the structure and evolution of the squall system.

It is evident from Fig. 6.16 that corresponding to the midlevel mesolow, there is an elongated zone of confluence (or convergence) between the FTR and RTF flows that is superposed on the large-scale cyclonic flow in the trailing stratiform region. Moreover, streamlines exhibit greater curvatures in the vicinity of the mesolow, indicating the generation of three-dimensional meso-β-scale structures associated with the squall convection. To help gain insight into the relationship between the mesolow and the generation of the three-dimensional structures, horizontal momentum budgets at 500 hPa are calculated with the following Lagrangian momentum equation

$$\frac{d\vec{v}'}{dt} = - f\vec{k} \times \vec{v}' - \left(\vec{\nabla}\phi + f\vec{k} \times \vec{c}\right) \qquad (6.2)$$

where $\vec{v}'$ is the horizontal wind vector relative to the squall line, f is the Coriolis parameter, $\vec{k}$ is the unit vector in the vertical direction, ϕ is the geopotential height, and $\vec{c}$ is the propagation vector of the squall line. Eq. (6.2) represents a horizontal force balance among the inertial acceleration, the Coriolis force and the pressure gradient force (PGF) in the framework relative to the squall line. Note that the term, $f\vec{k} \times \vec{c}$, has been included in the PGF calculation because of the use of the system-relative framework. Note also that the effect of numerical diffusion has been neglected in Eq. (6.2).

Figure 6.17 presents a 500-hPa map of geopotential heights and a few system-relative streamlines taken from Fig. 6.16, superposed with force-balance diagrams at some selected points in the vicinity of the squall line. The basic flow patterns at 500 hPa resemble those at 700 hPa (cf. Figs. 6.8b and 6.17), except that the convectively generated mesohigh becomes more evident at higher levels (see Fig. 6.10a). One can see that air parcels far behind the squall line (e.g., at points 1 - 3) are influenced little by the convectively-induced pressure perturbations; they are almost in a geostrophically-balanced state with the large-scale trough. However, the situation is quite different for air parcels closer to the mesolow. Specifically, these parcels are forced by PGF to accelerate into the low-pressure zone, while the Coriolis force tends to deflect them rightward (e.g., at points 4 - 9). The rightward deflection is greater if the large-scale background flow is stronger. The net result is that the parcels in the large-scale RTF southwesterly (FTR southerly) flow are accelerated toward the south (north) of PGF vectors, rather than along the vectors, leading to the confluence of streamlines along the mesotrough axis (cf. Figs. 6.16 and 6.17). Thus, a more intense RTF (FTR) flow should be expected slightly to the south (north) of the mesolow. This reveals that the mesolow mechanism, proposed by Smull and Houze (1987), is indeed operative during the mature stage, but the mechanism needs to include the deflectional effect of the Coriolis force.

To further examine the along-line variability of the squall system due to the convectively generated perturbations, Fig. 6.18 compares the relative flow and PGF normal to the line between three different cross sections around the midlevel mesolow. In general, the magnitude of PGF and the depth of convectively generated disturbances are greater toward the south. As can be expected, most of the FTR and RTF accelerations occur in the positive and negative PGF regions, respectively; the larger the PGF is, the greater is the FTR and RTF acceleration. This is particularly true for the cross section through the center of the mesolow (Fig. 6.18b). This result is consistent with the numerical momentum budget by Gao et al. (1990), who showed that PGF provides important contributions to the acceleration of both FTR and RTF flows. However, the RTF flow in the southern cross section is stronger than that in the middle one (cf. Figs. 6.18b,c), in spite of the presence of smaller PGF values in the region. As demonstrated in the force-balance diagrams in Fig. 6.17, this is due partly to the deflection of the rear inflow and partly to the existence of large-scale support. On the other hand, it is not surprising that the elevated RTF flow is much weaker to the north of the midlevel mesolow (see Fig. 6.18a), as has also been found by Zhang and Gao (1989).

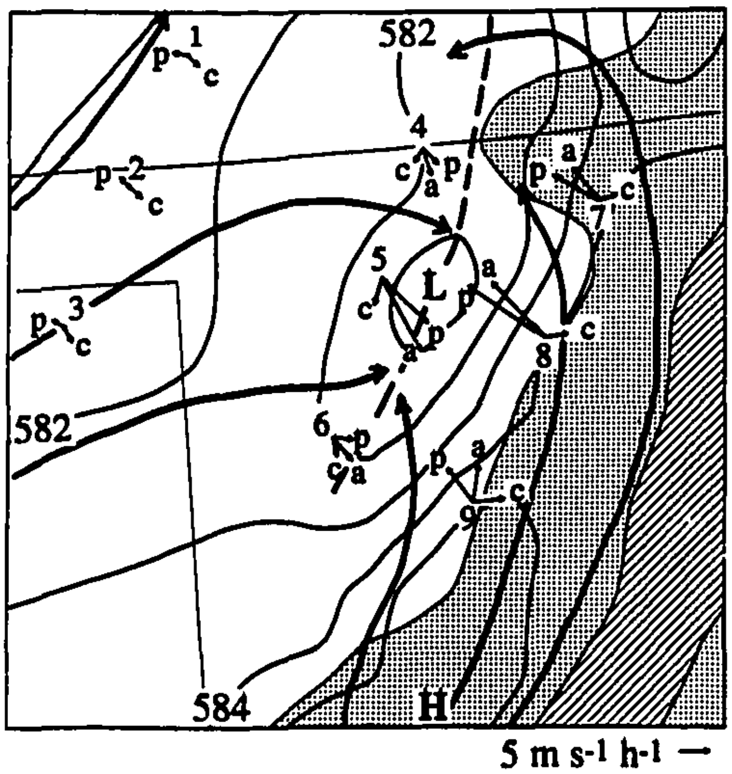

Fig. 6.17 Horizontal map of 500-hPa heights (solid, every 1 dam) superposed with streamlines of relative flow (thick solid lines) from 18-h integration. Force balances at a few selected points are depicted, with the letters, 'c', 'p' and 'a', denoting the Coriolis (i.e., $-f\vec{k}\times\vec{v}'$), pressure gradient force (i.e., $-\vec{\nabla}\phi - f\vec{k}\times\vec{c}$), and Lagrangian accelerations (i.e., $d\vec{v}'/dt$), respectively. Shadings represents the convective rainfall rates with contours of 1 and 5 mm h^{-1}. Dashed lines indicate the orientation of the mesoscale trough.

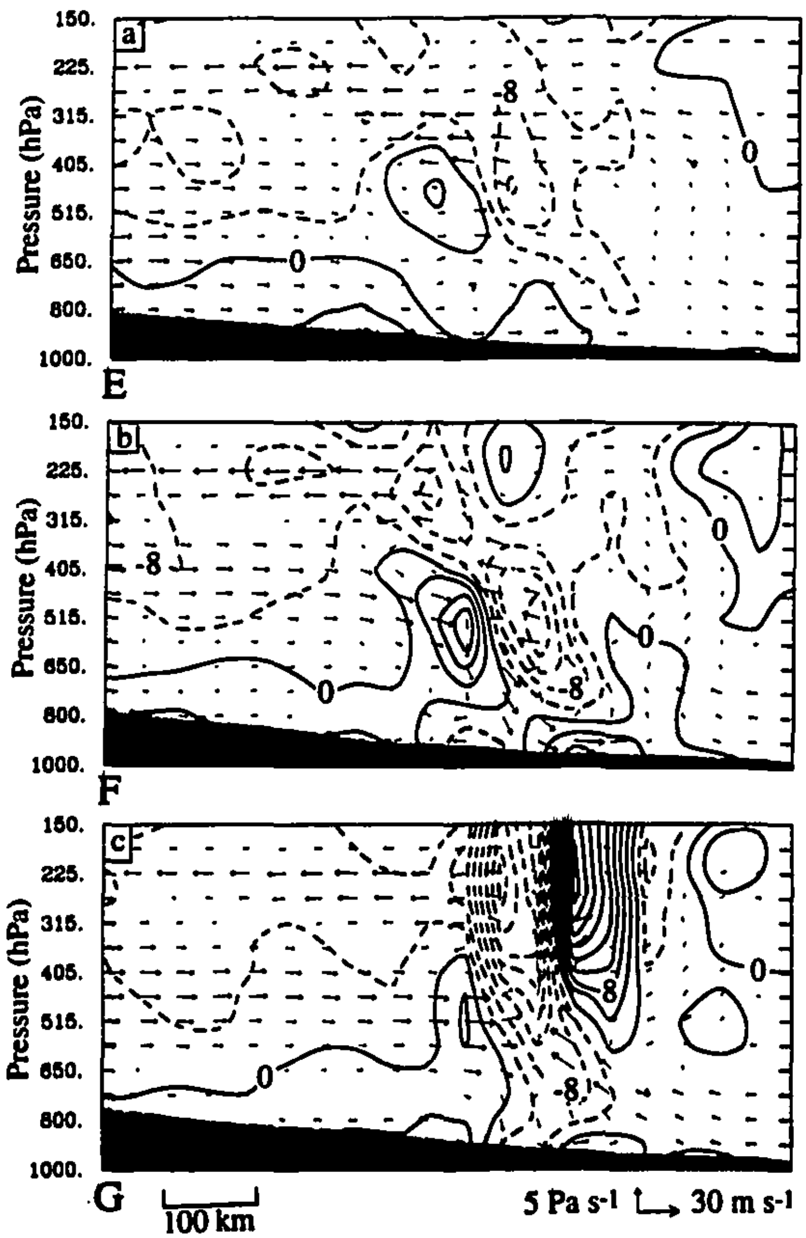

Fig. 6.18 As in Fig. 6.7 but for pressure gradient forces normal to the line (every 4 m s^{-1} h^{-1}) along a) line E; b) line F; and c) line G given in Fig. 6.16.

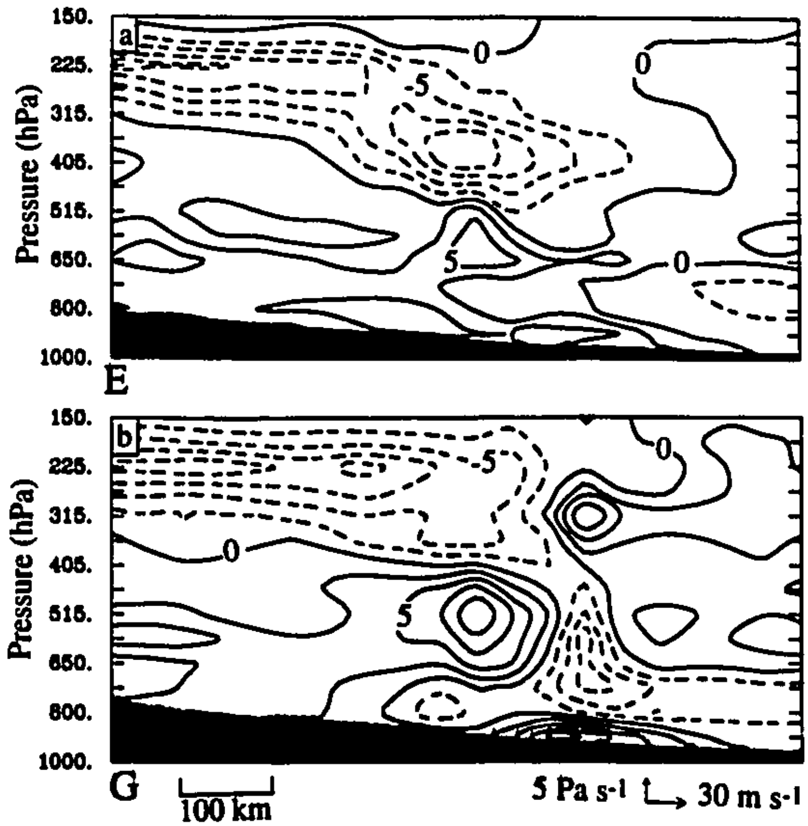

Fig. 6.19 Vertical cross sections of the horizontal flow differences (every 2.5 m s^{-1}) normal to the line between Exps. CTL and DRY (i.e., CTL - DRY) that are taken along a) line E; and b) line G given in Fig. 6.16, from 18-h integration.

While the mesolow mechanism is operative during the mature stage, it is unclear how significant it is, as compared to the large-scale support. Thus, the net (i.e., direct and indirect) effect of the squall convection needs be isolated from that associated with the large-scale circulation by subtracting the line-normal flows in Exp. DRY from those in Exp. CTL. It is evident from Figs. 6.19a,b that when coupled with vertical motion, the squall convection could induce, without any large-scale support (e.g., Lafore and Moncrieff 1989; Weisman 1992), the typical two-dimensional flow structures, such as the overturning ascending flow at the front, an FTR penetrative flow into the upper-level trailing stratiform region and an RTF flow down to the surface. However, the scale of the convectively generated RTF flow component (~ 200 km) is much shorter than that associated with the large-scale flow (cf. Figs. 6.13 and 6.19). This provides further evidence on the scale interaction involved in the development of rear inflow jets as found by Zhang and Gao (1989). It is also evident that both the convectively generated FTR and RTF flows in the southern cross section are stronger than those in the north, due to the presence of more intense PGF associated with the mesohigh and mesolow. In addition, the differenced FTR flow becomes more slantwisely distributed and the upper portion of the overturning flow diminishes as the cross section is shifted northward (Fig. 6.19a). This is because the large-scale flow tends to govern the two-dimensional structure of the squall system to the north, as previously mentioned.

6. Summary and conclusions

In this study, an improved research version of the RFE model has been used to investigate the along-line variability of vertical circulation structures of a frontal squall line that occurred during 26-27 June 1985 PRE-STORM. This version of the RFE model is similar to that used operationally at CMC except for the use of a high-resolution grid length and different treatments of subgrid and grid-scale condensation. It is shown that the model reproduces reasonably well a number of basic surface features and tropospheric flow structures, as verified against available network observations. These include the initiation, propagation and disintegration of the squall system, surface pressure perturbations and cold outflow boundaries, a midlevel mesolow and an upper-level mesohigh, an FTR ascending flow overlying an intense RTF flow, and a leading convective line followed by stratiform precipitation regions.

It is found that the vertical circulations at the northern segment of the squall line differ substantially from those at its southern segment. In particular, the classical squall-line structures that appeared in the southern segment do not develop in the northern portion of the squall system, such as the rear inflow jet, the midlevel mesolow and surface pressure and temperature perturbations. Instead, there are two FTR flows that are bifurcated at the leading squall front: one transports the boundary layer high-θ_e air into the upper levels and the other along the frontal zone into the midtroposphere. This appears to help generate trailing stratiform clouds in the lower and upper tropospheres.

To investigate the scale interaction involved in the development of the along-line variability, a scale separation technique is applied to the control integration and a comparison with a "dry" simulation is conducted, in which all moist convective processes are turned off. Both the scale analysis and the comparison between the control and "dry" integrations reveal that the along-line variability of the system's internal circulations results primarily from the interaction of convectively generated pressure perturbations with a midlevel baroclinic trough, as depicted in the conceptual model shown in Fig. 6.20. This conceptual model shows that the squall's vertical circulation structures depend on the location and orientation of the squall line with respect to the large-scale trough and the mesoscale disturbances. Specifically, the large-scale trough provides an extensive RTF flow component near its base (i.e., in the southern segment), and a favorable FTR flow component in the northern portion of the squall system (see Fig. 6.20a). This large-scale contribution to the along-line variability is especially significant during the system's formative stage. In contrast, convectively-induced mesoscale disturbances tend to determine the internal circulations of the squall system in the south during the system's mature to dissipating stages (see Fig. 6.20b). In particular, the midlevel mesolow and upper-level mesohigh help accelerate the rear inflow jet and the divergent FTR outflow in the trailing stratiform region. It has been demonstrated through force-balance diagrams that the rear inflow jet tends to be more intense to the south of the mesolow, rather than near the center of the mesolow, due to the deflectional effect of the Coriolis force. This enhanced RTF flow increases the convergence and upward motion in the low-to-mid troposphere, thus leading to the development of more intense and longer-lived convective system in the southern segment of the squall system.

In conclusion, we may state that the vertical circulation characteristics at different parts of a midlatitude squall line are dependent on the interaction of convectively generated mesoscale disturbances (e.g., mesolows and mesohighs) with large-scale circulations (e.g., baroclinic troughs, easterly waves and jet streams). The classical two-dimensional structures may only develop at certain, but not all, portions of midlatitude squall lines. In particular, the rear inflow component, that is often correlated with organized convective development, vorticity concentration and trailing stratiform precipitation, tends to be more intense to the south of a midlevel mesolow and near the base of a large-scale trough. In other cases, the rear inflow and upper-level FTR outflow may not develop, depending upon the distribution and orientation of the squall line with respect to its larger-scale flow and the intensity of the large-scale flow. Although the above conclusions are only drawn from a single squall-line study, they are more or less supported by previous studies of midlatitude squall lines. Hence, these results have important implications as to the improvement of warm-season quantitative precipitation forecasts and severe weather warnings by operational numerical weather prediction models, like the one used for the present study, since more intense meso-β-scale circulations in these MCSs are associated with meso-α or larger-scale disturbances.

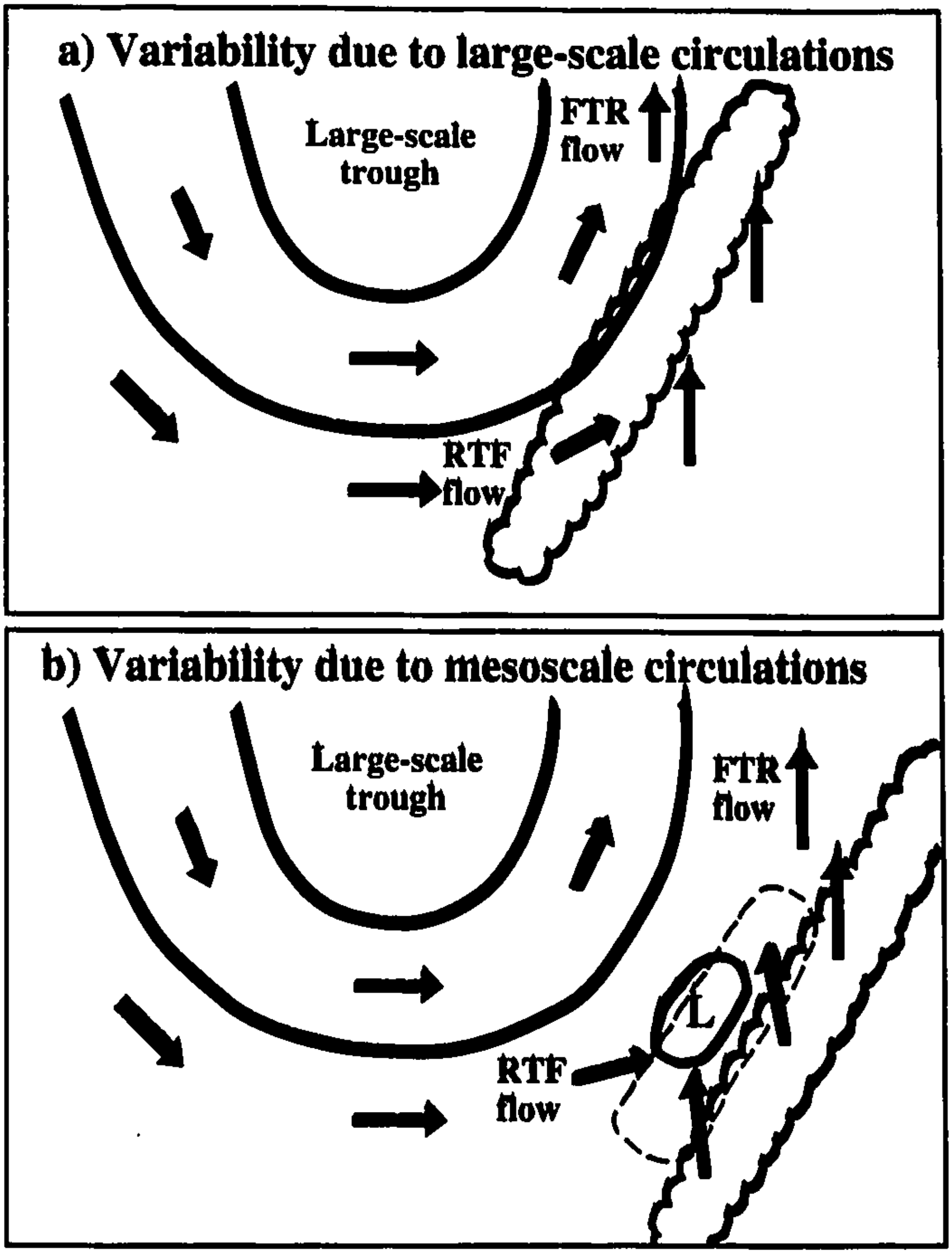

Fig. 6.20 Schematic representation of the influences of a) large-scale and b) mesoscale circulations on the internal flow structure of the squall line. The midlevel geopotential heights (thick solid lines) and relative flow vectors are shown. The location of the squall line (thick cloud line) and the trailing stratiform region (thin dashed line) are also indicated. Letter, 'L', shows the position of the midlevel mesolow.

Chapter 7

Summary, conclusions, and recommendations

7.1 Summary and conclusions

In this thesis, a research version of the Canadian RFE model is used to investigate the internal structures and evolution of midlatitude squall lines. As a first part of this project, the FC convective scheme and the explicit moisture scheme containing cloud water (ice) and rainwater (snow) are incorporated into the model. The capability of this improved model in predicting the development of midlatidude squall lines is tested with a well-documented case that occurred during 10-11 June 1985 over the PRE-STORM observational network. Then, the model is used as a tool to examine the meso-β-scale structure and evolution of two other squall lines, namely, the one that was associated with the 14 July 1987 Montreal flood, and the other that occurred during 26-27 June 1985 PRE-STORM. The main results are summarized as follows.

This study demonstrates that the improvement in the operational quantitative precipitation forecasts and severe weather warnings is possible if realistic model physics, reasonable initial conditions, and high resolution are used. It is found that although the use of high horizontal resolution helps improve the timing and location of the convective development, appropriate physics representations must be incorporated in order to reproduce various types of meso-β-scale circulations and their associated precipitation. These include parameterized moist downdrafts, explicit representation of cloud water (ice) and rainwater (snow), hydrostatic water loading, and boundary-layer parameterization. In the first squall-line case, when the FC convective scheme and the explicit moisture scheme are simultaneously used, the model reproduces remarkably well the main features of the 10-11 June 1985 PRE-STORM squall line, such as precipitation patterns, surface mesohighs and mesolows, FTR ascending and RTF descending flows, and a cooling-induced midlevel mesovortex. In contrast, the model fails to reproduce these features when either the Kuo or moist convective adjustment (MCA) schemes were utilized. Furthermore, it is found that the MCA scheme tends to delay the initiation of the deep convection, whereas the Kuo scheme removes too much moisture from the boundary layer, thereby leading to an underestimation of the grid-scale precipitation. It is also shown that poor resolution of mesoscale structures in the initial conditions could alter the prediction of the structure and evolution of MCSs. In the present case, the use of a low-resolution analysis leads to the development of a "cyclone-like" circulation in association with the squall line. This case verification provides a basis to use the RFE model to study the internal structures and evolution of other squall lines or MCSs.

A second case of the squall line that occurred in association with the 14 July 1987 Montreal flood, is simulated to study the role of gravity waves in the development of the prefrontal squall line. It is found that early convective activity is responsible for the triggering of the gravity waves. These waves propagate over a long distance in a "phase-locked" manner with deep convection, allowing the positive feedback between the convective heating/cooling and wave forcing to occur - a wave-CISK mechanism. Thus, the continued convective heating/cooling tends to enhance the gravity waves, while the gravity waves assist the organization of deep convection into a line structure. An important finding of this case simulation is that the realistic prediction of the wave-convection interactions depends on the use of an adequate convective parameterization. When the Kuo convective scheme is used, the model triggers moist convection over a mesotrough and fails to amplify a train of gravity waves interacting with deep convection during the mature stage of the system. In contrast, the model with the FC scheme reproduces convective activity over the wave ridge due to the effects of parameterized moist downdrafts, which is in agreement with the conceptual model of gravity waves.

A trailing stratiform rainband associated with the 14 July squall system is also investigated. It is found that the rainband is dynamically forced by frontogenetical processes, and aided by the release of conditional symmetric instability (CSI) and local orographical lifting. The internal flow structure of the system is determined by the release of latent heating in environments with different potential stability. It is found that the parameterized and explicit cloud schemes account for the formation of the leading convective line and trailing stratiform rainband, respectively. One of the roles of the leading convection is to remove most of the potential instability, and thus limit the development of the trailing stratiform precipitation.

Finally, the along-line variability of squall lines is investigated using the numerical prediction of a third squall-line case that occurred during 26-27 June 1985 over the PRE-STORM network. It is shown that the three-dimensionality of the internal flows of the squall line results from both large-scale and convectively-induced mesoscale circulations. The vertical circulation structures of the system are determined by the location of the squall line with respect to a midlevel baroclinic wave trough. This wave provides an intense midlevel RTF flow in the southern segment of the squall line and an FTR flow to the north. It is shown that the along-line variability of the squall line at the formative stage is mainly caused by the large-scale circulation. However, the situation is quite different at the mature stages, when only the southern portion of the system remains intense and well organized. This intense squall line is found to generate pressure perturbations superposed on the large-scale flow, leading to the development of meso-β-scale variability. It is shown that the rear inflow jet is enhanced in the trailing stratiform region, particularly to the south of the midlevel mesolow and near the base of the trough. This rear inflow jet increases the midlevel convergence and stratiform precipitation.

7.2 Recommendations

While the results of the present study are encouraging for the advent of operational prediction of meso-β-scale structures and evolution of MCSs, more work is needed to improve the operational forecast of our daily weather. In particular, the following research is highly recommended.

a) The improved version of the RFE model should be used to simulate other types of summertime severe weather events, such as MCCs. However, the prediction of these systems is an even more challenging task, since they normally occur in environments with weaker large-scale forcing, in contrast to squall-line systems. The use of more realistic initial conditions that better resolve mesoscale flows, such as low-level jets, moisture tongues, and outflow boundaries, and more reasonable model physics, such as the boundary-layer parameterization and convective triggering functions, could be the key elements to obtain successful prediction of these systems (see Stensrud and Fritsch 1994a,b; Zheng et al. 1994).

b) The improved version of the RFE model should also be tested with other types of weather systems, such as polar lows, coastal storms, tropical cyclones, etc. Work along this line is currently under way at the Montreal mesoscale community.

c) The coupling between the FC and explicit moisture schemes could be improved by allowing the implicit scheme to detrain cloud water (ice) and rainwater (snow) to the grid scale, as proposed by Molinari and Dudek (1992) and Zhang et al. (1994). Furthermore, the coupling between the model clouds and radiative processes could be improved due to the introduction of the explicit moisture scheme into the RFE model.

d) The FC convective scheme could be improved by incorporating a reasonable treatment of subgrid-scale momentum transport. It has been shown that momentum transport by meso-β-scale flows could have an important effect on the organization and evolution of squall lines, due to countergradient flow transport normal to the line and downgradient transport along the line.

REFERENCES

Anthes, R.A., 1985: Parameterization of moist convective effects on the thermodynamic and moisture fields in numerical models. *ECMWF Seminar, Phys. Param. Numer. Models Atmos.*, **1**, 121-147.

——, Y.-H. Kuo, E.-Y. Hsie, S. Low-Nam, and T.W. Bettge, 1989: Estimation of skill and uncertainty in regional numerical models. *Quart. J. Roy. Meteor. Soc.*, **115**, 763-806.

Arakawa, A., W.H. Schubert, 1974: Interaction of a cumulus cloud ensemble with the large-scale environment, part I. *J. Atmos. Sci.*, **31**, 674-701.

Augustine, J.A., and K.W. Howard, 1991: Mesoscale convective complexes over the United States during 1986 and 1987. *Mon. Wea. Rev.*, **119**, 1575-1589.

Balachandran, N.K., 1980: Gravity waves from thunderstorms. *Mon. Wea. Rev.*, **108**, 804-816.

Bartels, D. and R.A. Maddox, 1991: Midlevel cyclonic vortices generated by mesoscale convective systems. *Mon. Wea. Rev.*, **119**, 104-118.

Bélair, S., D.-L. Zhang, and J. Mailhot, 1994: Numerical prediction of the 10-11 June 1985 squall line with the Canadian regional finite-element model. *Wea. Forecasting*, 9, 157-172.

——, ——, and ——, 1995a: Numerical prediction of an intense convective system associated with the July 1987 Montreal flood. Part II: A trailing stratiform rainband. Accepted by *Atmos.-Ocean.*

——, ——, and ——, 1995b: Numerical prediction of an intense convective system associated with the July 1987 Montreal flood. Part I: Gravity waves and the squall line. Accepted by *Atmos.-Ocean.*.

Bellon, A., M. Duncan, and G.L. Austin, 1993: A non-isotropic gauge interpolation scheme applied to the Montreal rainstorm of 14 July 1987. *Atmos-Ocean*, **31**, 27-56.

Bennetts, D.A., and B.J. Hoskins, 1979: Conditional symmetric instability - A possible explanation for frontal rainbands. *Quart. J. Roy. Meteor. Soc.*, **105**, 945-962.

Benoit, R., J. Côté, and J. Mailhot, 1989: Inclusion of a TKE boundary layer parameterization in the Canadian regional finite-element model. *Mon. Wea. Rev.*, **117**, 1726-1750.

Biggerstaff, M.I., and R.A. Houze, 1991a: Kinematic and precipitation structure of the 10-11 June 1985 squall line. *Mon. Wea. Rev.*, **119**, 3034-3065.

——, and ——, 1991b: Midlevel vorticity structure of the 10-11 June 1985 squall line. *Mon. Wea. Rev.*, **119**, 3066-3079.

Bluestein, H.B., and M.H. Jain, 1985: Formation of mesoscale lines of precipitation: Severe squall lines in Oklahoma during the spring. *J. Atmos. Sci.*, **42**, 1711-1732.

Bosart, L.F., and J.P. Cussen, 1973: Gravity wave phenomena accompanying east coast cyclogenesis. *Mon. Wea. Rev.*, **101**, 446-454.

——, and F. Sanders, 1986: Mesoscale structure in the megalopolitan snowstorm of 11-12 February 1983. Part III: A large-amplitude gravity wave. *J. Atmos. Sci.*, **43**, 924-939.

——, and A. Seimon, 1988: A case study of an unusually intense atmospheric gravity wave. *Mon. Wea. Rev.*, **116**, 1857-1886.

Brandes, E.A., 1990: Evolution and structure of the 6-7 May 1985 mesoscale convective system and associated vortex. *Mon. Wea. Rev.*, **118**, 109-127.

Browning, K.A., and T.W. Harrold, 1969: Air motion and precipitation growth in a wave depression. *Quart. J. Roy. Meteor. Soc.*, **95**, 288-309.

Carbone, R.E., J.W. Conway, N.A. Crook, and M.W. Moncrieff, 1990: The generation and propagation of a nocturnal squall line. Part I: Observations and implications for mesoscale predictability. *Mon. Wea. Rev.*, **118**, 26-49.

Chang, C.B., D.J. Perkey and C.W. Kreitzberg, 1981: A numerical case study of the squall line of 6 May 1975. *J. Atmos. Sci.*, **38**, 1601-1615.

Charba, J.P., and W.H. Klein, 1980: Skill in precipitation forecasting in the national weather service. *Bull. Amer. Meteor. Soc.*, **61**, 1546-1555.

Churchill, D.D., and R.A. Houze, 1984: Development and structure of winter monsoon cloud clusters on 10 December 1978. *J. Atmos. Sci.*, **41**, 933-960.

Cotton, W.R., and R.A. Anthes, 1989: *Storm and Cloud Dynamics*. Academic Press, 883 pp.

——, M.-S. Lin, R.L. McAnelly, and C.J. Tremback, 1989: A composite model of mesoscale convective complexes. *Mon. Wea. Rev.*, **117**, 765-783.

Cram, J.M., R.A. Pielke, and W.R. Cotton, 1992a: Numerical simulation and analysis of a prefrontal squall line. Part II: Propagation of the squall line as an internal gravity wave. *J. Atmos. Sci.*, **49**, 209-225.

——, ——, and ——, 1992b: Numerical simulation and analysis of a prefrontal squall line. Part I: Observations and basic simulation results. *J. Atmos. Sci.*, **49**, 189-208.

Crook, N.A., 1988: Trapping of low-level internal gravity waves. *J. Atmos. Sci.*, **45**, 1533-1541.

Cunning, J.B., 1986: The Oklahoma-Kansas preliminary regional experiment for STORM-Central. *Bull. Amer. Meteor. Soc.*, **67**, 1478-1486.

Cunningham, R.M., 1951: Some observations of natural precipitation processes. *Bull. Amer. Meteor. Soc.*, **32**, 334-343.

Daley, R., C. Girard, J. Henderson, and I. Simmons, 1976: Short-term forecasting with a multi-level spectral primitive equation model. *Atmosphere*, **14**, 98-116.

Davies, H.C., 1979: Phase-lagged wave-CISK. *Quart. J. Roy. Meteor. Soc.*, **105**, 325-353.

Davis, C.A. and M.L. Weisman, 1994: Balanced dynamics of mesoscale vortices produced in simulated convective systems. *J. Atmos. Sci.*, **51**, 2005-2030.

Deardorff, J.W., 1979: Efficient prediction of ground surface temperature and moisture with inclusion of a layer vegetation. *J. Geophys. Res.*, **83**, 1889-1903.

Delage, Y., 1979: Parameterization of clouds, precipitation and radiation for forecast models. Notes scientifiques et techniques, **7**, RPN.

Dudhia, J., 1989: Numerical study of convection observed during the winter monsoon experiment using a mesoscale two-dimensional model. *J. Atmos. Sci.*, **46**, 3077-3107.

Einaudi, F., W.L. Clark, D. Fua, J.L. Green, and T.E. VanZandt, 1987: Gravity waves and convection in Colorado during July 1985. *J. Atmos. Sci.*, **44**, 1534-1553.

Emanuel, K.A., 1979: Inertial instability and mesoscale convective systems. Part I: Linnear theory of inertial instability in rotating viscous fluid. *J. Atmos. Sci.*, **36**, 2425-2449.

——, 1985: Frontal circulations in the presence of small moist symmetric stability. *J. Atmos. Sci.*, **42**, 1062-1071.

——, M. Fantini, and A.J. Thorpe, 1987: Baroclinic instability in an environment of small stability to slantwise moist convection. Part I: Two-dimensional models. *J. Atmos. Sci.*, **44**, 1559-1573.

Eom, J.K., 1975: Analysis of the internal gravity wave occurrence of 19 April 1970 in the Midwest. *Mon. Wea. Rev.*, **103**, 217-226.

Fankhauser, J.C., G.M. Barnes, and M.A. LeMone, 1992: Structure of a midlatidude squall line formed in strong unidirectional shear. *Mon. Wea. Rev.*, **120**, 237-260.

Ferguson, H.L., 1967: Mathematical and synoptic aspects of a small-scale wave disturbance over the lower Great Lakes area. *J. Appl. Meteor.*, **6**, 523-529.

Fouquart, Y., and B. Bonnel, 1980: Computations of solar heating of the earth's atmosphere: A new parameterization. *Contrib. Atmos. Phys.*, **53**, 35-62.

Frank, W.M., 1983: The cumulus parameterization problem. *Mon. Wea. Rev.*, **111**, 1859-1871.

Fritsch, J.M., and C.F. Chappell, 1980: Numerical prediction of convectively driven mesoscale pressure systems. Part I: Convective parameterization. *J. Atmos. Sci.*, **37**, 1722-1733.

——, and R.A. Maddox, 1981a: Convectively driven mesoscale weather systems aloft. Part I: Observations. *J. Appl. Meteor.*, **20**, 9-19.

——, and ——, 1981b: Convectively driven mesoscale weather systems aloft. Part II: Numerical simulations. *J. Appl. Meteor.*, **20**, 20-26.

——, and J.M. Brown, 1982: On the generation of convectively driven mesohighs aloft. *Mon. Wea. Rev.*, **110**, 1554-1563.

——, R.J. Kane, and C.R. Chelius, 1986: The contribution of mesoscale convective weather systems to the warm-season precipitation in the United States. *J. Climate Appl. Meteor.*, **25**, 1333-1345.

——, and K.F. Heideman, 1989: Some characteristics of the limited-area fine-mesh (LFM) model quantitative precipitation forecasts (QPF) during the 1982 and 1983 warm seasons. *Wea. Forecasting*, **4**, 173-185.

Fujita, T., 1959: Precipitation and cold air production in mesoscale thunderstorm systems. *J. Meteor.*, **16**, 454-466.

Gallus, W.A., and R.H. Johnson, 1991: Heat and moisture budgets of an intense midlatitude squall line. *J. Atmos. Sci.*, **48**, 122-146.

——, and ——, 1992: The momentum budget of an intense midlatitude squall line. *J. Atmos. Sci.*, **49**, 422-450.

Gao, K., D.-L. Zhang, M.W. Moncrieff and H.-R. Cho, 1990: Mesoscale momentum budget in a midlatitude squall line: A numerical case study. *Mon. Wea. Rev.*, **118**, 1011-1028.

Garand, L., 1983: Some improvements and complements to the infrared emissivity algorithm including a parameterization of the absorption in the continuum region. *J. Atmos. Sci.*, **40**, 230-244.

Gossard, E.E., and W.H. Hooke, 1975: Waves in the Atmosphere. Developments in Atmosphere Science. *Elsevier Scientific Publishing Co., Amsterdam*, 456 pp.

Grell, G.A., 1993: Prognostic evaluation of assumptions used by cumulus parameterizations. *Mon. Wea. Rev.*, **121**, 764-787.

Gyakum, J.R., 1986: Experiments in temperature and precipitation forecasting for Illinois. *Wea. and Forecasting*, **1**, 77-88.

Haltiner, G., and R. Williams, 1980: *Numerical Weather Prediction and Dynamic.* Wiley, 477 pp.

Heideman, K.F., and J.M. Fritsch, 1988: Forcing mechanisms and other characteristics of significant summertime precipitation. *Wea. and Forecasting*, **3**, 115-130.

Herzegh, P.H. and P.V. Hobbs, 1981: The mesoscale and microscale structure and organization of clouds and precipitation in midlatitude cyclones. IV: Vertical air motions and microphysical structures of prefrontal surge clouds and cold frontal clouds. *J. Atmos. Sci.*, **38**, 1771-1784.

Hobbs, P.V., 1978: Organization and structure of clouds and precipitation on the mesoscale and microscale in cyclonic stroms. *Rev. Geophys. Space Phys.*, **16**, 741-755.

——, J.D. Locatelli and J.E. Martin, 1990: Cold fronts aloft and the forecasting of precipitation and severe weather east of the Rocky Mountains. *Wea. Forecasting*, **5**, 613-626.

Houze, R.A., 1977: Structure and dynamics of a tropical squall line system. *Mon. Wea. Rev.*, **105**, 1540-1567.

——, and P.V. Hobbs, 1982: Organization and structure of precipitating cloud systems. *Adv. Geophys.*, **24**, 225-315.

——, S.A. Rutledge, M.I. Biggerstaff, and B.F. Smull, 1989: Interpretation of Doppler weather radar displays of midlatitude mesoscale convective systems. *Bull. Amer. Meteor. Soc.*, **70**, 608-619.

Hoxit, L.R., C.F. Chappell, and J.M. Fritsch, 1976: Formation of mesolows of pressure troughs in advance of cumulonimbus clouds. *Mon. Wea. Rev.*, **104**, 1419-1428.

Hsie, E.-Y., R.A. Anthes, and D. Keyser, 1984: Numerical simulation of frontogenesis in a moist atmosphere. *J. Atmos. Sci.*, **41**, 2581-2594.

Johnson, R.H., and P.J. Hamilton, 1988: The relationship of surface pressure features to the precipitation and airflow structure of an intense midlatitude squall line. *Mon. Wea. Rev.*, **116**, 1444-1472.

——, S. Chen, and J.J. Toth, 1989: Circulations associated with a mature-to-decaying midlatitude mesoscale convective system. Part I: Surface features - Heat bursts and mesolow development. *Mon. Wea. Rev.*, **117**, 942-959.

——, and D.L. Bartels, 1992: Circulations associated with a mature-to-decaying midlatitude mesoscale convective system. Part II: Upper-level features. *Mon. Wea. Rev.*, **120**, 1301-1320.

Kessinger, C.J., P.S. Ray and C.E. Hane 1987: The Oklahoma squall line of 19 May 1977. Part I: A multiple Doppler analysis of convective and stratiform region. *J. Atmos. Sci.*, **44**, 2840-2864.

Kessler, E., 1969: On the distribution and continuity of water substance in atmospheric circulation. *Meteorological Monographs*, 10, No. **32**, Americal Meteorological Society.

Klimowski, B.A., 1994: Initiation and development of rear inflow within the 28-29 June 1989 North Dakota mesoconvective system. *Mon. Wea. Rev.*, **122**, 765-779.

Knight, D.J., and P.V. Hobbs, 1988: The mesoscale and microscale structure and organization of clouds and precipitations in midlatitude cyclones. Part XV: A numerical modeling study of fontogenesis and cold-frontal rainbands. *J. Atmos. Sci.*, **45**, 915-930.

Koch, S., and R.E. Golus, 1988: A mesoscale gravity wave event observed during CCOPE. Part I: Multiscale statistical analysis of wave characteristics. *Mon. Wea. Rev.*, **116**, 2527-2544.

——, ——, and P.B. Dorian, 1988: A mesoscale gravity wave event observed during CCOPE. Part II: Interactions between mesoscale convective systems and the antecedent waves. *Mon. Wea. Rev.*, **116**, 2545-2569.

——, and P.B. Dorian, 1988: A mesoscale gravity wave event observed during CCOPE. Part III: Wave environment and probable source mechanisms. *Mon. Wea. Rev.*, **116**, 2570-2592.

Kreitzberg, C.W., and D.J. Perkey, 1976: Release of potential instability: Part I. A sequential plume model within a hydrostatic primitive equation model. *J. Atmos. Sci.*, **33**, 456-475.

Kuo, H.L., 1965: On formation and intensification of tropical cyclones through latent heat release by cumulus convection. *J. Atmos. Sci.*, **22**, 40-63.

——, 1974: Further studies of the parameterization of the influence of cumulus convection on large-scale flow. *J. Atmos. Sci.*, **31**, 1232-1240.

Lafore, J.-P., and M.W. Moncrieff, 1989: A numerical investigation of the organization and interaction of the convective and stratiform regions of tropical squall lines. *J. Atmos. Sci.*, **46**, 521-544.

Lalas, D.P., and F. Einaudi, 1976: On the characteristics of gravity waves generated by atmospheric shear layers. *J. Atmos. Sci.*, **33**, 1248-1259.

Leary, C.A., and E.N. Rappaport, 1987: The life cycle and internal structure of a mesoscale convective complex. *Mon. Wea. Rev.*, **115**, 1503-1527.

Lin, X., and R.H. Johnson, 1994: Heat and moisture budgets and circulation characteristics of a frontal squall line. *J. Atmos. Sci.*, **51**, 1661-1681.

Lin, Y.-L., and R.C. Goff, 1988: A study of a mesoscale solitary wave in the atmosphere originating near a region of deep convection. *J. Atmos. Sci.*, **45**, 194-205.

Lindzen, R.S., 1974: Wave-CISK in the tropics. *J. Atmos. Sci.*, **31**, 156-179.

——, and K.-K. Tung, 1976: Banded convective activity and ducted gravity waves. *Mon. Wea. Rev.*, **104**, 1602-1617.

Maddox, R.A., 1980a: Mesoscale convective complexes. *Bull. Amer. Meteor Soc.*, **61**, 1374-1387.

——, 1980b: An objective technique for separating macroscale and mesoscale features in meteorological data. *Mon. Wea. Rev.*, **108**, 1108-1121.

——, 1983: Large-scale meteorological conditions associated with midlatitude, mesoscale convective complexes. *Mon. Wea. Rev.*, **111**, 1475-1493.

——, D.J. Perkey and J.M. Fritsch, 1981: Evolution of upper tropospheric features during the development of a mesoscale convective complex. *J. Atmos. Sci.*, **38**, 1664-1674.

Mailhot, J., 1994: The regional finite-element (RFE) model scientific description - Part 2: Physics.

——, and R. Benoit, 1982: A finite-element model of the atmospheric boundary layer suitable for use with numerical weather prediction model. *J. Atmos. Sci.*, **39**, 2249-2266.

——, C. Chouinard, R. Benoit, M. Roch, G. Verner, J. Côté, and J. Pudykiewicz, 1989: Numerical forecasting of winter coastal storms during CASP: Evaluation of the regional finite-element model. *Atm. Ocean*, **27**, 24-58.

Manabe, S., J. Smagorinsky, and R.F. Strickler, 1965: Simulated climatology of a general circulation model with a hydrological cycle. *Mon. Wea. Rev.*, **93**, 769-798.

McAnelly, R.L., and W.R. Cotton, 1986: Meso-β-scale characteristics of an episode of meso-α-scale convective complexes. *Mon. Wea. Rev.*, **114**, 1740-1770.

——-, and W.R. Cotton, 1989: The precipitation life cycle of mesoscale convective complexes over the Central United States. *Mon. Wea. Rev.*, **117**, 784-808.

Menard, R.D., and J.M. Fritsch, 1989: A mesoscale convective complex-generated inertially stable warm core vortex. *Mon. Wea. Rev.*, **117**, 1237-1261.

Miller, F., and F. Sanders, 1980: Mesoscale conditions for the severe convection of 3 April 1974 in the east-central United States. *J. Atmos. Sci.*, **37**, 1041-1055.

Molinari, J., and M. Dudek, 1992: Parameterization of convective precipitation in mesoscale numerical models: A critical review. *Mon. Wea. Rev.*, **120**, 326-344.

Moncrieff, M.W., 1981: A theory of organized steady convection and its transport properties. *Quart. J. Roy. Meteor. Soc.*, **107**, 29-50.

Moore, J.T., and T.E. Lambert, 1993: The use of equivalent potential vorticity to diagnose regions of conditional symmetric instability. *Wea. Forecasting*, **8**, 301-308.

Nachamkin, J.E., R.L. McAnelly, and W.R. Cotton, 1994: An observational analysis of a developing mesoscale convective complex. *Mon. Wea. Rev.*, **122**, 1168-1188.

Newton, C.W., 1950: Structure and mechanisms of the prefrontal squall line. *J. Meteor.*, **7**, 210-222.

Ogura, Y., and M.-T. Liou, 1980: The structure of a midlatidude squall line: A case study. *J. Atmos. Sci.*, **37**, 553-567.

Parsons, D.B. and P.V. Hobbs, 1983: The mesoscale and microscale structure and organization of clouds and precipitation in midlatitude cyclones. IX: Some effects of orography on rainbands. *J. Atmos. Sci.*, **40**, 1930-1949.

Pecnick, M.J., and J.A. Young, 1984: Mechanics of a strong subsynoptic gravity wave deduced from satellite and surface observations. *J. Atmos. Sci.*, **41**, 1850-1862.

Powers, J.G., and R.J. Reed, 1993: Numerical simulation of the large-amplitude mesoscale gravity-wave event of 15 December 1987 in the central United States. *Mon. Wea. Rev.*, **121**, 2285-2308.

Pudykiewicz, J., R. Benoit, and J. Mailhot, 1992: Inclusion and verification of a predictive cloud water scheme in a regional numerical weather prediction model. *Mon. Wea. Rev.*, **120**, 612-626.

Ramage, C.S., 1982: Have precipitation forecasts improved ? *Bull. Amer. Meteor. Soc.*, **63**, 739-742.

Ramamurthy, M.K., R.M. Rauber, B.P. Collins, and N.K. Malhotra, 1993: A comparative study of large-amplitude gravity-wave events. *Mon. Wea. Rev.*, **121**, 2951-2974.

Rasmussen, E.N. and S.A. Rutledge, 1993: Evolution of quasi-two-dimensional squall lines. Part I: Kinematic and reflectivity structure. *J. Atmos. Sci.*, **50**, 2584-2606.

Raymond, D.J., 1975: A model for predicting the movement of continuously propagating convective storms. *J. Atmos. Sci.*, **32**, 1308-1317.

——, 1976: Wave-CISK and convective mesosystems. *J. Atmos. Sci.*, **33**, 2392-2398.

——, 1984: A wave-CISK model of squall lines. *J. Atmos. Sci.*, **41**, 1946-1958.

——, 1987: A forced gravity wave model of self-organizing convection. *J. Atmos. Sci.*, **44**, 3523-3543.

Reuter, G.W., and M.K. Yau, 1990: Observations of slantwise convective instability in winter cyclones. *Mon. Wea. Rev.*, **118**, 447-458.

Robert, A., J. Henderson, and C. Turnbull, 1972: An implicit time integration scheme for baroclinic models of the atmosphere. *Mon. Wea. Rev.*, **100**, 329-335.

Rotunno, R., J.B. Klemp, and M.L. Weisman, 1988: A theory for strong, long-lived squall lines. *J. Atmos. Sci.*, **45**, 463-485.

Rutledge, S.A., R.A. Houze, Jr., M.I. Biggerstaff, and T. Matejka, 1988: The Oklahoma-Kansas mesoscale convective system of 10-11 June 1985: Precipitation structure and single-Doppler radar analysis. *Mon. Wea. Rev.*, **116**, 1409-1430.

Sanders, F., 1979: Trends in skill of daily forecasts of temperature and precipitation, 1966-78. *Bull. Amer. Meteor. Soc.*, **60**, 763-769.

——, and L.F. Bosart, 1985: Mesoscale structure in the megalopolitan snowstorm of 11-12 February 1983. Part I: Frontogenetical forcing and symmetric instability. *J. Atmos. Sci.*, **42**, 1050-1061.

Sasamori, T, 1972: A linear harmonic analysis of atmospheric motion with radiative dissipation. *J. Meteor. Soc. Japan*, **50**, 505-518.

Schmidt, J.M., and W.R. Cotton, 1990: Interactions between upper and lower tropospheric gravity waves on squall line structure and maintenance. *J. Atmos. Sci.*, **47**, 1205-1222.

Skamarock, W.C., M.L. Weisman, and J.B. Klemp, 1994: Three-dimensional evolution of simulated long-lived squall lines. *J. Atmos. Sci.*, **51**, 2563-2584.

Smull, B.F., and R.A. Houze, Jr., 1985: A midlatitude squall line with a trailing region of stratiform rain: Radar and satellite observations. *Mon. Wea. Rev.*, **113**, 117-133.

——, and ——, 1987: Rear inflow in squall lines with trailing stratiform precipitation. *Mon. Wea. Rev.*, **115**, 2869-2889.

Snook, J.S., 1992: Current technique for real-time evaluation of conditional symmetric instability. *Wea. Forecasting*, **7**, 430-439.

Srivastava, R.C., T.J. Matejka and T.J. Lorello, 1986: Doppler radar study of the trailing anvil region associated with a squall line. *J. Atmos. Sci.*, **43**, 356-377.

Staniforth, A., 1987: Review - Formulating efficient finite-element codes for flows in regular domains. *Int. J. Numer. Meth. Fluids*, **7**, 1-16.

——, and H.L. Mitchell, 1978: A variable-resolution finite-element technique for regional forecasting with the primitive equations. *Mon. Wea. Rev.*, **106**, 439-447.

——, and R.W. Daley, 1979: A baroclinic finite-element model for regional weather forecasting with the primitive equations. *Mon. Wea. Rev.*, **107**, 107-121.

——, and C. Temperton, 1986: Semi-implicit semi-Lagrangian integration schemes for a barotropic finite-element regional model. *Mon. Wea. Rev.*, **114**, 2078-2090.

——, and J. Côté, 1991: Semi-Lagrangian integration schemes for atmospheric models - A review. *Mon. Wea. Rev.*, **119**, 2206-2223.

Stensrud, D.J., R.A. Maddox, and C.L. Ziegler, 1991: A sublimation-initiated mesoscale downdraft and its relation to the wind field below a precipitation anvil cloud. *Mon. Wea. Rev.*, **119**, 2124-2139.

——, and J.M. Fritsch, 1993: Mesoscale convective systems in weakly forced large-scale environments. Part I: Observations. *Mon. Wea. Rev.*, **121**, 3326-3344.

——, and ——, 1994a: Mesoscale convective systems in weakly forced large-scale environments. Part II: Generation of a mesoscale initial condition. *Mon. Wea. Rev.*, **122**, 2068-2083.

——, and ——, 1994b: Mesoscale convective systems in weakly forced large-scale environments. Part III: Numerical simulations and implications for operational forecasting. *Mon. Wea. Rev.*, **122**, 2084-2104.

Stirling, J. and R.M. Wakimoto, 1989: Mesoscale vortices in the stratiform region of a decaying midlatitude squall line. *Mon. Wea. Rev.*, **117**, 452-458.

Stobie, J.G., F. Einaudi, and L.W. Uccellini, 1983: A case study of gravity waves-convective storms interaction: 9 May 1979. *J. Atmos. Sci.*, **40**, 2804-2830.

Strang, G., and G. Fix, 1973: *An analysis of the finite-element method.* Prentice Hall, 306 pp.

Stumpf, G.J., R.H. Johnson, and B.F. Smull, 1991: The wake low in a midlatitude mesoscale convective system having complex convective organization. *Mon. Wea. Rev.*, **119**, 134-158.

Sun, W.-Y., 1984: Rainbands and symmetric instability. *J. Atmos. Sci.*, **41**, 3112-3426.

Sundqvist, H., E. Berge, and J.E. Kristjansson, 1989: Condensation and cloud parameterization studies with a mesoscale numerical weather prediction model. *Mon. Wea. Rev.*, **117**, 1641-1657.

Tanguay, M., A. Simard, and A. Staniforth, 1989: A three-dimensional semi-Lagrangian scheme for the Canadian regional finite-element forecast model. *Mon. Wea. Rev.*, **117**, 1861-1871.

Temperton, C., and M. Roch, 1991: Implicit normal mode initialization for an operational regional model. *Mon. Wea. Rev.*, **119**, 667-677.

Thorpe, A.J., M.J. Miller, and M.W. Moncrieff., 1982: Two-dimensional convection in non-constant shear: A model of mid-latitude squall lines. *Quart. J. Roy. Meteor. Soc.*, **108**, 739-762.

——, and K.A. Emanuel, 1985: Frontogenesis in the presence of small stability to slantwise convection. *J. Atmos. Sci.*, **42**, 1809-1824.

——, and R. Rotunno, 1989: Nonlinear aspects of symmetric instability. *J. Atmos. Sci.*, **46**, 1285-1299.

Tremblay, A., 1994: Simulations of the 14 July 1987 squall line using a fully compressible model. *Atmos.-Ocean*, **22**, 567-603.

Trier, S.B., D.B. Parsons, and J.E.H. Clark, 1991: Environment and evolution of a cold-frontal mesoscale convective system. *Mon. Wea. Rev.*, **119**, 2429-2455.

——, and D.B. Parsons, 1993: Evolution of environmental conditions preceding the development of a nocturnal mesoscale convective complex. *Mon. Wea. Rev.*, **121**, 1078-1098.

Uccellini, L.W., 1975: A case study of apparent gravity wave initiation of severe convective storms. *Mon. Wea. Rev.*, **103**, 497-513.

——, and D.R. Johnson, 1979: The coupling of upper and lower tropospheric jet streaks and implications for the development of severe convective storms. *Mon. Wea. Rev.*, **107**, 682-703.

——, and S.E. Koch, 1987: The synoptic setting and possible energy sources for mesoscale wave disturbances. *Mon. Wea. Rev.*, **115**, 721-729.

Van Tuyl, A.H., and J.A. Young, 1982: Numerical simulation of nonlinear jet streak adjustment. *Mon. Wea. Rev.*, **110**, 2038-2054.

Wagner, A.J., 1962: Gravity wave over New England, April 12, 1961. *Mon. Wea. Rev.*, **90**, 431-436.

Weisman, M.L., 1992: The role of convectively generated rear-inflow jets in the evolution of long-lived mesoconvective systems. *J. Atmos. Sci.*, **49**, 1826-1847.

——, 1993: The genesis of severe, long-lived bow echoes. *J. Atmos. Sci.*, **50**, 645-670.

——, and J.B. Klemp, 1982: The dependence of numerically simulated convective storms on vertical wind shear and buoyancy. *Mon. Wea. Rev.*, **110**, 504-520.

Xu, Q., 1986: Conditional symmetric instability and mesoscale rainbands. *Quart. J. Roy. Meteor. Soc.*, **112**, 315-334.

——, and J.H.E. Clark, 1984: Wave CISK and mesoscale convective systems. *J. Atmos. Sci.*, **41**, 2089-2107.

Zhang, D.-L., 1989: The effect of parameterized ice microphysics on the simulation of vortex circulation with a mesoscale hydrostatic model. *Tellus*, **41A**, 132-147.

——, 1992: The formation of a cooling-induced mesovortex in the trailing stratiform region of a midlatitude squall line. *Mon. Wea. Rev.*, **120**, 2763-2785.

——, and J.M. Fritsch, 1986: Numerical simulation of the meso-β scale structure and evolution of the 1977 Johnstown flood. Part I: Model description and verification. *J. Atmos. Sci.*, **43**, 1913-1943.

——, and ——, 1987: Numerical simulation of the meso-β scale structure and evolution of the 1977 Johnstown flood. Part II: Inertially stable warm-core vortex and the mesoscale convective complex. *J. Atmos. Sci.*, **44**, 2593-2612.

——, and ——, 1988a: Numerical simulation of the meso-β scale structure and evolution of the 1977 Johnstown flood. Part III: Internal gravity waves and the squall line. *J. Atmos. Sci.*, **45**, 1252-1268.

——, and ——, 1988b: A numerical investigation of a convectively generated, inertially stable, extratropical warm-core mesovortex over land. Part I: Structure and evolution. *Mon. Wea. Rev.*, **116**, 2660-2687.

——, and ——, 1988c: Numerical sensitivity experiments of varying model physics on the structure, evolution and dynamics of two mesoscale convective systems. *J. Atmos. Sci.*, **45**, 261-293.

——, E.-Y. Hsie, and M.W. Moncrieff, 1988: A comparison of explicit and implicit predictions of convective and stratiform precipitating weather systems with a meso-β -scale numerical model. *Quart. J. Roy. Meteor. Soc.*, **114**, 31-60.

——, K. Gao, and D.B. Parsons, 1989: Numerical simulation of an intense squall line during 10-11 June 1985 PRE-STORM. Part I: Model verification. *Mon. Wea. Rev.*, **117**, 960-994.

——, and ——, 1989: Numerical simulation of an intense squall line during 10-11 June 1985 PRE-STORM. Part II: Rear inflow, surface pressure perturbations and stratiform precipitation. *Mon. Wea. Rev.*, **117**, 2067-2094.

——, and H.-R. Cho, 1992: The development of negative moist potential vorticity in the stratiform region of simulated squall line. *Mon. Wea. Rev.*, **120**, 1322-1341.

——, and ——, 1995: Three-dimensional simulation of frontal rainbands and conditional symmetric instability in the Eady-wave model. *Tellus*, **47A**, in press.

——, J.S. Kain, J.M. Fritsch, and K. Gao, 1994: Comments on "Parameterization of convective precipitation in mesoscale numerical models: A critical review". *Mon. Wea. Rev.*, **122**, 2222-2231.

Zheng, Y., Q. Xu, and D.J. Stensrud, 1994: A numerical study of the 7 May 1985 mesoscale convective system: Initial condition sensitivities. *Mon. Wea. Rev.*, submitted.

Zipser, E.J., 1969: The role of organized unsaturated convective downdrafts in the structure and rapid decay of an equatorial disturbance. *J. Appl. Meteor.*, **8**, 799-814.

——, 1977: Mesoscale and convective-scale downdrafts as distinct components of squall-line structure. *Mon. Wea. Rev.*, **105**, 1568-1589.

——, R.J. Meitin, and M.A. Lemone, 1982: Mesoscale motion fields associated with a slowly moving GATE convective band. *J. Atmos. Sci.*, **38**, 1725-1750.